OBSERVATIONAL STUDIES OF SOIL MOISTURE, VALLEY FOG AND TEMPERATURE VARIANCE IN THE ATMOSPHERIC BOUNDARY LAYER OVER DIVERSE TERRAIN

by

Chaoxun Hang

A dissertation submitted to the faculty of
The University of Utah
in partial fulfillment of the requirements for the degree of

Doctor of Philosophy

Department of Mechanical Engineering

The University of Utah

December 2017

The University of Utah Graduate School

STATEMENT OF DISSERTATION APPROVAL

The dissertation of **Chaoxun Hang**
has been approved by the following supervisory committee members:

Eric R. Pardyjak ,	Chair(s)	**19 Jun 2017** Date Approved
Daniel F. Nadeau ,	Chair(s)	**07 Jul 2017** Date Approved
James R. Stoll II ,	Member	**05 Jul 2017** Date Approved
Marc Calaf ,	Member	**29 Jun 2017** Date Approved
Sebastian Wilhelm Hoch ,	Member	**05 Jul 2017** Date Approved

by **Timothy A. Ameel** , Chair/Dean of
the Department/College/School of **Mechanical Engineering**
and by **David B. Kieda** , Dean of The Graduate School.

ABSTRACT

The atmospheric boundary layer (ABL) has been widely investigated due to the complexity of its physical processes and its impact on human life. One of the most challenging yet critical topics in this layer is scalar transport. Many efforts have been dedicated to investigating heat and moisture transport in the ABL using experimental and numerical approaches over the last several decades. However, there are still many knowledge gaps that limit the performance of numerical weather prediction models, in particular over complex terrain. For example, insufficient understanding of near-surface processes has resulted difficulties in parameterizing meteorological variables in numerical models. Hence, the main objective of this work is to gain a better fundamental understanding of flow processes and scalar transport in the surface boundary layer over different types of terrain with the ultimate goal of improving numerical weather forecasting models by developing more accurate surface parameterizations. Three different topics are discussed in this dissertation.

The first topic is a study of land-atmosphere interactions over a desert playa to better understand the impacts of spatial and temporal heterogeneity in water availability as part of the short-term hydrologic cycle. High evaporation rates and the exponential decay of these rates are observed following occasional rainfall events. Three main factors explained the fast evaporation observed following rainfall. The first factor is the existence of a powerful positive feedback mechanisms initialized by rainfall events that leads to increasing volumetric water content, decreasing surface albedo and Bowen ratio, followed by increases in net radiation, and eventually the enhancement of evaporation rates. The second factor is the clay soil texture, which has low permeability and high capacity. The soil property makes more water available near the surface for evaporation. The third factor is the non-negligible nocturnal evaporation rates that are correlated with increasing soil moisture content. Moreover, a higher spatial variability of surface soil moisture and evaporation is observed when the surface is dry.

The second topic is articulated around a case study of the mechanisms that modulates the evolution of valley fog. A typical shallow, early-morning, short-lived valley fog is observed in a sheltered alpine valley. This work shows that mountain circulations play a critical role in the formation and development of shallow valley fog by modulating temperature and moisture fields through katabatic flow interactions and gravity waves. In particular, internal gravity waves are shown to modulate fog processes by varying the near-surface temperature within a time period of ≈ 20 min.

The purpose of the last topic is to better understand the potential temperature variance budget over three different surfaces, a desert playa (dry lakebed), characterized by a flat surface devoid of vegetation; a vegetated site, characterized by a flat valley floor covered with greasewood vegetation, and a mountain terrain site with a slope angle of 2 -4° and covered by high-elevation vegetation. The analysis reveals the presence of a 5-m layer where the production and dissipation terms of potential temperature variance ($\overline{\theta^2}$) drop rapidly below this level. Within the 5-m layer, turbulent transport of $\overline{\theta^2}$ acts as a sink term at all sites of interest. The ratio of turbulent transport to production of $\overline{\theta^2}$ remains constant as stability decreases. The imbalance ratio between production and dissipation shows no correlation with the stability conditions.

For my parents and Yao.

CONTENTS

CHAPTERS

ACKNOWLEDGEMENTS

I would like to express my greatest gratitude to my graduate advisor, Eric Pardyjak, for his continuous support and guidance in my graduate life and for being such a great academic example who promotes me to think, to explore, and to learn independently. I would also like to thank my co-advisor, Daniel Nadeau, for his endless patience with my writing, for continuous inspiration and cheering, and for the numerous academic ideas that help me to finish my graduate studies. I would also like to thank my committee members, Rob Stoll, Sebastian Hoch and Marc Calaf for their career advice and valuable help throughout these years.

I want to thank Derek Jensen for his numerous suggestions on instrument deployment, data analysis, and playing ping pong with me. I thank Nipun Gunawardena for his help in many of my field trips. He made the tough work enjoyable. I also thank Alexei Perelet for being a great field partner who fights cows with me in Heber Valley. I am grateful for Daniel Alexander for being my escort in United States Army Dugway Proving Ground when the air temperature was above 115 °F. I would also thank all my friends in the Environmental Fluid Dynamics Lab, who made my graduate life so enjoyable and full of excitement.

I would like to give thanks to my parents for their support and encouragement when I am in the United States. I am grateful to Yao Yao, for giving me the opportunity to transfer to Utah and for her countless efforts to make my life so joyful.

Finally, I want to thank the Mountain Terrain Atmospheric Modeling and Observations (MATERHORN) team that makes the program possible and the Office of Naval Research for its generous support.

CHAPTER 1

INTRODUCTION

Flow motion in the atmospheric boundary layer can be extremely difficult to study over typical complex terrain, which can be broadly defined as regions with irregular topography (Rotach et al., 2008) and/or regions that generally have strong spatial heterogeneities. It can influence a wide range of scales from small turbulent eddies to synoptic-scale processes (Arya, 2001). The atmosphere over complex terrain experiences terrain-induced circulations, such as katabatic and anabatic flows, sea breezes etc., which altogether define the local meteorological conditions near the surface. On the other hand, flow over flat terrain with complexities induced by surface heterogeneity of temperature or moisture encounters strong surface temperature variations, along with uneven evaporation rates, surface properties variability (e.g., albedo and soil properties)(Hang et al., 2015). In order to narrow the knowledge gap, the strategy of this dissertation is to use observational data to examine the flow processes over complex terrain that have not been well–studied to better understand scalar transport. The main objective is to better understand the flow dynamics and improve numerical weather prediction over diverse types of terrain.

1.1 Atmospheric Boundary Layer

The atmospheric boundary layer (ABL) is formed by the interaction between the atmosphere and the land or water surface. The ABL has been widely investigated due to not only the complexity of physical processes, but also to its impact on human life. It plays an extremely important role in many fields, such as air quality, agriculture, weather forecasting, prediction of natural hazards, etc. Hence, in order to improve the understanding of the atmospheric processes across various temporal (from seconds to days) and spatial (from millimeters to kilometers) scales, numerous studies have been conducted regarding to momentum and scalar transport over land and water surfaces (Garratt, 1994), idealized and complex terrain (Kaimal & Finnigan, 1994), unstable (Mason, 1989), stable (Mahrt, 1999) and transitional (Garratt, 1990; Wyngaard, 2010) atmospheric conditions. Within the ABL, the lowest one-tenth is usually refereed as the surface layer, where the turbulent flux and stress are assumed to be changed less than 10% of their magnitude (Stull, 1988) and the most significant exchanges of meteorological variables occur (Arya, 2001). The physical processes in the surface layer have a general meteorological significance due to the fact that the dynamic interaction in the surface layer is actually the main source of atmospheric moisture and heat (Monin & Obukhov, 1954).

1.2 Scalar Transport in the Atmospheric Boundary Layer

Within the atmospheric boundary layer, the exchanges of heat and moisture are caused by both turbulent and nonturbulent motion in the air. In particular, the turbulence in the surface layer is responsible for the scalar transport between the atmosphere and the ground surface. Of particular interest in this dissertation is evaporation from land and water surfaces, which provides nearly all of the atmospheric moisture. Evaporation is not only a crucial part of the water cycle, but also of the surface energy budget. In addition, the moisture leads to the formation of clouds and ground fog by interacting with particles and aerosols (Arya, 2001).

1.3 Flow Over Complex Terrain

The majority of complex terrain in the world is contained in mountainous regions, which covers about 70% of land surfaces on the earth including hills, slopes, valleys, gullies, etc. (Strobach, 1991). There are a large number of flow processes exclusive to complex terrain (Figure 1 from Fernando et al., 2015), such as mountain circulations at the slope and valley scales (Fernando, 2010; Whiteman, 2000), internal gravity waves (Nappo, 2002), cold-air pools (Clements et al., 2003), smaller topographic features (Baines, 1995) etc. In order to fill the knowledge gaps, such as the prediction of near-surface temperature and moisture transport, the parameteraizations of turbulence closure models, the role of soil moisture and soil properties in mountainous terrain, etc., a better understanding of flow physics leaves much to be desired.

1.4 Flow Over Heterogeneous Terrain

In this dissertation, a heterogeneous terrain is specifically defined as terrain which has a flat surface with small surface roughness and strong thermal or moisture heterogeneities. Figure 1.1 shows a field site called desert playa where can be characterized by negligible surface roughness and high variation of surface temperature at different scales (Figure 1.1a, 1.1b). A desert playa is a remnant of an endorheic lake or an ephemeral lakebed, which are found in semi-arid/ arid regions across different continents, such as the Great Basin in United States (Hang et al., 2015; Malek, 2003); the Lake George and Lake Eyre in Australia (Torgersen, 1984); the Qaidam basin in China (Kezao & Bowler, 1986). However, there are few studies have been attempted to study the scalar transport over playa in the ABL (Torgersen, 1984; Tyler et al., 2006).

1.5 The MATERHORN Program

The Mountain Terrain Atmospheric Modeling and Observations (MATERHORN) Program was designed to better understand atmospheric flow dynamics across a wide range of scales over realistic mountainous terrain. This five-year long project funded by the Office of Naval Research Award involved 11 principal investigators from five academic institutions. The MATERHORN program consisted of four components including field experiments, parameterization development, modeling, and technology development. More details can be found in Fernando et al., (2015). In this dissertation, we analyze data from the experimental component, which consisted of three extensive field campaigns: Fall 2012, Spring 2013, and Fog-X 2015. They are inspired and guided by many recent extensive field campagin over complex terrains, such as the Vertical Transport and Mixing Experiment (VTMX; Doran et al., 2002), the Mesoscale Alpine Programme (MAP; Rotach & Zardi, 2007), the Meteor Crater Experiment (METCRAX; Whiteman et al., 2008),

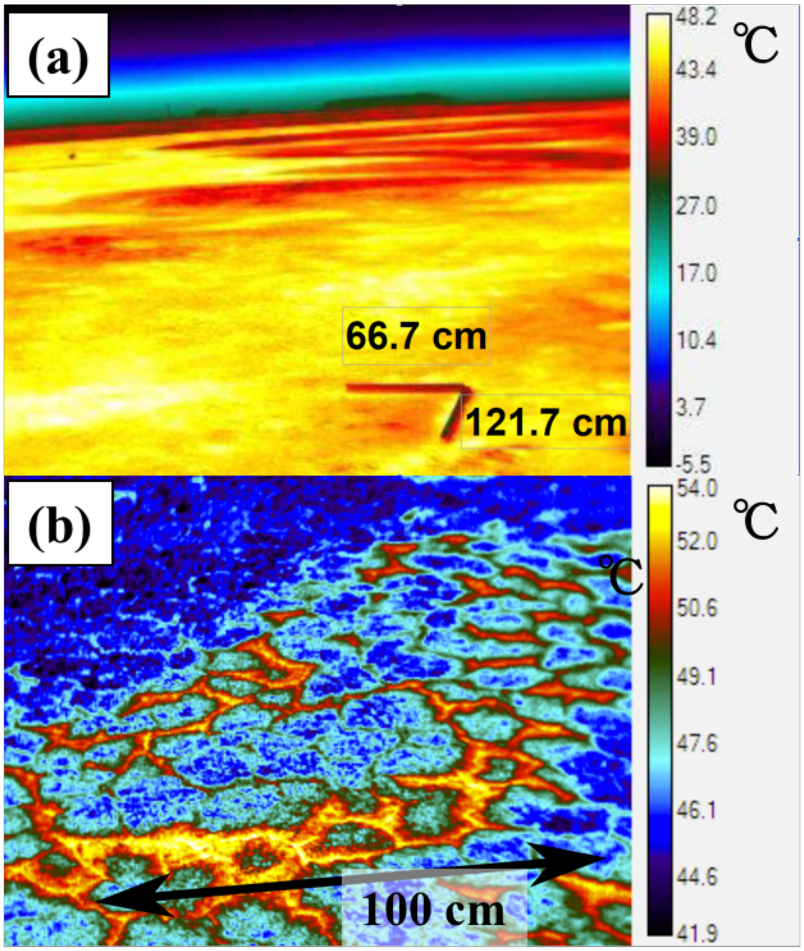

Figure 1.1: (a) Large–scale infrared picture (19 June 2014 1530 MST); (b) Small–scale infrared picture (23 July 2014 1420 MST).

the Phoenix Air Flow Experiment (PAFEX; Pardyjak et al., 2009), the Boundary-Layer Late Afternoon and Sunset Turbulence (BLLAST; Lothon et al., 2014). The former two were conducted at the United States Army's Dugway Proving Ground (DPG), located about 137 km southwest of Salt Lake City, Utah. The DPG site is characterized by an arid environment consisting of salt flats and isolated hills surrounded by interconnected mountains. The Fall 2012 campaign ran from 26 September – 7 Novermber 2012, and the Spring 2013 campaign ran from 1 May – 6 June 2013. The last campaign was conducted on a dairy farm in Heber Valley, Utah, which is a sheltered alpine valley with mixed agricultural and urban land cover. The field campaign ran from 7 January – 1 February 2015.

1.6 Dissertation Organization and Scientific Questions

The overarching goal of this dissertation is to better understand the flow dynamics corresponding to the scalar transport so that numerical weather prediction over complex and heterogeneous terrain can be improved. Chapters 2–4 study different areas of application of meteorology and some fundamental atmospheric fluid dynamics with respect to the exchanges of heat and moisture in the ABL. Chapter 2 presents the soil moisture and evaporation dynamics over a thermally heterogeneous terrain and investigates the heterogeneity of energy balance and land-atmosphere interaction over a desert playa. The study has been published in *Boundary-Layer Meteorology* with the citation: Hang, C., Nadeau, D. F., Jensen, D. D., Hoch, S. W., and Pardyjak, E. R., 2016: Playa Soil Moisture and Evaporation Dynamics During the MATERHORN Field Program. *Boundary-Layer Meteorol.*, **159(3)**, 521–538. Chapter 3 focuses on the effects of flow processes over mountainous terrain on fog evolution. The study has been published in *Pure and Applied Geophysics* with the citation: Hang, C., Nadeau, D.F., Gultepe, I., Hoch, S.W., Romn-Cascn, C., Pryor, K., Fernando, H.J.S., Creegan, E.D., Leo, L.S., Silver, Z. and Pardyjak, E.R., 2016. A case study of the mechanisms modulating the evolution of valley fog. *Pure and Applied Geophysics.*, *173(9)*, 3011–3030. Chapter 4 examines the temporal and spatial variations of near-surface temperature variance over three different surfaces. The study will be submitted to *Environmental Fluid Mechanics*. Finally, Chapter 5 shows the general conclusion and future works.

1.7 References

Arya, P. S. (2001), *Introduction to micrometeorology*, San Diego, CA: Academic doi: https://doi.org/10.1016/s0074-6142(01)x8014-5

Baines, P. G. (1995), *Topographic effects in stratified flows*, Cambridge monographs on mechanics, Cambridge, UK: Cambridge University. .

Clements, C. B., C. D. Whiteman, & J. D. Horel (2003), Cold-air-pool structure and evolution in a mountain basin: Peter sinks, Utah, *Journal of Applied Meteorology*, *42*(6), 752–768, doi:http://doi.org/cd3z3x

Doran, J. C., J. D. Fast, & J. Horel (2002), The VTMX 2000 campaign, *Bulletin of the American Meteorological Society*, *83*(4), 537–551, doi:https://doi.org/10.1175/1520-0477(2002)0832.3.co

Fernando, H. J. S. (2010), Fluid dynamics of urban atmospheres in complex terrain, *Annual Review of Fluid Mechanics*, *42*(1), 365–389, doi: https://doi.org/10.1146/annurev-fluid-121108-145459

Fernando, H. J. S., et al. (2015), The MATERHORN: Unraveling the intricacies of mountain weather, *Bulletin of the American Meteorological Society*, *96*(11), 1945–1967, doi:https://doi.org/10.1175/bams-d-13-00131.1

Garratt, J. R. (1990), The internal boundary layer — a review, *Boundary-Layer Meteorology*, *50*(1-4), 171–203, doi:https://doi.org/10.1007/bf00120524

Garratt, J. R. (1994), Review: The atmospheric boundary layer, *Earth-Science Reviews*, *37*(1-2), 89–134, doi:https://doi.org/10.1016/0012-8252(94)90026-4

Hang, C., D. F. Nadeau, D. D. Jensen, S. W. Hoch, & E. R. Pardyjak (2015), Playa soil moisture and evaporation dynamics during the MATERHORN field program, *Boundary-Layer Meteorology*, *159*(3), 521–538, doi: https://doi.org/10.1007/s10546-015-0058-0

Kaimal, J. C., & J. J. Finnigan (1994), *Atmospheric boundary layer flows: their structure and measurement*, Oxford, UK: Oxford University.

Kezao, C., & J. M. Bowler (1986), Late pleistocene evolution of salt lakes in the Qaidam basin, Qinghai Province, China, *Palaeogeography, Palaeoclimatology, Palaeoecology*, *54*(1-4), 87–104, doi:https://doi.org/10.1016/0031-0182(86)90119-7

Lothon, M., et al. (2014), The BLLAST field experiment: Boundary-Layer Late Afternoon and Sunset Turbulence, *Atmospheric Chemistry and Physics*, *14*(20), 10,931–10,960.

Mahrt, L. (1999), Stratified atmospheric boundary layers, *Boundary-Layer Meteorology*, *90*(3), 375–396 .

Malek, E. (2003), Microclimate of a desert playa: evaluation of annual radiation, energy, and water budgets components, *International Journal of Climatology*, *23*(3), 333–345.

Mason, P. J. (1989), Large-eddy simulation of the convective atmospheric boundary layer, *Journal of the Atmospheric Sciences*, *46*(11), 1492–1516.

Monin, A. S., & A. M. Obukhov (1954), Basic laws of turbulent mixing in the surface layer of the atmosphere, *Contributions of the Geophysical Institute of the Academy of Sciences*, *24*(151), 163–187.

Nappo, C. J. (2002), *An introduction to atmospheric gravity waves*, Cambridge, MA: Academic.

Pardyjak, E. R., H. J. S. Fernando, J. C. R. Hunt, A. A. Grachev, & J. Anderson (2009), A case study of the development of nocturnal slope flows in a wide open valley and associated air quality implications, *Meteorologische Zeitschrift*, *18*(1), 85–100.

Rotach, M. W., & D. Zardi (2007), On the boundary-layer structure over highly complex terrain: Key findings from map, *Quarterly Journal of the Royal Meteorological Society*, *133*(625), 937–948.

Rotach, M. W., M. Andretta, P. Calanca, A. P. Weigel, & A. Weiss (2008), Boundary layer characteristics and turbulent exchange mechanisms in highly complex terrain, *Acta Geophysica*, *56*(1), 194–219.

Strobach, K. (1991), *Unser planet erde: ursprung und dynamik. (German) [Our Planet Earth: Origin and Dynamics]*, Berlin, Germany: Gebrüder Bornträger.

Stull, R. B. (1988), *An introduction to boundary layer meteorology*, 670 pp., Berlin, Germany: Springer Science & Business Media.

Torgersen, T. (1984), Wind effects on water and salt loss in playa lakes, *Journal of Hydrology*, *74*(1-2), 137–149.

Tyler, S. W., J. F. Muñoz, & W. W. Wood (2006), The response of playa and sabkha hydraulics and mineralogy to climate forcing., *Ground Water*, *44*(3), 329–38.

Whiteman, C. D. (2000), *Mountain meteorology: fundamentals and applications*, Oxford, UK: Oxford University.

Whiteman, C. D., et al. (2008), METCRAX 2006: Meteorological experiments in Arizona's meteor crater, *Bulletin of the American Meteorological Society*, *89*(11), 1665–1680.

Wyngaard, J. C. (2010), *Turbulence in the atmosphere*, Cambridge, UK: Cambridge University.

CHAPTER 2

SOIL MOISTURE AND EVAPORATION DYNAMICS IN A SEMI-ARID AREA

The article in this chapter was originally published in *Boundary-Layer Meteorology* (2016) **159**, 521–538. Reprinted with the kind permission of Springer International Publishing.

Boundary-Layer Meteorol (2016) 159:521–538
DOI 10.1007/s10546-015-0058-0

ARTICLE

Playa Soil Moisture and Evaporation Dynamics During the MATERHORN Field Program

Chaoxun Hang[1] · **Daniel F. Nadeau**[2] ·
Derek D. Jensen[1] · **Sebastian W. Hoch**[3] · **Eric R. Pardyjak**[1]

Received: 16 October 2014 / Accepted: 23 June 2015 / Published online: 15 July 2015

Abstract We present an analysis of field data collected over a desert playa in western Utah, USA in May 2013, the most synoptically active month of the year, as part of the Mountain Terrain Atmospheric Modeling and Observations (MATERHORN) program. The results show that decreasing surface albedo, decreasing Bowen ratio and increasing net radiation with increasing soil moisture sustained a powerful positive feedback mechanism promoting large evaporation rates immediately following rain events. Additionally, it was found that, while nocturnal evaporation was negligible during dry periods, it was quite significant (up to 30 % of the daily cumulative flux) during nights following rain events. Our results further show that the highest spatial variability in surface soil moisture is found under dry conditions. Finally, we report strong spatial heterogeneities in evaporation rates following a rain event. The cumulative evaporation for the different sampling sites over a five-day period varied from $\approx$0.1 to $\approx$6.6 mm. Overall, this study allows us to better understand the mechanisms underlying soil moisture dynamics of desert playas as well as evaporation following occasional rain events.

Keywords Bare soil evaporation · Dry lake · Gravimetric method · Nocturnal evaporation · Spatial heterogeneity · Surface energy balance

1 Introduction

Drylands, defined as regions in which potential evapotranspiration exceeds annual precipitation, cover more than 40 % of the exposed earth surface (D'Odorico and Porporato 2006). Particularly in arid areas, where the average annual precipitation is less than 250 mm, soil

---

✉ Eric R. Pardyjak
pardyjak@eng.utah.edu

[1] Department of Mechanical Engineering, University of Utah, Salt Lake City, UT 84112, USA

[2] Department of Civil and Water Engineering, Université Laval, Quebec City, Canada

[3] Department of Atmospheric Sciences, University of Utah, Salt Lake City, UT 84112, USA

moisture is known to be a key driver of eco-hydrological (D'Odorico and Porporato 2006) and meteorological (Seneviratne et al. 2010; Zhou and Geerts 2013; Massey et al. 2014) processes. Soil water content controls the partitioning of incoming energy at the surface into latent and sensible heat fluxes. Despite considerable efforts (Famiglietti et al. 1998, 2008; Teuling 2005; Tyler et al. 2006; Teuling et al. 2007; Vivoni et al. 2010; Ivanov et al. 2010; Mittelbach and Seneviratne 2012), because of the wide range of scales and processes involved, there are still knowledge gaps regarding spatial and temporal soil moisture dynamics in arid areas. A better understanding and parametrization of soil moisture content is necessary for predicting surface and boundary-layer variables, cloud formation, and atmospheric boundary-layer structure (Ookouchi et al. 1984; Avissar and Pielke 1989; Segal et al. 1989; Ek and Holtslag 2004; Zhou and Geerts 2013; Massey et al. 2014).

Temporal variations of soil moisture are controlled by a series of interactions at the land-atmosphere interface, such as precipitation and evapotranspiration, but also by water transport in the soil layer itself. Feedback mechanics involving soil moisture exist and can act to accelerate or decelerate water transport in the soil-vegetation-atmosphere continuum (Menenti 1984; Allison and Barnes 1985; Yechieli and Wood 2002; Warner 2004; Gowing et al. 2006; Tyler et al. 2006). For instance, when soil water content increases after a rainfall event, evaporation rates are enhanced and thus promote additional precipitation events (Koster and Suarez 2003). Even a small amount of rain can radically change the energy balance (Malek et al. 1990). In addition to increased water availability, wetter soils have a lower surface albedo, and thus more energy is available for evapotranspiration (Idso and Jackson 1975; Eltahir 1998; Zheng and Eltahir 1998; Schär et al. 1999). However, moist high salinity soils act to reduce evaporation by lowering the saturation vapour pressure (Warner 2004). These feedback mechanics are critical because they not only affect precipitation, but they also clearly affect the atmospheric boundary-layer structure (Rife et al. 2002; Zhou and Geerts 2013).

Soil water fluctuations are driven to a large extent by evapotranspiration at the land surface. In arid areas with very limited vegetation cover (such as desert playas—a remnant of an endorheic lake or an ephemeral lakebed), transpiration can be ignored and bare soil evaporation prevails. Following a rain event, bare soil evaporation has been shown to display two main stages based on theoretical studies (Philip 1957) and field experiments (Black et al. 1969; Parlange et al. 1992; Brutsaert and Chen 1995). In the first stage, when the soil is saturated, the evaporation rate is mostly controlled by the available energy and atmospheric drying power (i.e. wind speed, vapour pressure deficit, etc.) (Katul and Parlange 1992). In the second stage, the rate of evaporation is primarily limited by the soil moisture content and soil properties. Little is known about what controls the duration of each stage in the arid environment. In addition, recent studies have found that nocturnal evaporation could account for more than 10 % of the total daily evaporation (Burgess et al. 1998; Fisher and Baldocchi 2007; Dawson et al. 2007; Oishi et al. 2008). To the best of our knowledge, no previous studies have quantified the significance of nocturnal evaporation in arid areas. Given the large water vapour pressure deficits typically found at night (Novick et al. 2009), we hypothesize that nocturnal evaporation is significant over arid playas and should be quantified.

Studies on spatial patterns of soil moisture have proliferated in recent years originating from both meteorological and hydrological communities (Whitaker 1993; Scanlon and Goldsmith 1997; Lawrence and Hornberger 2007; Vivoni et al. 2008). As a result, several controlling factors of soil moisture spatial variability have been identified such as vegetation cover, soil texture, topography, and climate conditions (Famiglietti et al. 1998; Famiglietti 1999; Hupet and Vanclooster 2002; Teuling 2005; Brocca et al. 2007; Yeh et al. 1985). However, there does not appear to be a universal understanding of how spatial heterogeneity in soil water content varies with soil wetness. Some studies have reported less spatial heterogeneity in soil moisture under wet conditions (Famiglietti 1999; Hupet and Vanclooster 2002; Teuling 2005; Brocca et al. 2007), while other studies have reported the opposite (Hills and Reynolds 1969; Henninger et al. 1976; Bell et al. 1980; Famiglietti et al. 1998; Western and Grayson 1998; Teuling 2005). Moreover, some have reported greatest spatial heterogeneity in soil moisture under mid-range soil water contents (Owe et al. 1982; Albertson and Montaldo 2003; Famiglietti et al. 2008). In general, an understanding of soil moisture dynamics requires an analysis of sub-surface hydrology and boundary-layer processes (Entin et al. 2000; Brocca et al. 2007). Unfortunately, very few studies using this dual approach have focused on bare soils in arid areas (Williams et al. 2003).

The objectives of the paper are: (1) to determine how soil moisture affects the surface energy balance in an arid area; (2) to identify the key controlling mechanisms on evaporation after a rain event; (3) to explore the existence of nocturnal evaporation and investigate its main driving factors; (4) to characterize the spatial heterogeneity in soil moisture and evaporation rates. The analysis is supported by measurements made within the field experiment component of the Mountain Terrain Atmospheric Modeling and Observations (MATERHORN) program, designed to better understand atmospheric fluid dynamics across all scales over realistic mountainous terrain as well as under transient and steady conditions. The overall goal of MATERHORN project is to improve mountain weather forecasts by developing scientific tools to help identify leaps in predictability. More details can be found in Fernando and Pardyjak (2013) and Fernando et al. (2015).

2 Methods

2.1 Experimental Site Description

As part of the MATERHORN program, a spring field campaign was conducted from 1 to 31 May 2013 at the U.S. Army's Dugway Proving Ground (DPG), located about 137 km south-west of Salt Lake City, Utah. The DPG site is characterized by an arid climate with an annual cumulative precipitation of ≈100 mm and an annual cumulative evaporation of nearly 170 mm resulting in a net loss of water from the shallow water table (Malek 2003). The annual mean air temperature is ≈13.7 °C (Malek 2003). The terrain of the DPG site consists of sand dunes, salt flats and isolated hills surrounded by interconnected mountains, with sparse shrub steppe vegetation and very little human population. The main study area of interest here is a highly alkaline desert playa site (40°08′N, 113°27′W, 1296 m above mean sea level), which is mostly devoid of vegetation and characterized by a vast, barren and very flat surface, shallow water table and a heterogeneous soil moisture spatial distribution (Fig. 11a). The elevation variation on the playa is typically less than 1 m km^{-1}. The playa is ≈130 km long (north-south), and ≈65 km wide (east-west) and is located in the southern portion of the Great Salt Lake Desert.

The MATERHORN spring campaign contained ten Intensive Observation Periods (IOPs), during which extensive non-continuous datasets were collected (See Fernando et al. 2015 for details).

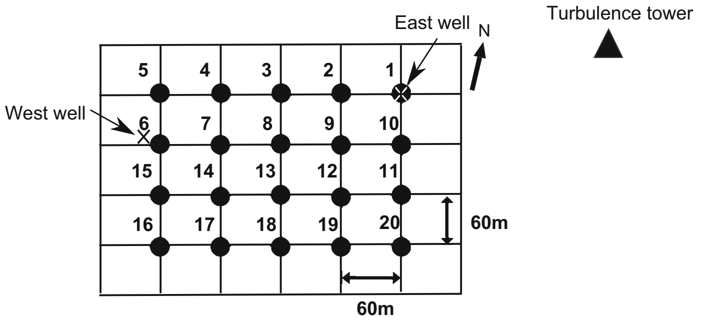

Fig. 1 Schematic illustrating the experiment layout (not to scale) with soil sampling sites (1–20) and the two wells monitoring the water table. The turbulence tower is located 200 m of the east well

2.2 Soil Moisture Content Sampling

2.2.1 Soil Sampling Transect

Soil moisture content was sampled at 20 sites evenly distributed on a 240 m × 180 m grid (Fig. 1). The grid size was selected to capture the typical length scale of wet and dry soil patches that are visible on the surface. Out of the 20 sampling sites, sites 1–17 were assigned to study the spatial heterogeneity of the playa soil. At these locations, soil from the surface layer (0–20 mm) and 50-mm layer (40–60 mm) were sampled. Here we assume that the spatial arrangement of wet and dry patches contained in our sampling grid is representative of the processes taking place at the playa scale. Sites 18–20 were used for mesoscale model validation purposes, which required extracting two soil cores from the layers 0 to 100 and 240 to 260 mm. Soil moisture was measured twice per IOP at sites 1–17, and once per IOP at sites 18–20, from the second IOP onwards (Table 1).

2.2.2 Moisture Content Sampling Method

Due to high salinity of the water in the playa soil, typical continuous moisture sampling probes such as reflectometers could not be used. As a result, volumetric water content (*VWC*) was measured directly using the gravimetric method (Johnson 1962). Soil samples were collected within a 1-m radius of each site by using a 25.4-mm gauge auger. The samples were taken sufficiently far from each other to prevent soil disruption throughout the field campaign. The soil samples were kept in pre-weighed tins immediately following extraction from the ground. The tins were sealed with electric tape and placed into plastic zipper bags. Once all of the samples were obtained, they were immediately weighed on-site before and after heating at 105 °C for at least 24 h. The precision of the scale was $\pm 10^{-5}$kg. The estimated uncertainty of *VWC* was found to be $\pm 0.012\,\mathrm{m}^3\,\mathrm{m}^{-3}$. In order to convert from mass to volume, the density of the water and soil were both measured in the field using the recommended USDA soil quality test kit guide (USDA 1999). The volumetric water content of each soil sample was taken as the ratio of the volume of the water inside of the soil to the volume of the dry soil. To characterize the spatial heterogeneity statistically, mean and standard deviations were computed over all sampling results for each IOP (e.g. mean surface-layer *VWC* during IOP2 was the average over all surface samples from the 17 sites during IOP2). The density of the saline water in the soil was found to be $\approx$1080 kg m^{-3} and the bulk density of the soil was 1426.2 kg m^{-3}.

Table 1 Surface (0–20 mm) temporal variability of playa soil moisture during the experimental period

IOP	Sampling time		*VWC* ($m^3\ m^{-3}$)		
	Start–final (MST)		Mean	Min/Max	Std
2	May 4	1411–1642	0.22	0.05/0.33	0.08
	May 5	0937–1026			
3	May 7	1353–1510	0.24	0.08/0.34	0.08
	–				
4	May 11	1200–1238	0.20	0.06/0.32	0.10
	May 12	0414–0604			
5	May 13	1845–1926	0.20	0.06/0.31	0.07
	May 14	0937–1026			
6	May 16	2219–0037	0.21	0.05/0.35	0.11
	–				
7	May 20	1325–1455	0.34	0.16/0.42	0.05
	May 21	0441–0526			
8	May 22	1351–1512	0.30	0.15/0.38	0.06
	May 23	0615–0700			
9	May 25	1028–1110	0.27	0.04/0.36	0.09
	May 25	0724–0811			
10	May 30	1904–1932	0.33	0.28/0.36	0.02
	–				

Std standard deviation

2.3 Other Measurements

To determine the evaporation and corresponding atmospheric variables at the playa site, we use 20-Hz data from a 28-m turbulence flux tower, which ran nearly continuously from 2 May to 5 June 2013. The tower was instrumented at six levels (0.6, 2.0, 5.3, 10.4, 19.4, 25.5 m) with Campbell Scientific, Inc. CSAT3 sonic anemometer/thermometers (Logan, UT) and HMP45C temperature/relative humidity sensors (Vaisala, Vantaa, Finland). Two EC150 CO_2/H_2O open-path gas analyzers (Campbell Scientific, Inc., Logan, UT) were deployed at 2.0 and 10.4 m above the surface. The eddy-covariance technique was applied to obtain sensible and latent heat fluxes using averaging periods of 30 min. More details on the turbulence flux corrections and quality control can be found in Jensen et al. (2015). The random flux uncertainty was estimated based on Lenschow et al. (1994). Here, we purposely did not exclude nocturnal data segments characterized by weak or ‘insufficient’ mechanical mixing. Indeed, given the closure of the surface energy balance at night (see Fig. 3), we have no indication that the latent heat fluxes are underestimated. The estimations of nocturnal evaporation reported in Sect. 3.2 are, in the worst case, conservative.

Thermal property sensors (TP01, Hukseflux, Delft, the Netherlands) were installed at a depth of 50 and 250 mm to measure soil thermal conductivity, soil thermal diffusivity, and volumetric heat capacity. The sub-surface heat flux at 50 mm depth was measured with self-calibrating heat-flux plates (HFP-SC, Hukseflux, the Netherlands). The ground heat flux at the surface was then calculated as the sum of the average measured ground heat flux at 50-mm depth (flux plate measurements) and the heat storage change in the 0 to 50-mm soil layer. The heat storage was calculated using the direct measurements of thermal heat capacities at 50 mm below the surface and soil temperatures at depths of 10, 25, and 50 mm. Given the low permeability of the soil, advective heat transport by rain infiltration was neglected. The individual shortwave and longwave components of the surface radiation balance were measured with up- and down-facing pyranometers and pyrgeometers (CMP21 and CGR4, Kipp & Zonen, the Netherlands) mounted horizontally 2 m above ground.

Finally, two Solinst Model 3001 Levelogger (Ontario, Canada) probes were installed at the field site (marked with an × in Fig. 1) to measure water table depth as it is a critical hydrological variable for dry lake beds (Tyler et al. 2006).

2.4 Soil Textures

As shown in Table 2, the study site is characterized by tremendous spatial variability in soil textures. In the top 250 mm, the soil texture is clay, silty clay or silty clay loam. In the surface soil layer (0–20 mm), the percentage of sand varies from 1 to 22 %, whereas silt varies from 24 to 55 % and clay from 41 to 62 %. All soil texture data were determined with the hydrometer method (Day 1965). Malek (2003) reported the surface salt content at a site ≈250 m to the north-east of the present measurement site, finding a soil electrical conductivity of 140 dS m^{-1} and a predominance of sodium, thereby explaining the white tinted surface soil colour.

3 Results and Discussion

3.1 Brief Climatology

Figure 2 shows a summary of basic hydrological and meteorological conditions during the field campaign at the playa site. Figure 2a reveals two main rain events in May 2013 (rainfall data obtained from a nearby automated weather station, 40°197′N, 113°167′W, 1299 m above mean sea level). The first occurred on 17–18 May 2013, with a cumulative rainfall of 15.8 mm, whereas the second took place on 28 May 2013, with a total rainfall of 10.2 mm. Figure 2a also shows the water-table depth fluctuations for part of the experimental period. Apart from a weak daily cycle possibly attributable to evaporative losses, we note two different time scales in the water table response to rainfall events. Following the first rain event, it took roughly 4 days for the water table to start rising, while for the second event it took only a day. One potential reason for these two different time scales is the antecedent soil moisture conditions. The last rain event before 17 May 2013 was 20 April 2013, allowing 30 days for soil to dry out. However, the second rain event occurred only 10 days after the first event, so, the antecedent soil moisture during the second event was higher than for the first rain event, which led to a more rapid response to the water table depth. Figure 2b shows the evolution of air temperature and wind speed throughout the experimental period, with air temperature varying between 1.8 and 34.1 °C, with an average of 17.4 °C. The mean 2-m wind speed was 4 $\mathrm{m\,s^{-1}}$ and reached a maximum of 17 $\mathrm{m\,s^{-1}}$ on 23 May at night. Figure 2c shows the evaporation rate measured using the eddy-covariance technique at the site from 2 May to 5 June 2013. The mean daily cumulative evaporation before 17 May 2013 was about 0.3 ± 0.2 mm. We note an increase in evaporation rates after the first rain event, followed by a sharp decay (see following section). The peak evaporation rates following the two rain events were 5.9 mm day^{-1} (±0.4 mm day^{-1}) and 8.3 mm day^{-1} (±0.3 mm day^{-1}) respectively. These events are discussed thoroughly in Sect. 3.2. Note that the cumulative evaporation for the entire experimental period was 19.3 mm (±1.5 mm) (73 % of the rainfall received during the campaign). The monthly averaged evaporation rate is 0.69 mm day^{-1}, which is consistent with the annual mean evaporation rate of 0.46 mm day^{-1} reported by Malek (2003).

Table 2 Playa soil texture analysis for Site 1–Site 17 following the USDA classification system (Soil Survey Staff 1999) as well as basic *VWC* statistics

Site number	Texture	Sand (%)	Silt (%)	Clay (%)	*VWC* (m^3m^{-3})		
					Mean	Min/Max	Std
1	SC	9	45	46	0.29	0.19/0.35	0.04
1 (40–60 mm)	SC	0	56	44	–	–	–
1 (200–250 mm)	SC	0	51	49	–	–	–
2	C	10	36	54	0.25	0.04/0.40	0.11
3	SC	1	48	51	0.19	0.05/0.34	0.09
4	C	16	30	54	0.20	0.07/0.32	0.09
5	C	14	31	55	0.20	0.06/0.33	0.09
6	SC	9	40	51	0.33	0.29/0.38	0.03
7	SC	1	55	44	0.29	0.17/0.37	0.06
8	SC	7	52	41	0.32	0.25/0.37	0.03
9	C	10	38	52	0.21	0.06/0.34	0.09
10	C	10	36	54	0.23	0.06/0.33	0.10
11	C	22	37	41	0.31	0.22/0.42	0.06
12	C	17	27	56	0.19	0.08/0.34	0.09
13	C	14	24	62	0.26	0.10/0.38	0.09
14	C	20	40	41	0.30	0.14/0.42	0.07
15	C	15	32	54	0.27	0.18/0.36	0.06
16	C	10	34	56	0.29	0.12/0.41	0.10
16 (40–60 mm)	SCL	16	44	40	–	–	–
16 (200–250 mm)	SCL	11	51	38	–	–	–
17	C	16	30	54	0.23	0.06/0.39	0.11
Mean		11.8	37.3	50.9	–	–	–
Min/Max		1/22	24/55	41/62			

Unless specified, the reported soil texture and *VWC* are averaged over the entire experimental period and are reported for the top 20-mm soil layer

SC: silty clay, C: clay, SCL: silty clay loam

3.2 Atmosphere–Soil Moisture Dynamics

Figure 3 shows the full surface energy balance around the first rain event, which occurred on 17–18 May 2013 (see Fig. 2a). Before the rain event, the peak value of net radiation was about 400 $\mathrm{W m^{-2}}$. During and after the rain event, the maximum net radiation exceeded 500 $\mathrm{W m^{-2}}$ and continued to do so for at least the next 3 days. As surface soil moisture increases following precipitation events, the surface albedo decreases, leading to reduced outgoing shortwave radiation flux densities and an increase in net radiation, especially under less cloudy conditions. Furthermore, as the most synoptically active month of the year, most of the data were obtained under cloudy conditions. Figure 3 also shows that the sensible heat flux decreased by a factor of ≈ 2 during the rain event. After approximately one day, the sensible heat flux returned to its pre-rainfall values. The nighttime sensible heat flux is very small (near zero), indicating near-neutral surface layer conditions on certain days (see also Jensen et al. 2015). As required, the latent heat fluxes show the same behaviour observed with

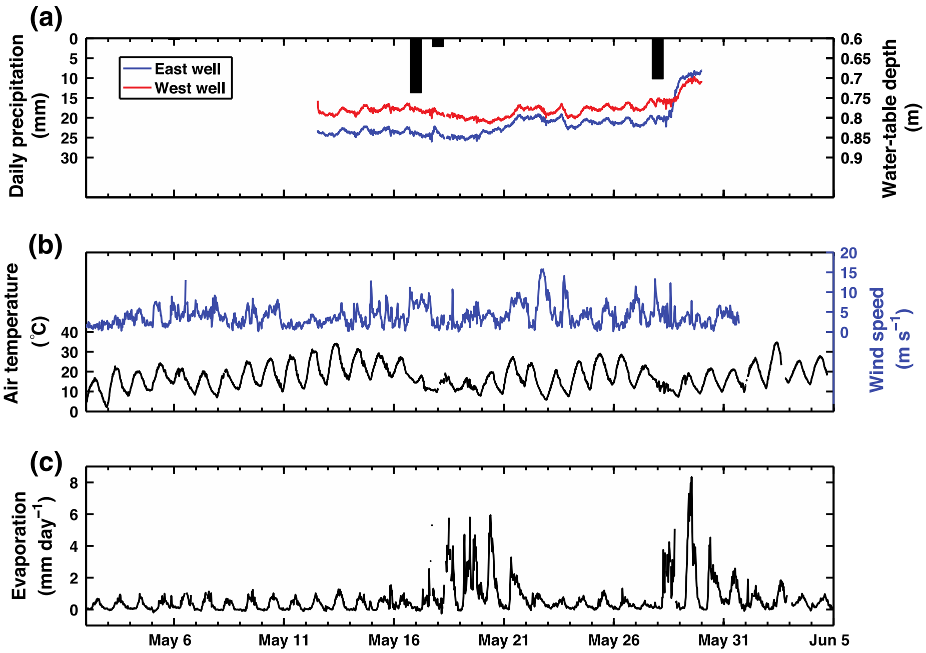

Fig. 2 **a** Daily precipitation and water-table level during the experimental period. **b** 5-min averages of air temperature and wind speed at 2 m above ground from the flux tower. **c** 30-min averages of evaporation rates measured 10 m above ground. *Error bars* are not included for readability

the evaporation rate shown in Fig. 2c. The magnitude of the ground heat flux increases during the rainfall and reaches its maximum value on 20 May 2013, partly because of variations in soil thermal conductivity. Indeed, before the rain event, the thermal conductivity was 0.71 W $(mK)^{-1}$ and immediately after, it increased to 0.85 W $(mK)^{-1}$. Due to the fact that the soil in this studied area is rich in clay, the advective transport of heat is very small and is thus neglected as previously mentioned. The magnitude of the daytime residual heat flux is about 100 Wm^{-2} before the rain, and increases to 200 Wm^{-2} for a brief period. As can be seen in Fig. 3, there are missing data, both due to the rain event and a brief power outage.

Several studies have reported exponential decay of evapotranspiration following a rain event (Williams and Albertson 2004; Teuling et al. 2006), and in order to relate evaporation to the soil moisture dynamics, the model presented in Teuling et al. (2006) is applied here. The model has a basic simplified terrestrial water balance under the assumptions that there is no rainfall and no runoff,

$$\frac{\mathrm{d}S(t)}{\mathrm{d}t} = -E(t), \tag{1}$$

and assumes evaporation E is proportional to the available soil moisture storage S with proportionality constant c. Then, Eq. 1 can be integrated from t_0 to t and written as,

$$E(t) = E_0 \exp\left(\frac{-(t-t_0)}{\lambda}\right), \tag{2}$$

where E_0 is the evaporation at $t = t_0$ (t_0 is specified as the first day following the rain event) and $\lambda = 1/c$ is a time scale controlling the temporal evolution of evaporation. If the evaporation rate is plotted as function of time on a semi-log plot (Fig. 4), E_0 is given by the

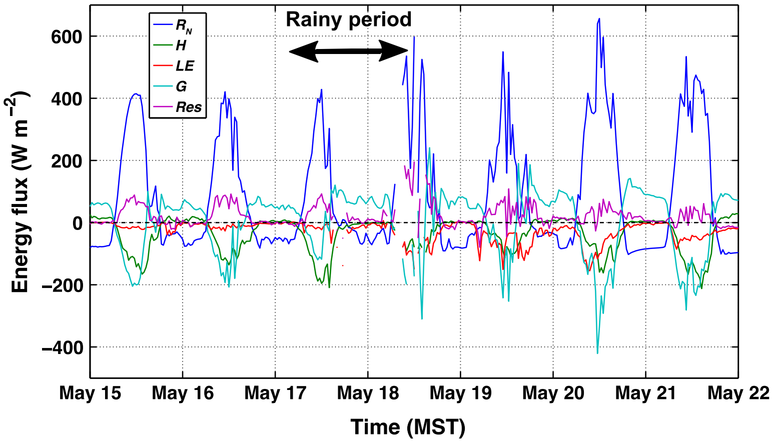

Fig. 3 Surface energy balance ($R_N + H + LE + G = Res$) for a six-day period centered on the first rain event (17 May 2013). Energy fluxes shown are 30-min averages (R_N net radiation, H sensible heat flux, LE latent heat flux, G ground heat flux, Res residual energy). More details on the surface energy balance can be found in Hoch et al. (2013, 2014)

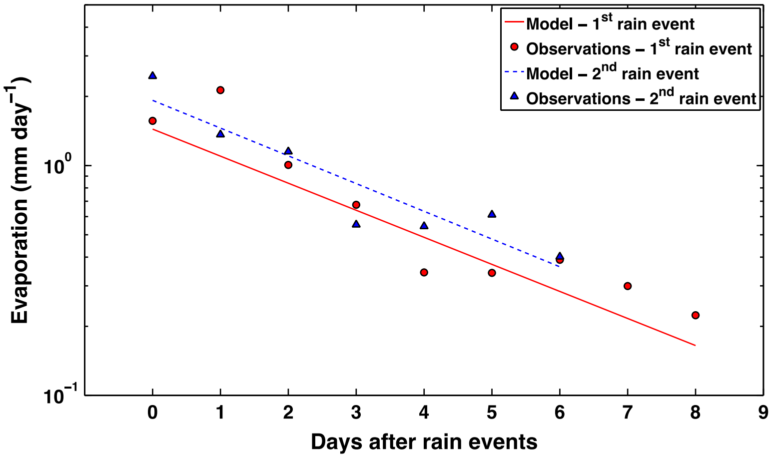

Fig. 4 Daily evaporation at the field site following two rain events. The model evaluated here is the one from Teuling et al. (2006) (see Eq. 2). The first rain event took place on 17–18 May 2013 and the second on 28 May 2013

intercept with the ordinate obtained using a linear regression. In order to connect the time scale λ to the soil moisture dynamics, a storage term S_0 is defined as soil moisture depleted following a complete drydown ($t \rightarrow \infty$),

$$S_0 = \int_{t_0}^{\infty} E(t)\mathrm{d}t = \lambda E_0 \tag{3}$$

In their study, Teuling et al. (2006) report λ and S_0 values for a wide range of surface types and climate conditions. During the MATERHORN field experiment, the mean e-folding time was found to be $\lambda = 3.64$ days, and $S_0 = 6.12$ mm, values that are much smaller than those reported in Teuling et al. (2006). In fact, the minimum λ and S_0 from their Table 2 are 12.4 days and 28.1 mm respectively. We believe that the short e-folding time is due to the high

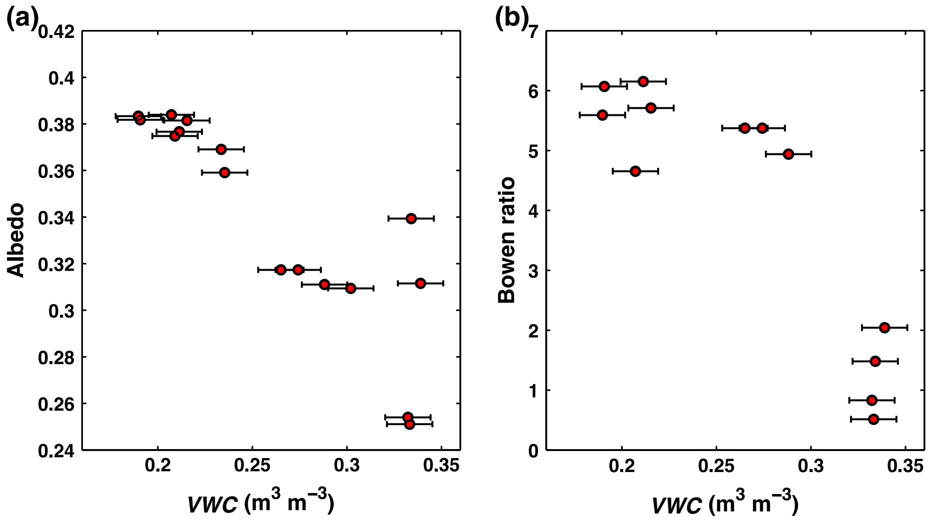

Fig. 5 *Left* Average daytime surface albedo versus mean volumetric water content (*VWC*) for each IOP. *Right* Average daytime Bowen ratio versus mean volumetric water content for each IOP

atmospheric drying demand at the playa site, to the fine texture of the soil retaining rainwater close to the surface, and to the existence of positive feedback mechanisms promoting fast surface drying after a rain event. On the other hand, the low storage volume is possibly a result of the soil properties and shallow water table position at the field site.

As shown in Table 2, the surface soil texture at the playa is mainly clay, which has a very low permeability due to its fine texture. Furthermore, clay rich soil has a relatively high water capacity. As a result, water is kept near the surface after the rain events, which promotes large evaporation rates.

As a starting point to investigate processes responsible for the unusually rapid surface drying following a rain event, we focus on two key determinants of the energy budget: the playa surface albedo and Bowen ratio. Figure 5a presents variations of surface albedo as a function of *VWC* in the surface layer, where we see that the surface albedo increases by up to a factor of 1.5 in response to a drying surface. In terms of energy fluxes, this reduction of 0.13 in surface albedo translates into an increase of 80 W m^{-2} given the typical conditions at the site. Figure 5b shows the relationship between the daytime Bowen ratio and surface soil moisture, with the Bowen ratio taken as the ratio of the mean daytime sensible heat flux to latent heat flux. The Bowen ratio varies greatly, from ≈ 6 to 0.5 as *VWC* in the surface layer increases. The variation of Bowen ratio under dry and medium soil moisture conditions ($VWC \approx 0.18$–$0.29\,\mathrm{m}^3\,\mathrm{m}^{-3}$) is relatively small, but under wet conditions ($VWC \approx 0.29$–$0.34\,\mathrm{m}^3\,\mathrm{m}^{-3}$) it increases sharply from about 5 to 0.5, i.e. by a factor of 10. In essence, Fig. 5 shows that both surface albedo and Bowen ratio decrease with increasing surface wetness, a well-known relationship.

Given that there is more energy available at the surface under wet conditions, one needs to investigate how this excess energy is redistributed. Figure 6 shows sensible (H), latent (*LE*) and ground (G) heat fluxes normalized by net radiation (R_{N}). The 30-min averaged data of all the heat fluxes are integrated over a 24-h period, which imply values of the daily total heat transfer. The daily total net radiation increases from 6.2 to 12.5 MJ m^{-2} with increasing wetness. Figure 6a illustrates that the integrated sensible heat flux has a slightly increasing

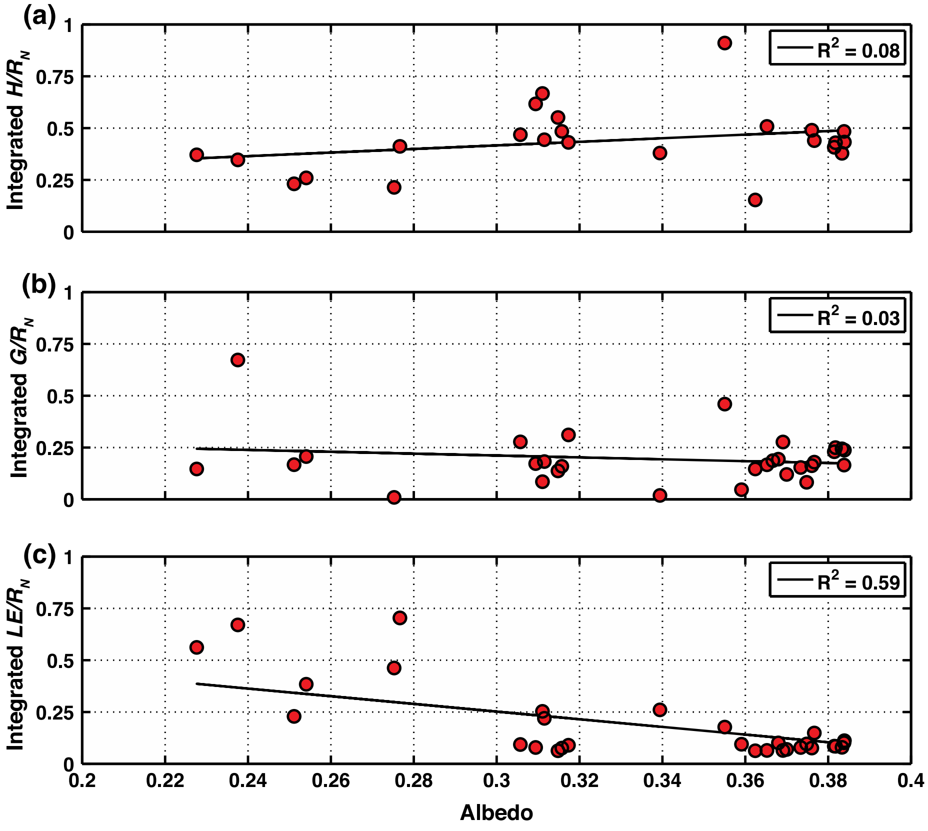

Fig. 6 **a** Integrated sensible heat flux over 1 day normalized by daily-averaged net radiation versus daily averaged surface albedo. **b** Integrated ground heat flux over a day normalized by daily-averaged net radiation versus daily-averaged surface albedo. **c** Integrated latent heat flux over a day normalized by daily-averaged net radiation versus daily-averaged surface albedo

trend with increasing albedo. Under relatively low-albedo conditions (0.22–0.31), integrated H/R_N increases from about 0.2 to 0.5 and then levels off when surface albedo is greater than 0.32. This indicates that the temperature difference between the soil surface and the overlying air increases under moist low-albedo conditions. Figure 6b does not show any clear relation between the integrated G and albedo as indicated by the very small correlation coefficient. This can be explained by the balance of increasing soil thermal conductivity and decreasing temperature difference when the albedo becomes smaller (greater soil moisture content). Figure 6c shows a decreasing trend of integrated LE/R_N as albedo increases. The integrated LE decreases from ≈0.6 to 0.1 under small albedo conditions, and then appears to plateau when surface albedo exceeds 0.36. In summary, when the soil moisture content increases (i.e. after a rain event), the surface albedo decreases and the additional energy is used to evaporate more water and thus accelerate surface drying.

We hypothesize that nocturnal evaporation is another factor behind the positive surface drying feedback mechanism. Figure 7 shows that nocturnal evaporation (obtained from the eddy-covariance measurements) can account for up to 30 % of the cumulative daily evaporation, although it is usually in the range 0–10 %. Note that this has implications for traditional radiation-based evaporation relations such as that of Priestley and Taylor (1972), which

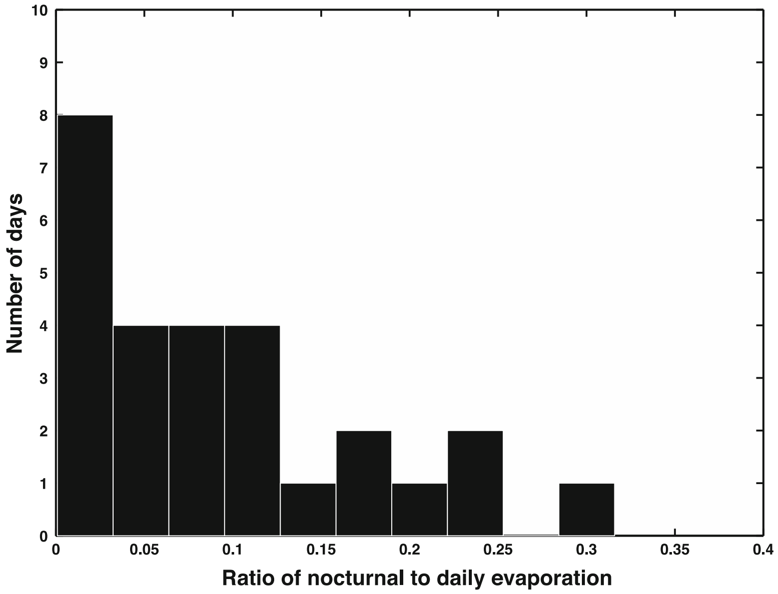

Fig. 7 Histogram of the ratio of nocturnal to daily cumulative evaporation for the full experimental period

assume that nighttime evaporation is non-existent. The use of such relations over long time periods could lead to an underestimation of the actual water vapour transfer.

To investigate the driving process related to nocturnal evaporation, Fig. 8 shows the cumulative nocturnal evaporation versus the mean atmospheric drying power (a–c) and surface soil moisture content (d). Note that the *VWC* data are available exclusively during the IOP periods, which focused on daytime conditions. Thus, Fig. 8d represents nighttime evaporation versus the corresponding *VWC* values for the equivalent day. Negative evaporation indicates that on certain days, weak condensation occurs, although these values may result from random flux errors. There is no clear relation between cumulative nocturnal evaporation and atmospheric drying demand. In most cases, no matter how the atmospheric dying power changes, total nighttime evaporation only varies slightly from zero to 0.1 mm (Fig. 8a–c). However, nocturnal evaporation is positively correlated with *VWC* (Fig. 8d); therefore, in arid areas devoid of vegetation such as playas, nocturnal evaporation is essentially limited by water availability, as one would expect.

3.3 Spatial Heterogeneity of Soil Moisture and Evaporation

Figure 9 shows the spatial standard deviation of *VWC* values in the soil surface layer computed with data from all IOPs at sites 1–17. In the surface soil layer, the spatial heterogeneity increases as the soil becomes drier. Under the driest surface conditions, the coefficient of variation is 50 %, while under the wettest conditions it decreases to 14 %. Yeh et al. (1985) were the first to postulate that increased heterogeneities under dry conditions were due to variations in soil texture, as is likely the case here. This surface variability was evident in visual observations of persistent moist and dry regions throughout the playa (Fig. 11a). However, at greater soil depths, less heterogeneity is observed until eventually the soil becomes saturated. Thus, there is no clear relation between mean soil moisture and its standard deviation in the 50-mm layer. As expected, a larger range of soil moisture conditions was found in the surface

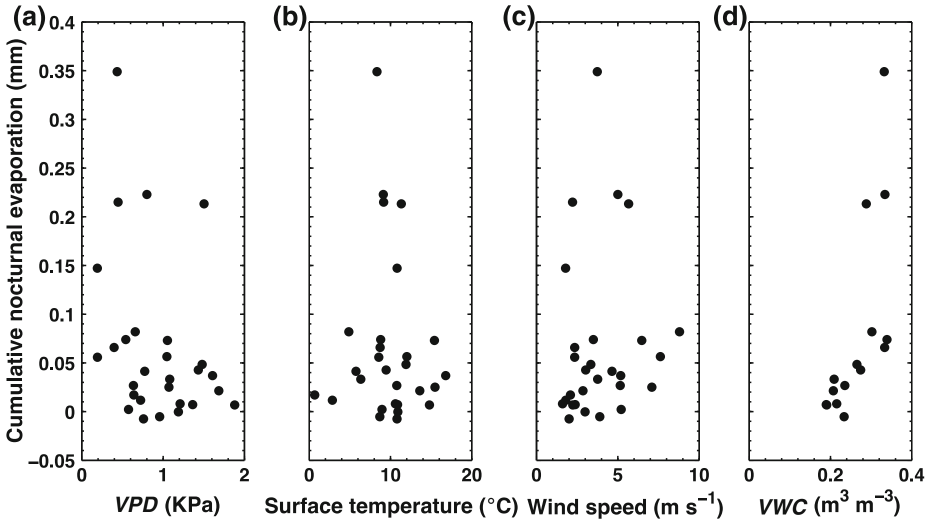

Fig. 8 Nocturnal cumulative evaporation (mm) versus: **a** vapour pressure deficit (*VPD*); **b** soil surface temperature; **c** wind speed measured 2 m above ground; **d** surface volumetric water content (*VWC*)

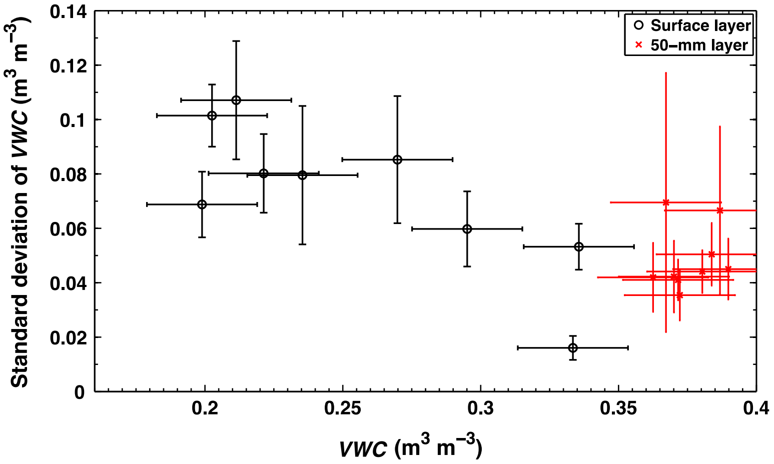

Fig. 9 Standard deviation of volumetric water content in the surface soil layer and 50-mm soil layer versus mean volumetric water content. Standard deviation of *VWC error bars* represent 95 % confidence intervals calculated with a jackknife resampling algorithm (Tukey 1958). *VWC error bars* represent the mean error of soil sampling

layer, where it varied from 0.20 to 0.34 m^3 m^{-3}. In the 50-mm layer, *VWC* covered the range 0.36–0.39 m^3 m^{-3}.

One would expect spatial heterogeneity in soil moisture to translate into heterogeneity in evaporation rates. To investigate this, we used the soil moisture depletion technique (Johnston et al. 1969) at each of our 17 sampling sites with soil water profiles obtained, by solving Richards equation with a simple finite difference model (Clapp and Hornberger 1978; McCumber 1980; Shingleton 2010 for more detail on the model). As the top boundary condition, we used our surface soil moisture measurements, whereas for the bottom boundary

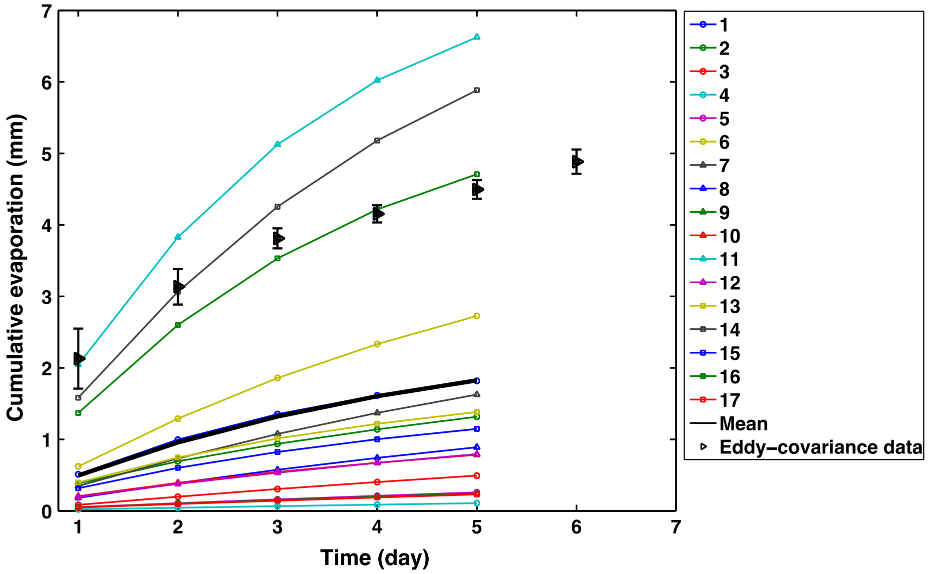

Fig. 10 Cumulative evaporation for each of the 17 soil sampling sites as determined from the soil depletion method and the eddy-covariance measurements. *Error bars* on eddy-covariance data represent the estimated random errors of daily evaporation

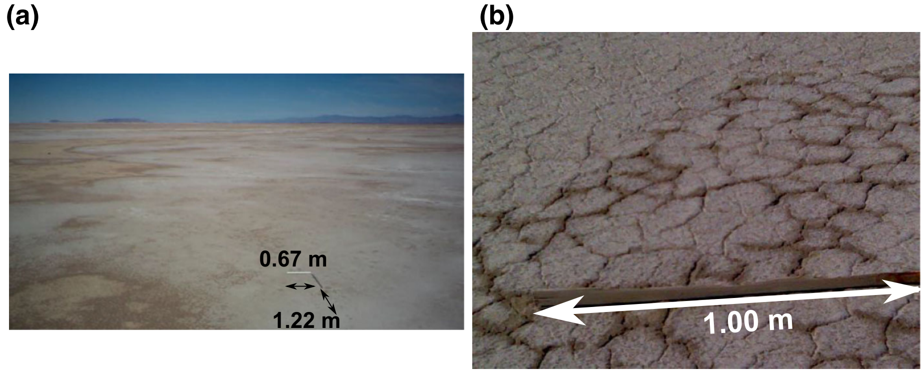

Fig. 11 **a** Large-scale visible photograph of the desert playa (19 June 2014 1335 MST); **b** small-scale visible photograph showing desiccation cracks (23 July 2014 1530 MST)

conditions (0.8 m below the surface) we assumed a saturated soil with $VWC = 0.46\,\mathrm{m}^3\,\mathrm{m}^{-3}$. We validated the model by comparing the variations of 50-mm soil moisture after the rain event on May 17–18. Although this is far from an exhaustive validation, the differences between observational and modelled values were relatively small and considered sufficiently good to proceed with the analysis. Figure 10 shows substantial variability in evaporation rates among the 17 sampling sites. The cumulative evaporation on the first day after the last rain event varies from $\approx$0 to 2.0 mm. However, the values of total evaporation after 5 days changes from $\approx$0.1 to $\approx$6.6 mm, which indicates strong heterogeneity over these 17 sites. As expected, most of the sites with smaller-than-average evaporation are usually relatively dry ($VWC < 0.2\,\mathrm{m}^3\,\mathrm{m}^{-3}$) and vice versa. In essence, Fig. 10 illustrates the underlying spatial variability in evaporation rates, which an 'integrated' measurement approach such as the eddy-covariance method is unable to detect.

As highlighted by Brutsaert (1998), spatial heterogeneity in soil moisture (and thus water vapour fluxes) exists at multiple scales. Figure 11 shows visible photographs of the playa site at two scales. At large scales (Fig. 11a), clear dry (brown) and wet (white) patches are found and are likely associated with sharp local gradients in evaporation rates. Heterogeneity is also found at small scales (Fig. 11b), where water vapour is evacuated through small desiccation cracks. This illustrates that even under a priori homogeneous surfaces, spatial heterogeneity has to be taken into account.

4 Conclusions

This study focuses on mechanisms controlling desert playa soil moisture dynamics as well as evaporation following occasional rain events. The analysis is based on observational data collected as part of the MATERHORN program in May 2013. This month is typically the most synoptically active month of the year, and while there were only two significant rain events during the month, total precipitation (25 mm) did exceed cumulative evaporation (19 mm). Hence, the month was relatively wet compared to the annual averages where evaporation exceeds precipitation.

Regarding the temporal variability of soil moisture, a fast positive feedback mechanism promoting surface drying after precipitation events was observed. Following rainfall, surface albedo and Bowen ratio decreased from 0.38 to 0.25 and from 6 to 0.5 respectively, while net radiation increased by 25 %. The evaporation rate reached its maximum value one day after the rain event, and then decayed exponentially. The associated *e*-folding time scale is much smaller than values previously reported in the literature. An additional contributing factor to the positive drying feedback mechanism is nocturnal evaporation. Furthermore, the clay soil at the playa site is characterized by low permeability and a relatively large water holding capacity, which holds water near the surface and is available for evaporation. On several nights following rain events, the ratio of nocturnal to daily cumulative evaporation reached up to 30 %. Near-surface volumetric water content has a bigger impact than they do vapour pressure deficit, surface temperature and wind speed.

High spatial variability of surface soil moisture and soil texture was also investigated on an experimental grid. The spatial heterogeneity was found to be significant in the top 20-mm layer, with a *VWC* standard deviation of $0.07\,\mathrm{m^3\,m^{-3}}$, and negligible deeper into the soil, with a *VWC* standard deviation of $0.05\,\mathrm{m^3\,m^{-3}}$. Cumulative evaporation after rain events shows the presence of strong heterogeneity in evaporation rates under wet soil conditions (relatively low variability). The total evaporation after 5 days varied from ≈0.1 to ≈6.6 mm. Some evidence of a positive feedback mechanism over a desert playa site was observed, and additionally we also identified strong spatial heterogeneity at different scales for playa sites.

Acknowledgments This research was funded by the Office of Naval Research Award #N00014-11-1-0709, Mountain Terrain Atmospheric Modeling and Observations (MATERHORN) Program. The authors thank Daniel Alexander for his help with the finite difference model of the Richard's equation used to compute soil moisture profiles. The authors are also grateful to Dr. Dragan Zajic, John Pace and Nipun Gunawardena whose contributions were critical to the success of the field measurements. We are also extremely grateful for all of the help in the field, and the scientific insight provided by the MATERHORN team, especially Prof. H.J.S. Fernando.

References

Albertson JD, Montaldo N (2003) Temporal dynamics of soil moisture variability: 1. Theoretical basis. Water Resour Res 39:1274

Allison GB, Barnes CJ (1985) Estimation of evaporation from the normally "dry" Lake Frome in South Australia. J Hydrol 78(3):229–242

Avissar R, Pielke RA (1989) A parameterization of heterogeneous land surfaces for atmospheric numerical models and its impact on regional meteorology. Mon Weather Rev 117:2113–2136

Bell KR, Blanchard BJ, Schmugge TJ, Witczak MW (1980) Analysis of surface moisture variations within large-field sites. Water Resour Res 16:796–810

Black TA, Gardner WR, Thurtell GW (1969) The prediction of evaporation, drainage, and soil water storage for a bare soil. Soil Sci Soc Am J 33:655

Brocca L, Morbidelli R, Melone F, Moramarco T (2007) Soil moisture spatial variability in experimental areas of central Italy. J Hydrol 333:356–373

Brutsaert, W. (1998). Landsurface water vapor and sensible heat flux: Spatial variability, homogeneity, and measurement scales. Water Resour Res 34(10), 2433–2422

Brutsaert W, Chen D (1995) Desorption and the two stages of drying of natural tallgrass prairie. Water Resour Res 31:1305–1313

Burgess SSO, Adams MA, Turner NC, Ong CK (1998) The redistribution of soil water by tree root systems. Oecologia 115:306–311

Clapp R, Hornberger G (1978) Empirical equations for some soil hydraulic properties. Water Resour Res 14:601–604

D'Odorico P, Porporato A (2006) Dryland ecohydrology. Springer, Dordrecht, 341 pp

Dawson TE, Burgess SSO, Tu KP, Oliveira RS, Santiago LS, Fisher JB, Simonin KA, Ambrose AR (2007) Nighttime transpiration in woody plants from contrasting ecosystems. Tree Physiol 27:561–575

Day PR (1965) Particle fractionation and particle-size analysis. In: Black CA (ed) Methods of soil analysis, part 1. American Society of Agronomy No. 9, Madison, pp 545–567

Ek MB, Holtslag AAM (2004) Influence of soil moisture on boundary layer cloud development. J Hydrometeorol 5:86–99

Eltahir E (1998) A soil moisture-rainfall feedback mechanism 1. Theory and observations. Water Resour Res 34:765–776

Entin JK, Robock A, Vinnikov KY, Hollinger SE, Liu S, Namkhai A (2000) Temporal and spatial scales of observed soil moisture variations in the extratropics. J Geophys Res 105:11865

Famiglietti JS (1999) Ground-based investigation of soil moisture variability within remote sensing footprints during the southern great plains 1997. Water Resour Res 35:1839–1851

Famiglietti JS, Rudnicki JW, Rodell M (1998) Variability in surface moisture content along a hillslope transect: Rattlesnake Hill, Texas. J Hydrol 210:259–281

Famiglietti JS, Ryu D, Berg AA, Rodell M, Jackson TJ (2008) Field observations of soil moisture variability across scales. Water Resour Res 44:W01423

Fernando HJS, Pardyjak ER (2013) Field studies delve into the intricacies of mountain weather. Eos Trans Am Geophys Union 94:313–320

Fernando HJS, Pardyjak ER, Di Sabatino S, Chow FK, De Wekker SFJ, Hoch SW, Hacker J, Pace JC, Pratt T, Pu Z, Steenburgh JW, Whiteman CD, Wang Y, Zajic D, Balsley B, Dimitrova R, Emmitt GD, Higgins CW, Hunt JCR, Knievel JC, Lawrence D, Liu Y, Nadeau DF, Kit E, Blomquist BW, Conry P, Coppersmith RS, Creegan E, Felton M, Grachev A, Gunawardena N, Hang C, Hocut CM, Huynh G, Jeglum ME, Jensen D, Kulandaivelu V, Lehner M, Leo LS, Liberzon D, Massey JD, McEnerney K, Pal S, Price T, Sghiatti M, Silver Z, Thompson M, Zhang H, Zsedrovits T (2015) The MATERHORN—unraveling the intricacies of mountain weather. Bull Am Meteorol Soc. doi:10.1175/BAMS-D-13-00131.1

Fisher J, Baldocchi D (2007) What the towers don't see at night: nocturnal sap flow in trees and shrubs at two AmeriFlux sites in California. Tree Physiol 27:597–610

Gowing JW, Konukcu F, Rose DA (2006) Evaporative flux from a shallow watertable: the influence of a vapour–liquid phase transition. J Hydrol 321(1–4):77–89

Henninger DL, Petersen GW, Engman ET (1976) Surface soil moisture within a watershed—variations, factors influencing, and relationship to surface runoff. Soil Sci Soc Am J 40:773

Hills RC, Reynolds SG (1969) Illustrations of soil moisture variability in selected areas and plots of different sizes. J Hydrol 8:27–47

Hoch SW, Jensen D, Pardyjak ER, Whiteman CD, Fernando HJ (2013) Surface energy balance observations during MATERHORN. In: 32nd International Conference on Alpine Meteorology, Kranjska Gora, Slovenia, 3–7 June 2013

Hoch SW, Jensen D, Massey JD, Pardyjak ER, Fernando HJS (2014) Surface energy balance observations during MATERHORN. In: 16th American Meteorological Society Conference on Mountain Meteorology, San Diego, CA, 18–22 Aug 2014

Hupet F, Vanclooster M (2002) Intraseasonal dynamics of soil moisture variability within a small agricultural maize cropped field. J Hydrol 261:86–101

Idso S, Jackson R (1975) The dependence of bare soil albedo on soil water content. J Appl Meteorol Climatol 14:109–113

Ivanov VY, Fatichi S, Jenerette GD, Espeleta JF, Troch Pa, Huxman TE (2010) Hysteresis of soil moisture spatial heterogeneity and the "homogenizing" effect of vegetation. Water Resour Res 46:W09521

Jensen DD, Nadeau DF, Hoch SW, Pardyjak ER (2015) Observations of near-surface heat flux and temperature profiles through the early evening transition over contrasting surfaces. Boundary-Layer Meteorol. doi:10.1007/s10546-015-0067-z

Johnson A (1962) Methods of measuring soil moisture in the field. US Government Printing Office, Washington, 25 pp

Johnston RS, Doty RD, Tew RK (1969) Soil moisture depletion and estimated evapotranspiration on Utah mountain watershed. USDA Forest Service – Research Papers International-67

Katul GG, Parlange MB (1992) Estimation of bare soil evaporation using skin temperature measurements. J Hydrol 132:91–106

Koster R, Suarez M (2003) Observational evidence that soil moisture variations affect precipitation. Geophys Res Lett 30:1241

Lawrence JE, Hornberger GM (2007) Soil moisture variability across climate zones. Geophys Res Lett 34:L20402

Lenschow DH, Mann J, Kristensen L (1994) How long is long enough when measuring fluxes and other turbulence statistics. J Atmos Ocean Technol 11:661–673

Malek E (2003) Microclimate of a desert playa: evaluation of annual radiation, energy, and water budgets components. Int J Climatol 23:333–345

Malek E, Bingham GE, McCurdy GD (1990) Evapotranspiration from the margin and moist playa of a closed desert valley. J Hydrol 120:15–43

Massey JD, Steenburgh WJ, Hoch SW, Knievel JC (2014) Sensitivity of near-surface temperature forecasts to soil properties over a sparsely vegetated dryland region. J Appl Meteorol Climatol 53:1976–1995

McCumber MC (1980) Numerical simulation of the influence of heat and moisture fluxes upon mesoscale circulations. PhD Thesis, University of Virginia

Menenti M (1984) Physical aspects and determination of evaporation in deserts applying remote sensing techniques. PhD Thesis, Netherlands Agricultural University

Mittelbach H, Seneviratne SI (2012) A new perspective on the spatio-temporal variability of soil moisture: temporal dynamics versus time-invariant contributions. Hydrol Earth Syst Sci 16:2169–2179

Novick KA, Oren R, Stoy PC, Siqueira MBS, Katul GG (2009) Nocturnal evapotranspiration in eddy-covariance records from three co-located ecosystems in the Southeastern U.S.: implications for annual fluxes. Agric For Meteorol 149:1491–1504

Oishi aC, Oren R, Stoy PC (2008) Estimating components of forest evapotranspiration: a footprint approach for scaling sap flux measurements. Agric For Meteorol 148:1719–1732

Ookouchi Y, Segal M, Kessler RC, Pielke RA (1984) Evaluation of soil moisture effects on the generation and modification of mesoscale circulations. Mon Weather Rev 112:2281–2292

Owe M, Jones EB, Schmugge TJ (1982) Soil moisture variation patterns observed in hand county, South Dakota. J Am Water Resour Assoc 18:949–954

Parlange MB, Katul GG, Cuenca RH, Kavvas ML, Nielsen DR, Mata M (1992) Physical basis for a time series model of soil water content. Water Resour Res 28:2437–2446

Philip JR (1957) Evaporation, and moisture and heat fields in the soil. J Meteorol 14:354–366

Priestley CHB, Taylor RJ (1972) On the assessment of surface heat flux and evaporation using large-scale parameters. Mon Weather Rev 100:81–92

Rife DL, Warner TT, Chen F, Astling EG (2002) Mechanisms for diurnal boundary layer circulations in the Great Basin Desert. Mon Weather Rev 130:921–938

Scanlon BR, Goldsmith RS (1997) Field study of spatial variability in unsaturated flow beneath and adjacent to playas. Water Resour Res 33:2239–2252

Schär C, Lüthi D, Beyerle U, Heise E (1999) The soil-precipitation feedback: a process study with a regional climate model. J Clim 12:722–741

Segal M, Garratt JR, Kallos G, Pielke RA (1989) The impact of wet soil and canopy temperatures on daytime boundary-layer growth. J Atmos Sci 46:3673–3684

Seneviratne SI, Corti T, Davin EL, Hirschi M, Jaeger EB, Lehner I, Orlowsky B, Teuling AJ (2010) Investigating soil moisture–climate interactions in a changing climate: a review. Earth Sci Rev 99:125–161

Shingleton N (2010) Coupling a land-surface model to large-eddy simulation to study the nocturnal boundary layer. MSc Thesis, The University of Utah

Soil Survey Staff (1999) Soil taxonomy: a basic system of soil classification for making and interpreting soil surveys. Agricultural handbook 438; Natural Resources Conservation Service, USDA, Washington DC, USA, 869 pp

Teuling AJ (2005) Improved understanding of soil moisture variability dynamics. Geophys Res Lett 32:L05404

Teuling AJ, Seneviratne SI, Williams C, Troch PA (2006) Observed timescales of evapotranspiration response to soil moisture. Geophys Res Lett 33:L23403

Teuling AJ, Hupet F, Uijlenhoet R, Troch PA (2007) Climate variability effects on spatial soil moisture dynamics. Geophys Res Lett 34:L06406

Tukey JW (1958) Bias and confidence in not-quite large samples. Ann Math Stat 29:614

Tyler SW, Muñoz JF, Wood WW (2006) The response of playa and sabkha hydraulics and mineralogy to climate forcing. Ground Water 44:329–38

USDA (1999) Soil quality test kit guide. USDA, Washington DC, USA, 82 pp

Vivoni ER, Gebremichael M, Watts CJ, Bindlish R, Jackson TJ (2008) Comparison of ground-based and remotely-sensed surface soil moisture estimates over complex terrain during SMEX04. Remote Sens Environ 112:314–325

Vivoni ER, Rodríguez JC, Watts CJ (2010) On the spatiotemporal variability of soil moisture and evapotranspiration in a mountainous basin within the North American monsoon region. Water Resour Res 46:W02509

Warner TT (2004) Desert meteorology. Cambridge University Press, Cambridge, 595pp

Western AW, Grayson RB (1998) The Tarrawarra data set: soil moisture patterns, soil characteristics, and hydrological flux measurements. Water Resour Res 34:2765–2768

Whitaker M (1993) Small-scale spatial variability of soil moisture and hydraulic conductivity in a semi-arid rangeland soil in Arizona. MS Thesis, The University of Arizona

Williams AG, Ternan JL, Fitzjohn C, de Alba S, Perez-Gonzalez A (2003) Soil moisture variability and land use in a seasonally arid environment. Hydrol Process 17:225–235

Williams CA, Albertson JD (2004) Soil moisture controls on canopy-scale water and carbon fluxes in an African savanna. Water Resour Res 40:W09302

Yechieli Y, Wood WW (2002) Hydrogeologic processes in saline systems: playas, sabkhas, and saline lakes. Earth Sci Rev 58:343–365

Yeh TCJ, Gelhar LW, Gutjar GAL (1985) Stochastic analysis of unsaturated flow in heterogeneous soils: 3. Observations and applications. Water Resour Res 21:465–471

Zheng X, Eltahir E (1998) A soil moisture-rainfall feedback mechanism 2. Numerical experiments. Water Resour Res 34:777–785

Zhou X, Geerts B (2013) The influence of soil moisture on the planetary boundary layer and on cumulus convection over an isolated mountain. Part I: observations. Mon Weather Rev 141:1061–1078

CHAPTER 3

THE MECHANISMS MODULATING THE EVOLUTION OF VALLEY FOG

The article in this chapter was originally published in *Pure and Applied Geophysics* (2016) **173**, 3011–3030. Reprinted with the kind permission of Springer International Publishing.

Pure Appl. Geophys. 173 (2016), 3011–3030

DOI 10.1007/s00024-016-1370-4

Pure and Applied Geophysics

A Case Study of the Mechanisms Modulating the Evolution of Valley Fog

C. Hang,[1] D. F. Nadeau,[2] I. Gultepe,[3] S. W. Hoch,[4] C. Román-Cascón,[5] K. Pryor,[6] H. J. S. Fernando,[7,8]
E. D. Creegan,[9] L. S. Leo,[7] Z. Silver,[7] and E. R. Pardyjak[1]

Abstract—We present a valley fog case study in which radiation fog is modulated by topographic effects using data obtained from a field campaign conducted in Heber Valley, Utah from January 7–February 1, 2015, as part of the Mountain Terrain Atmospheric Modeling and Observations (MATERHORN) program. We use data collected on January 9, 2015 to gain insight into relationships between typical shallow radiation fog, turbulence, and gravity waves associated with the surrounding topography. A $\approx$ 10–30 m fog layer formed by radiative cooling was observed from 0720 to 0900 MST under cold air temperatures (≈ -9 °C), near-saturated (relative humidity with respect to water $\approx$95 %), and calm wind (mostly $<$0.5 m s^{-1}) conditions. Drainage flows were observed occasionally prior to fog formation, which modulated heat exchanges between air masses through the action of internal gravity waves and cold-air pool sloshing. The fog appeared to be triggered by cold-air advection from the south ($\approx$200°) at 0700 MST. Quasi-periodic oscillations were observed before and during the fog event with a time period of about 15 min. These oscillations were detected in surface pressure, temperature, sensible heat flux, incoming longwave radiation, and turbulent kinetic energy measurements. We hypothesize that the quasi-periodic oscillations were caused by atmospheric gravity waves with a time period of about 10–20 min based on wavelet analysis. During the fog event, internal gravity waves led to about 1 °C fluctuations in air temperatures. After 0835 MST when net radiation became positive, fog started to dissipate due to the surface heating and heat absorption by the fog particles. Overall, this case study provides a concrete example of how fog evolution is modulated by very weak thermal circulations in mountainous terrain and illustrates the need for high density vertical and horizontal measurements to ensure that the highly spatially varying physics in complex terrain are sufficient for hypothesis testing.

Key words: Ice fog, internal gravity wave, mountain complex terrain, radiation fog, turbulence–wave interaction.

1. *Introduction*

Fog is defined as a near-surface air mass with suspended water droplets and/or ice crystals that reduces horizontal visibility to less than 1 km (NOAA 1995). Understanding fog evolution processes is critical in populated areas due to its effect on ground transportation, air traffic, vegetation health and air quality (Gultepe et al. 2007). Although the processes associated with fog formation, evolution and dissipation are extremely important, they are still not fully understood, especially, in the areas of complex terrain (Golding 1993; Müller et al. 2007; Price et al. 2011). The difficulties in predicting fog arise from the nonlinear interactions between simultaneous atmospheric processes, such as aerosol chemistry, droplet microphysics, radiative transfer, turbulent mixing, and moisture deposition (Gultepe et al. 2007).

Fog frequently forms in river valley bottoms, where moisture is plentiful and cold air accumulates due to drainage flows. These valley fogs are radiation fogs modulated by topographic effects such as slope flows and mountain-generated gravity waves. Several field studies have been conducted across the world to analyze valley fogs, including in the Chemung River Valley (Pilié et al. 1975), the Hudson Valley

---

[1] Department of Mechanical Engineering, University of Utah, Salt Lake City, UT, USA. E-mail: pardyjak@eng.utah.edu
[2] Department of Civil and Water Engineering, Université Laval, Quebec City, QC, Canada.
[3] Cloud Physics and Severe Weather Research Section, Environment Canada, Toronto, ON, Canada.
[4] Department of Atmospheric Sciences, University of Utah, Salt Lake City, UT, USA.
[5] Departamento de Geofísica y Meteorología, Universidad Complutense de Madrid, Madrid, Spain.
[6] Center for Satellite Applications and Research, National Oceanic and Atmospheric Administration, National Environmental Satellite, Data, and Information Service, Camp Springs, MD, USA.
[7] Department of Civil and Environmental Engineering and Earth Sciences, University of Notre Dame, Notre Dame, IN, USA.
[8] Department of Aerospace and Mechanical Engineering, University of Notre Dame, Notre Dame, IN, USA.
[9] Battlefield Environment Division, Army Research Lab, White Sands, NM, USA.

Birkhäuser

(Fitzjarrald and Lala 1989), and the Central Valley in the United States (Holets and Swanson 1981; Lee 1987; Underwood et al. 2004). In Europe, valley fog studies have been conducted in the Abisko Valley in Sweden (Adedokun and Holmgren 1993), the Po Valley in Italy (Argentini et al. 1999), and the Ebro Valley in Spain (Cuxart and Jiménez 2012). For the most part, these studies have been focused on the impacts of fog microphysics, radiative exchanges, surface energy fluxes, fog chemistry, and to minor extent mountain flow dynamics on deep (>100 m) valley fog evolution. For example, Cuxart and Jiménez (2012) analyzed a 300-m thick and 60-h long persistent fog in a wide closed valley; Holets and Swanson (1981) focused on a 6-day fog event with thicknesses between 100 and 600 m; Pilié et al. (1975) studied the life cycle of 100-m thick and 5-h long valley fog. However, less attention has been paid to shallow (<20 m) valley fog, which is extremely challenging to predict with current numerical weather prediction models (see Pu et al. 2016 submitted to PAAG to the same issue). In an attempt to fill this research gap, this work focuses on shallow and short-duration (~ 100 min) valley fog.

Under cold weather conditions, suspended fine ice crystals may form and lead to ‘ice fog’. Ice fog is hazardous, as ice crystals tend to settle on the surfaces of roads and airplanes, but also very challenging to forecast because of the knowledge gaps in its microphysical dynamics as well as limited near-surface observations (Gultepe et al. 2009, 2012). While the consensus is that ice fog forms at temperatures below −30 °C, recent studies have reported its occurrence under warmer conditions (>−20 °C, Gultepe et al. 2008) that are related to ice nucleation processes.

Numerous experimental and numerical studies have shown over the past decades that turbulence is a key variable affecting the evolution of radiation fog (Rodhe 1962; Roach 1976; Bergot and Guedalia 1994; Duynkerke 1999; Terradellas et al. 2008; Zhou and Ferrier 2008; Van Der Velde et al. 2010; Román-Cascón et al. 2012; Ye et al. 2014; Steeneveld et al. 2014). However, arguments exist regarding the role of turbulence in modulating fog evolution depending on the situation. For example, some researchers report that turbulent mixing inhibits fog formation since fog forms when the turbulence intensity is low (Roach 1976; Ye et al. 2014). Other researchers have noted that turbulent mixing actually supports fog formation by the mixing of cool near-surface air with warm near-saturated air above the boundary layer, which leads to air saturation and fog formation (Gerber 1981; Welch et al. 1986). More recently, Zhou and Ferrier (2008) introduced a turbulence intensity threshold above which radiation fog would dissipate under the action of strong turbulent mixing. Although it is difficult to pinpoint the role of turbulence on fog evolution, case studies with detailed turbulence measurements may give new insight on this matter.

Besides turbulence, internal gravity waves (IGW), commonly observed in stable stratified boundary layers (Finnigan 1988) and over mountainous terrain (Nappo 2002), are also known to impact fog dynamics. Indeed, several studies have found that gravity waves can lead to quasi-periodic oscillations in air temperature, liquid water content and visibility (Roach 1976; Gerber 1981; Choularton et al. 1981; Welch et al. 1986; Kurita et al. 1990; Duynkerke 1991; Richiardone et al. 1995; Uematsu et al. 2007; Manoj and Devara 2011; Ye et al. 2014; Price et al. 2015). For instance, Roach (1976) reports a case of radiation fog with quasi-periodic oscillations in surface temperature, wind speed and net infrared radiative flux with time periods of 10–15 min. He concludes that the interaction between turbulent mixing and radiative cooling is the driving factor for radiation fog formation based on the phase difference between these variables. Duynkerke (1991) also found that gravity waves can introduce oscillations in fog thickness and visibility for a shallow (≈ 30 m) radiation fog. However, the understanding of the interactions between the internal gravity waves and fog processes is still partial (Haeffelin et al. 2010). Overall, far too few studies have provided quantitative analyses of IWG interactions with shallow valley/radiation fogs.

This paper presents a case study of a shallow, short-duration, early morning valley (ice) fog event formed in a stable boundary layer affected by its interactions with atmospheric waves and turbulence. The case study event is typical of wintertime fogs observed within valley bottoms of northern Utah

(Horel et al. 2002). The objectives of this paper are to use a case study of a typical shallow fog event in an enclosed mountain valley: (1) to classify the fog type and describe the fog event in terms of its key mean and turbulence variables; (2) to investigate the impacts of mountain flow dynamics on fog physical behavior; (3) to understand the linkage between internal gravity waves and quasi-periodic oscillations in visibility in shallow fog layers. This observational work was conducted as part of the Mountain Terrain Atmospheric Modeling and Observations (MATERHORN) program. One of the primary objectives of the program was to better understand atmospheric fluid dynamics across all scales over realistic mountainous terrain as well as under transient and steady conditions. MATERHORN-Fog is a field campaign designed to study the formation of fog in complex terrain. More details on the MATERHORN program can be found in Fernando et al. (2015), while an overview of the MATERHORN-Fog field campaign is provided in Gultepe et al. (2016) (submitted to PAAG for this same issue).

2. Methods

2.1. Experimental Site

Observations were conducted on a dairy farm in Heber Valley, Utah (40°31′40″N, 111°27′36″W, Fig. 1), a sheltered alpine valley with mixed agricultural and urban land cover, located ≈50 km southeast of Salt Lake City. The Wasatch Mountains and the Rhodes Plateau define the western and eastern borders of the valley, respectively. Thom (1965) describes the valley as roughly circular with an approximate diameter of 16 km, surrounded by several escarpment and canyons (see Fig. 1b). The Provo River runs on the valley floor, from the Jordanelle reservoir at the north end of the valley to the Deer Creek reservoir at the southeastern end at an elevation of 1652 m above sea level (asl). The highest peaks surrounding the valley are ∼3500 m asl and are located to the west and southwest.

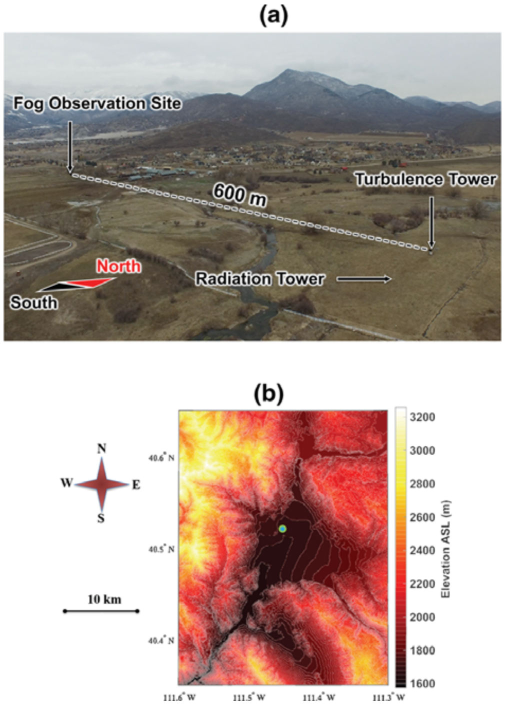

Figure 1

a Aerial photograph capturing the Heber Valley site facing northwest, taken on February 27, 2015. The locations of the main sampling sites have been highlighted. Note that during the case study (January 9, 2015) snow cover was present. Photo courtesy of Derek Jensen and Tim Price. **b** Topographic map of the Heber Valley. The contour interval is 25 m. The *blue* point with *green* outline represents the main study area

The main campaign operations were conducted between January 7 and February 1, 2015, the time when fog events are most likely to occur in northern Utah (Hodges and Pu 2015). Snow covered the valley floor for the duration of the experiment, although substantial melt occurred near the end of the campaign. The snow layer is a moisture source and acts as an isolating layer between the soil and air, thus limiting heat and mass transfer between the soil and the atmosphere. Both the enhanced moisture availability and the reduced heat transfer from the warmer ground are expected to promote fog formation (Lareau et al. 2013). A detailed overview of the campaign can be found in Gultepe et al. (2016) (submitted to PAAG for this same issue). As shown in Fig. 1a, there were two closely situated (600 m) observational sites: one dedicated to detailed fog observation (1708 m asl) and another focused on energy balance and turbulence measurements (1696 m asl). The lower altitude site included a 28-m turbulence tower, an adjacent radiation flux divergence measurement tower (50 m south of the turbulence tower), and ground heat flux measurements (100 m south of the turbulence tower). Due to the strong spatiotemporal variability of fog in this case study, small-scale flow dynamics which can trigger or inhibit fog formation (as will be discussed), are slightly different between the two sites.

2.2. Instrumentation

At the fog observation site, a suite of instruments was deployed to characterize fog properties, which are discussed in detail in Gultepe et al. (2016) (submitted to PAAG for this same issue). Briefly, the instrumentation included: (1) one Vaisala PWD22 present weather detector measuring visibility (uncertainty of ±10 %), installed at 3.1 m above ground; (2) one HMP155A temperature/relative humidity sensor (Campbell Sci. Inc.) installed at 1.0 m above ground with 1 Hz sampling rate and uncertainties of ±1.8 % in relative humidity and ±0.25 °C in temperature; (3) two Young ultrasonic anemometers (R. M. Young Company) at 1.0 and 2.8 m above ground with 20 Hz sampling rate, whose uncertainties are ±0.05 m s^{-1} in velocity components and ±2 °C in sonic temperatures; (4) one Met One Instruments Inc. eight-channel particle counter (Model 212-2) with an uncertainty of ±10 % at 3.85 m with 1 Hz sampling rate; (5) two HDCAM (Micro-7) cameras pointing two directions (125° and 155° from north) at 1.6 m with one frame per min sampling rate. Fog particle spectra measurements from a fog measuring device (FMD) were not available during this case study.

The turbulence tower consisted of a 28-m mast equipped with sonic anemometers and fine-wire type K thermocouples (75 μm diameter, uncertainty of ±0.07 °C, Omega Engineering, Inc.) at five levels (2.10, 3.99, 7.80, 14.55, 27.30 m) sampled at 20 Hz. A CSAT3 sonic anemometer was deployed at the 7.80 m level with uncertainties of ±0.08 m s^{-1} in horizontal velocity components and ±0.04 m s^{-1} in vertical velocity components, while RM Young ultrasonic anemometers where deployed at all other levels. In the following figures and discussions, we will use 2, 4, 8, 15, and 27 m to refer to these heights for the sake of clarity. In addition, we also installed HMP45C temperature and relative humidity sensors at ten levels (0.94, 1.94, 2.62, 3.80, 5.89, 7.67, 10.05, 11.86, 14.27 and 27.1 m) with 1 Hz sampling rate. One EC150 CO_2/H_2O open path gas analyzer (Campbell Sci., Inc.) was deployed at 7.80 m above ground level (agl) along with a PTB 110 barometer (Vaisala, Inc.), with an accuracy of ±0.3 hPa. Both sampled at 20 Hz. Finally, a LI-7500A CO_2/H_2O open path gas analyzer (LiCOR, Inc.) was deployed at 2.10 m with a sampling rate of 20 Hz. The tower recorded data from January 1 to March 30, 2015. The individual shortwave and longwave components of the radiation balance were measured at frequency of 1/6 Hz with up- and down-facing pyranometers and pyrgeometers (CMP21 with directional error less than 10 W m^{-2} and CGR4 with offset less than 4 W m^{-2}, Kipp & Zonen) mounted horizontally at ~2 and 8 m above ground on a 10-m radiation tower located south of the main tower (Fig. 1a).

A 9 m^3 DigiCORA tethered balloon system (Vaisala, Inc.) was deployed to characterize the shallow fog layer vertical structure during Intensive Observation Periods (IOPs). The launching point was about 50 m south of the fog observation site. During nights without fog formation, profiles were obtained up to 100-m. Each profile vertical leg of a profile took ~3–5 min, the balloon was then positioned at the top of its path for 30 min before descending back to the surface. During fog events, the tethered balloon profiled continuously. A single Vaisala TS111 tethersonde fixed to the tether line approximately 5 m below the balloon measured temperature, relative humidity, pressure, wind speed and wind direction with uncertainties of 0.5 °C, 5 %, 1.5 hPa, 0.5 m s^{-1}, respectively. Data were collected at a sampling frequency of 1 Hz. In addition to tethered balloon soundings, untethered Radiosondes (DFM-09, GRAW Radiosondes) were launched every 3 h during IOPs, recording the temperature (error <0.2 °C), humidity (error <5 %), and wind (error <0.2 m s^{-1}) profile up to about 10 km agl.

To study the spatiotemporal variations of surface variables, six automatic weather stations were deployed in the Heber Valley during the field campaign. Temperature, humidity, winds and pressure were measured at each station with the sampling frequencies of 0.2, 0.2, 1, 1 Hz, respectively. More details can be found in Bossche and de Wekker (2016) (submitted to PAAG for this same issue).

2.3. Data Processing

Turbulence data analysis used the Utah Turbulence in Environmental Studies Processes and analysis code (UTESpac, see Jensen et al. 2015). More details on the turbulence flux corrections and quality control can be found in Jensen et al. (2015). Most of the meteorological data have been averaged over 5-min periods to remove noise, as well as to capture the rapid fog dynamics and turbulent processes. Visibility data from the PWD22 present weather detector were averaged over 10-min. Particle concentrations, surface radiative fluxes, and the data from automatic weather stations have been averaged over 1-min periods to capture small-scale dynamics.

Wavelet analysis was used to study the internal gravity waves. It is a common and powerful multiscale tool often used for determining the dominant modes of variability in environmental time series without suffering from the limitations of the (more traditional) windowed Fourier transform (Torrence and Compo 1998). Wavelet transforms have been applied in the past to analyze turbulence and wave structures in atmospheric flows (Rees et al. 2001; Viana et al. 2009; Román-Cascón et al. 2015a, 2015b). In this study, we use this method to identify the signature of atmospheric waves throughout the fog event. The Morlet wavelet, which is a nonorthogonal and complex wavelet basis function with a plane wave modulated Gaussian function, is adopted in this work. A detailed description of this method can be found in Torrence and Compo (1998) and Gultepe et al. (2000).

2.4. Satellite-Based Fog Retrievals

To detect fog for the period of interest over the United States Great Basin region, imagery data from the Geostationary Operational Environmental Satellite (GOES)-15 infrared (IR) channels were combined. GOES-15 imager datasets were obtained from the Comprehensive Large Array-data Stewardship System (CLASS, available online at http://www.class.ncdc.noaa.gov/) and a fog product image was generated by the Man computer Interactive Data Access System (McIDAS)-X program that performs a differencing operation in which shortwave infrared (SWIR) radiance (channel 2, 3.9 μm wavelength) brightness temperature is subtracted from the infrared radiance (IR) (channel 4, 10.7 μm) brightness temperature. The resulting quantity of this operation is referred to as the brightness temperature difference (BTD, see Ellrod and Gultepe 2007) with a horizontal resolution of 4 km. Note that the effect of shortwave radiance on SWIR black body temperature was not included in the analysis, which might result in an overestimation of SWIR temperature. In addition, retrievals cannot easily distinguish clouds that may result in low ceilings and/or reduced surface visibility from higher-based stratus, stratocumulus, and altostratus. Manual observations on January 9, 2015 indicated that there were few higher-based stratus clouds during most of the study period, however, some cirrus clouds were observed during the period. The McIDAS fog detection program generates output files in both AREA and netCDF format.

3. Results and Discussion

3.1. Overview of the Fog Event

This paper presents a case study of a single fog event that occurred on January 9, 2015, from 0720 to 0900 MST (Fig. 2a). This analysis focuses on a patchy, shallow and relatively short-duration fog episode that is typical of what is regularly observed in the Heber Valley during winter. During the 1-month field campaign, fog events were reported on eight different days. All events were short-duration and shallow fogs similar the one analyzed in this study, except the event on January 16, 2015, which was a dense and deep ice fog (Gultepe et al. 2016 submitted to PAAG for the same issue).

3.1.1 Synoptic Conditions

On January 9, 2015, a long wave ridge spanning from Oregon to Texas at 500 hPa provided warm air

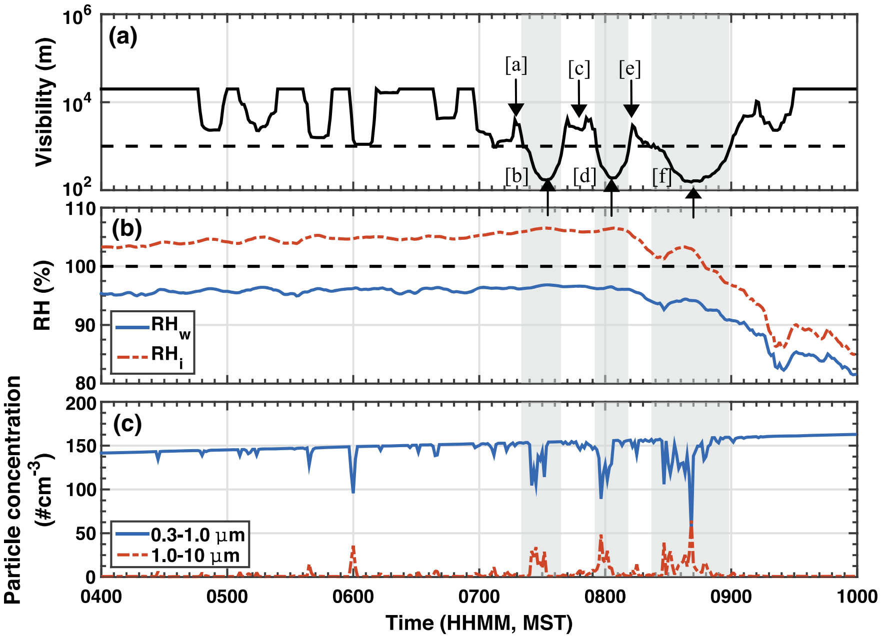

Figure 2

Time series of relevant variables at the fog observation site on January 9, 2015. **a** Visibility obtained from the PWD22 present weather sensor. The *black dashed line* represents a visibility of 1000 m. *Letters* (*a–f*) in the figure indicate the timestamps of photographs from the fog observation site presented in the *left column* of Fig. 3. *Shaded areas* represent the periods when the visibility is less than 1000 m. **b** RH$_w$ and RH$_i$ are relative humidity with respect to water and ice, respectively, at the same location. **c** Particle concentrations

advection into northern Utah at upper levels. Clear skies and calm winds were observed at 0800 MST based on Weather Prediction Center (WPC) surface analysis from NOAA (http://www.wpc.ncep.noaa.gov/). More details on the synoptic conditions can be found in Pu et al. (2016) (submitted to PAAG for this same issue).

The 0813 MST radiosonde profiles (Fig. 3) show a 100-m deep cold-air pool layer characterized by near-saturated relative humidity and calm winds (<0.5 m s^{-1}). The cold-air pool is capped by a strong temperature inversion, with a vertical gradient of 11.3 °C km^{-1} between 100 and 500 m agl. RH drops rapidly from 95 to 65 % between 100 and 500 m, and wind speed reaches a local maximum of 5 m s^{-1} at about 300 m agl. Between 500 and 1100 m, there is a weaklier stable layer with little change in RH and winds. Immediately above the average ridge-top level to 1200 m agl, a strong 150 m temperature inversion layer is observed. In this layer, RH decreased dramatically from 50 to 25 %, and wind speed remained 1 m s^{-1} in this layer. This 100 m-depth layer disconnects the flows above and below the ridge top. Above this layer, dry adiabatic flow can be observed above 1200 m. RH remains relatively dry at 25 %, and wind speed starts to increase to almost 10 m s^{-1}, which is influenced by the synoptic forces.

3.1.2 *Visibility, Relative Humidity, and Particle Concentration*

Here, we define fog as when visibility drops below 1000 m, as recommended by NOAA (2005). During the event, fog formed in a cyclic pattern, as indicated by the three clear oscillations in visibility in Fig. 2a. Based on an inspection of time lapse photographs, the average depth of the fog layer was estimated to be about 30 m at the turbulence tower and about 5–15 m at the fog observation site (12 m higher up the slope), indicating a near-horizontal average fog top height.

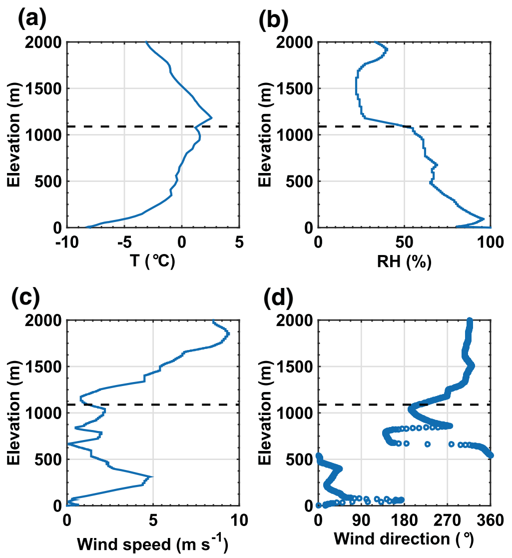

Figure 3
Observations from a radiosonde launched at 0813 MST: **a** air temperature; **b** relative humidity; **c** wind speed; **d** wind direction. The *black dashed line* represents the average ridge-top level (1100 m agl) surrounding the Heber Valley basin

Relative humidity with respect to ice ($\mathrm{RH_i}$) is used in this work to study the potential of ice fog occurrence (Gultepe et al. 2003). When $\mathrm{RH_i} > 100$ %, it indicates that ice fog can be formed. In this study, we follow Eq (1) to (4) of Gultepe et al. (2014) to calculate $\mathrm{RH_i}$. From Fig. 2b, we can see that relative humidity with respect to water vapor ($\mathrm{RH_w}$) was constantly greater than 95 % from 0400 to 0810 MST, which indicates that the air was saturated if we consider the uncertainty of relative humidity sensors ($\sim$5 % for RH from 90 to 100 % at -10 °C from personal communication with Dr. Sasha Ivans from Campbell Sci. Inc.). Meanwhile, $\mathrm{RH_i}$ was greater than 100 % before and during the fog event. This is a necessary but not sufficient condition for the formation of ice fog—for instance, sufficient ice condensation nuclei also have to be present. When ice fog occurs, the ice crystals have typical sizes between 10 and 200 μm with fall speeds similar to 10 μm droplets (Gultepe et al. 2014). Unfortunately, these variables were not measured during this event because of instrumental issues. Nonetheless, it is worth noting that during the experimental period, deposited ice crystals were observed on the tethersonde balloon and other surfaces, which could indicate deposition of ice fog. Both $\mathrm{RH_w}$ and $\mathrm{RH_i}$ started to decrease after 0810 MST with increasing temperature.

To better understand the nature of fog particles, we present the evolution of the particle size distribution. For clarity, seven size bins are aggregated into two intervals: small particles, which are the cloud condensation nuclei (particles with diameters of 0.3–1.0 μm), and larger particles, which are the fog droplets with diameters of 1.0–10.0 μm. Figure 2c shows a very clear anti-correlation between cloud condensation nuclei particles and fog particles. In essence, during the fog episodes, water vapor condenses on the cloud condensation nuclei and quickly grows to form the fog droplets. This result is consistent with the observations that have been reported in the literature (Ahrens 2012).

3.1.3 Net Radiation

Some of the most essential variables in studying radiation fog are the surface radiative fluxes, which not only directly influence the temperature structure and droplet growth (Mason 1982; Gultepe et al. 2016 submitted to PAAG for this same issue), but also indirectly affect energy transfer by initializing the vertical heat flux. Figure 4a shows that the net radiation remains constant at about $-45\ \mathrm{Wm^{-2}}$ during the nighttime period, and only small changes are seen during the shallow fog event. This constant surface radiative cooling is the most frequent cause of the development of a nocturnal stable boundary layer under clear-sky conditions (Mahrt 2013). Meanwhile, it also promotes fog formation by decreasing air temperatures close to the ground. A detailed look at the incoming longwave radiative fluxes (Fig. 4b) shows an increase as fog particles (water droplets and/or ice crystals) are introduced in the near-surface air layer. The small variations in longwave incoming radiation correspond well with the changes in fog density and visibility seen in Fig. 5. In Heber Valley, astronomical sunrise on January 9, 2015 occurred at 0748 MST. Net radiation became positive at 0835 MST, leading to increasing temperatures, decreasing RH, and finally to fog dissipation at 0900 MST (Fig. 2a).

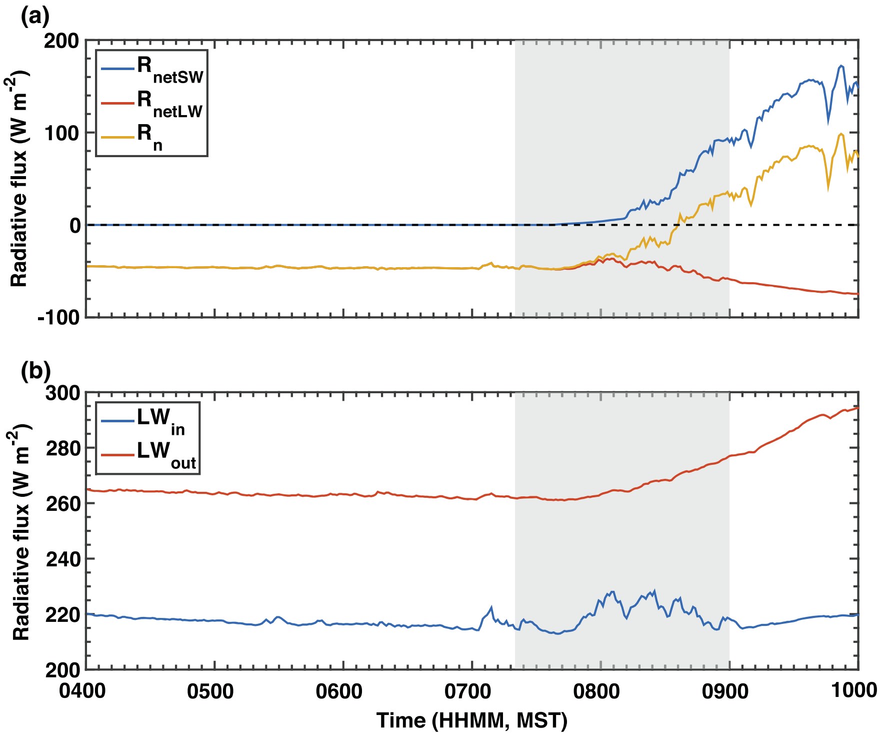

Figure 4

Time series at 2 m agl of **a** net shortwave radiation (R_{netSW}), net longwave radiation (R_{netLW}) and net radiation (R_n); **b** incoming (LW_{in}) and outgoing (LW_{out}) longwave radiation. The *shaded area* represents the fog event at the turbulence tower site. The astronomical sunrise time is 0748 MST

3.1.4 Photographs and Satellite Imagery

The oscillations in visibility reported in Fig. 2a were observed at both sites in photographs taken during the period 0720–0900 MST (Fig. 5). Although the local fog behavior at both sites is correlated, there are differences in the timing and amplitude of oscillations. This is a result of the spatial separation and terrain differences at the two sites. In addition to variations in fog densities occurring over short distances (≈600 m), spatial variability was substantial over larger scales during valley fog events. Figure 6 illustrates this larger scale variability using satellite imagery of brightness temperature difference (BTD) in the region of interest. The satellite retrievals demonstrate that Heber Valley was occupied by several patches of shallow fog (indicated by BTD >1.0 K), and that this spatial pattern was also observed in other mountain valleys of the area. In addition, fog became thicker and higher after 0800 MST. This is the result of the convective mixing generated by both surface heating and radiative cooling at the fog top.

Figure 5 ▶

Photographs taken during the fog event on January 9, 2015. The *left column* shows images collected at the fog observation, with the field of view pointing northwest, while the *right column* shows images from the turbulence tower site, with the field of view pointing north. **a** Fog starts forming in the background; **b** fog reaches the sites; **c** fog leaves the site/dissipates for the first time; **d** fog reaches the site for the second time; **e** fog leaves the site/dissipate for the second time; **f** fog comes back at its thickest. Both sites have similar fog oscillations. However, the initialization and dissipation of each oscillation are slightly different between the two sites due to the fact that they are separated horizontally by 600 m and vertically by 15 m


0708 MST
(a)
0718 MST
0730 MST
(b)
0726 MST
0747 MST
(c)
0733 MST
0800 MST
(d)
0801 MST
0813 MST
(e)
0809 MST
0840 MST
(f)
0821 MST

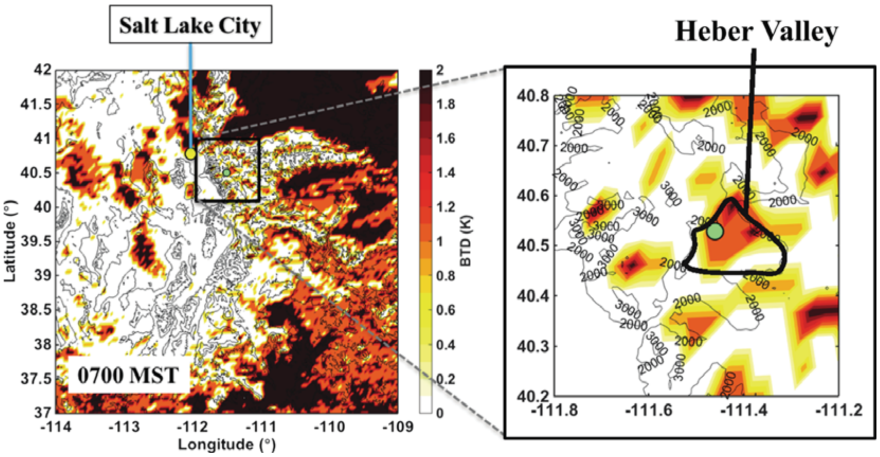

Figure 6

Satellite imagery at 0700 MST from GOES-15 on January 9, 2015. When the brightness temperature difference (BTD) >1 K, it indicates fog. BTD here is calculated by T_4–T_2, where T_2 is the GOES-15 SWIR band at 3.9 μm wavelength and T_4 is the GOES-15 LWIR band at 10.7 μm. The *green circle* indicates the location of the fog observation site in the Heber Valley. Elevation contours are displayed in *black* in the background. *Black bold line* roughly represents the Heber Valley

3.2. Flow Dynamics and Impact on Fog Evolution

Accurate prediction of valley fog formation requires a sufficient understanding of the nocturnal boundary layer. In this section, we examine the impacts of nighttime flow dynamics over mountainous terrain on fog evolution.

3.2.1 Temperature Profiles

Temperature is considered the main factor that has direct influence on fog by controlling the growth of water droplets. Figure 7a shows a contour plot of air temperatures (2.1–27.3 m) from the turbulence tower. Four fine-wire temperature sensors are used to show the vertical structure of air temperature. Before the fog event (0400–0700 MST), near-surface air temperatures decreased steadily with a cooling rate of 0.5 °C h^{-1} due to radiative losses. Meanwhile, Fig. 7b shows the surface inversion with a vertical temperature gradient of ~0.1–0.2 °C m^{-1} before and throughout the fog event (0500, 0700, 0740 MST in the figure). After 0835 MST, when net radiation changed sign (see Fig. 4a), near-surface temperatures increased rapidly, and a convective near-surface layer developed. The rapid warming was not only confined to the near-surface layers, but to the stably stratified layer above too, due to absorption of shortwave radiation by the fog particles. Some 30 min later (0900 MST), a near-neutral stratification had developed and the fog had fully disappeared.

In addition, we observed rapid temperature drops at a rate of ≈0.1 °C min^{-1} at 0500, 0535, and 0650 MST within the bottom 10-m atmospheric layer. These are caused by cold-air advection from nearby mountain circulations, possibly inducing sloshing of cold pool air, as will be discussed in Sect. 3.2.2.

3.2.2 Mean Wind, Drainage Flows, and Cold-Air Advection

Cold-air pools are often observed in the mountainous valleys due to topographic depressions with cold air cooled by near-surface longwave radiation loss, which leads to air stagnation (calm winds) and strongly stratified layers (Lareau et al. 2013, temperature inversions) that inhibit transport (Whiteman et al. 2001; Lareau et al. 2013). In this study case, a cold-air pool with a depth of 50–100 m was observed throughout the night. The measurements display extremely low wind speeds before and during the fog episode with an average value of 0.43 m s^{-1} in the lowest 27 m agl. Figure 8 shows tethered balloon

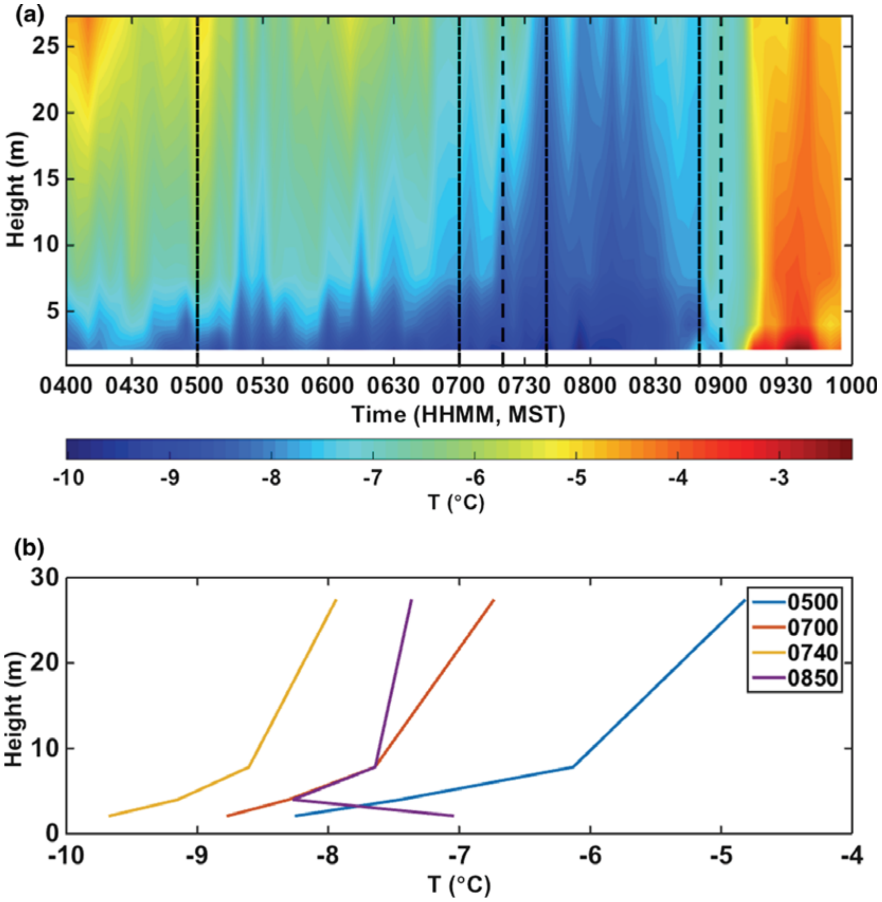

Figure 7

a Contour plot of air temperatures at the turbulence tower site. Four levels (2.1, 4.0, 7.8, 27.3 m) of fine-wire thermocouples were utilized to generate this plot. The *black vertical dashed lines* represent the start and end of the fog event. *Black dash-dot lines* represent the profiles showing in (**b**); **b** Temperature profiles from the same measurements at four different stages (i.e., 0500 MST: 2-h before fog formation; 0700 MST: right before fog formation; 0740 MST: early stage of fog event; 0850 MST: late stag of fog event). Legend is in MST

profiles 2 h before (0510 MST), right before (0709), during (0741 MST), and after (0924 MST) the fog event. The potential temperature profile was stably stratified at 0709 MST with the coldest potential temperatures in the bottom 40 m and a vertical gradient of 0.13 °C m^{-1}. At 0510, 0741, and 0925 MST, the cold-air pool had similar behavior, but with weaker inversion strength. From Fig. 8b, we can see that the wind speeds were lower than ≈ 1 m s^{-1} inside the cold-air pool during the period of interest, which is consistent with the radiosonde profile (Fig. 3).

Figure 9 shows a time series of wind speed (Fig. 9a) and wind direction (Fig. 9b) for a 27-m layer above the surface. Winds greater than 0.5 m s^{-1} tend to show consistent wind directions across certain heights. For instance, winds uniformly came from N ($\approx 10°$) at 0420; from NE ($\approx 45°$) at 0530; from W ($\approx 270°$) at 0550; from S ($\approx 180°$) at 0700 MST. The data indicate that this is a signature of drainage flows coming from the mountain slopes surrounding the field site or cold-air pool sloshing.

A sudden spike in turbulent kinetic energy (TKE $= \frac{1}{2}\left(\overline{u'^2} + \overline{v'^2} + \overline{w'^2}\right)$, where u', v', and w' are

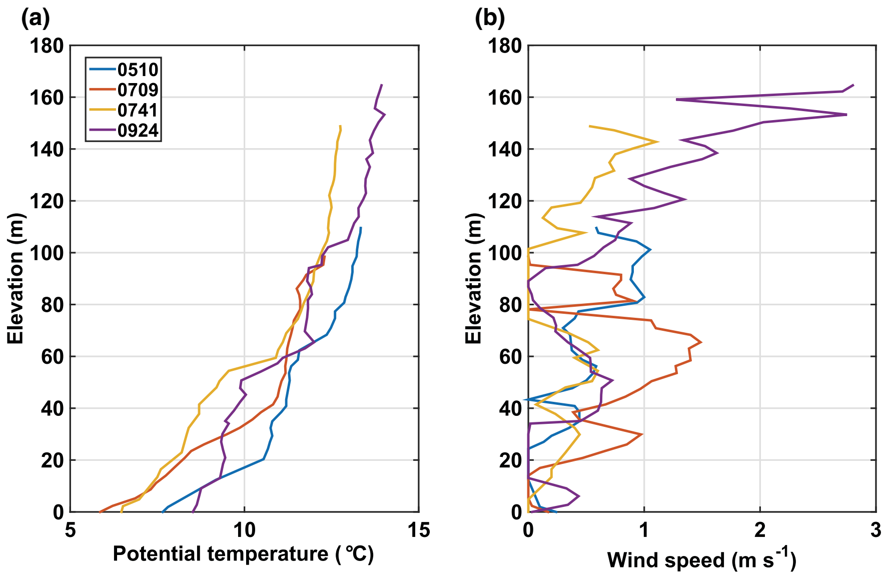

Figure 8

a Potential temperature and **b** wind speed profiles from tethered balloon data launched during four different time periods. Time is in MST

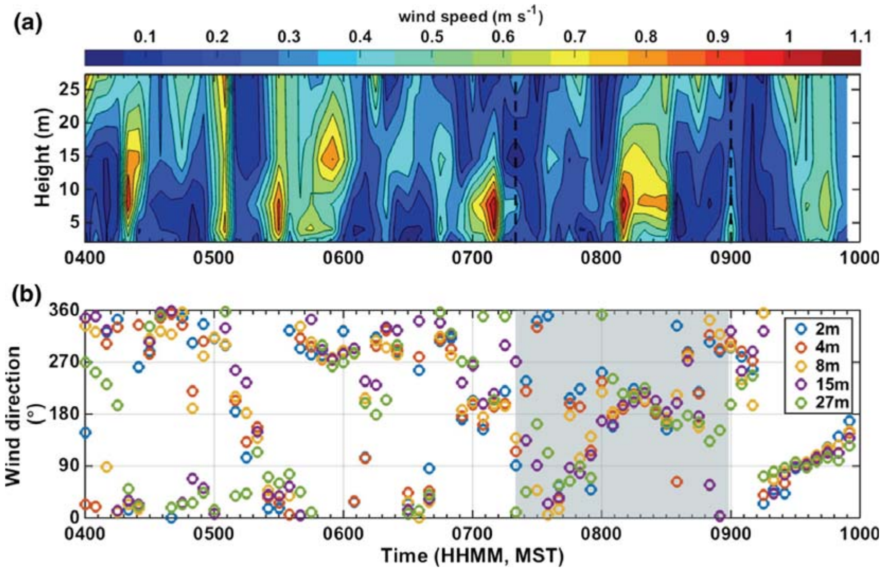

Figure 9

a Contour plot of wind speed and **b** time series of wind direction at five different levels of the turbulence tower. *Shaded area* represents the fog event

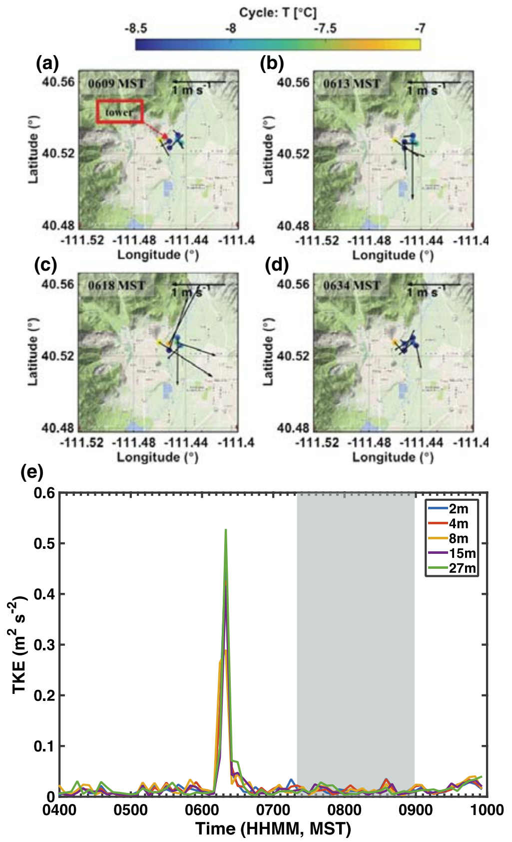

Figure 10

a–**d** Wind vectors and temperature from five automatic weather stations and the turbulence tower (indicated in **a** by *red arrow*) at four different times; **e** Turbulent kinetic energy (TKE) at five levels. TKE data have been averaged over 5-min intervals to resolve the rapid change by oscillations. *Shaded area* represents the fog event

the along-wind, crosswind, and vertical velocity perturbations from the 5-min block mean) started at 0610 MST, peaked at 0620 MST, and stopped at about 0635 MST (Fig. 10e). The TKE spike was dominated by along-wind velocity fluctuations (i.e., u', not shown). We hypothesize that this rapid increase in TKE is caused by the collision of drainage flows and sloshing of the cold-air pool. Figure 10a–d shows wind vectors and temperatures from five automatic weather stations and the turbulence tower at 0609, 0613, 0618, and 0634 MST. At 0609 MST, calm winds were observed at all stations. As indicated in Fig. 10a, temperatures were stratified in the lowest 28 m. Figure 10b clearly shows that winds were coming from three different directions (i.e., N, NW, and E). Slightly stronger winds from north to northwest were caused by drainage flows from the two canyons on the NW and NE sides of the turbulence tower site (see Fig. 1b). The weak easterly flow was caused by the sloshing of the cold-air pool. Consequently, these three flows met at the bottom of the valley (i.e., near the turbulence tower site) and initialized the collision. At 0618 MST, when TKE reached its peak, the flows were significantly affected by the strong local shear instability generated by the collision, which led to a clockwise eddy with a scale of several kilometers in the valley (Fig. 10c). Finally, after dissipation of the TKE spike, calm winds were observed at 0634 MST (Fig. 10d). We speculate that the collision of these drainage flows and the cold-air pool sloshing on the valley floor produced a horizontal (not aligned with gravity) shear instability resulting in turbulence and exciting gravity waves to due vertical displacement of streamlines (see e.g., Sun et al. 2015). The collision is accompanied by a coherent change in the sign of the sensible heat flux (see Fig. 13). Prior to the peak in TKE the heat flux is negative; at the peak the flux is positive, and then following the peak the flux is negative again.

Alternatively, the spike in TKE could have been produced through vertical shear instability (e.g., Kelvin–Helmholtz instability) at the interface between the cold-air pool and the flow above (e.g., Monti et al. 2002). However, given the nearly calm conditions (bulk Richardson number is constantly greater than 100 during the night) through the lowest 100 m of the cold pool, we expect that this is less likely.

If turbulent mixing of air masses can trigger fog formation, cold-air advection by drainage flows appears to have the same effect. We see that fog forms at 0720 MST right after a short pulse of cold air (bottom 10 m on Fig. 9a) from the south reaches the site, which decreased the air temperature at lower levels (see Figs. 7a, 11).

As a complementary approach to better understand the effect of drainage flows and cold-air advection (via cold pool sloshing), we present 5-min averaged time series of air temperatures at four levels (2, 4, 8 and 27 m) from 0400 to 1000 MST

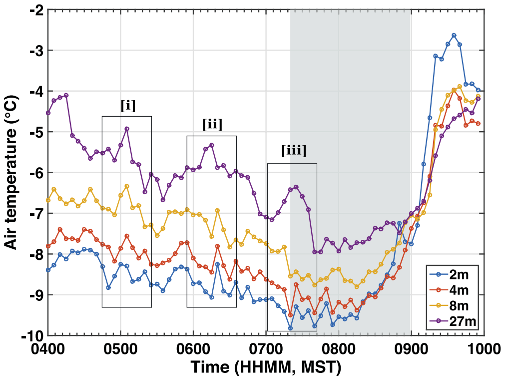

Figure 11
Air temperature at four different heights measured by thermocouples at the turbulence tower site. The data have been averaged over 5-min intervals to resolve the rapid change by oscillations. The *shaded area* represents the fog event. Three *rectangular boxes* (*i, ii, iii*) represent three oscillation

(Fig. 11), and focus on three major oscillations (box [i], [ii], and [iii]). Box [i] shows that the oscillation at all levels displays similar phases and amplitudes with fluctuations in temperatures of ≈0.6–0.8 °C. These amplitudes are similar to those previously reported in other studies from the action of internal gravity waves (e.g., ≈1 °C in Duynkerke 1991). Temperatures decreased at 0455 MST and immediately increased. Wind data indicate that there was a northwesterly drainage flow (Fig. 9) which advected cold air to the turbulence tower site. Meanwhile, the original air mass was lifted. After the drainage flow passed the site, the (relatively) warm air aloft descended to the surface. The whole process caused the temperature oscillation shown in box [i]. The temperatures in box [ii] correspond to the TKE spike described above. Strong temperature fluctuations are evident at all levels. However, the temperature trend at 27 m was opposite the trend at the lower three levels. This can be explained by two simultaneous mechanisms. For the first mechanism, the air mass near the surface was vertically displaced by a relatively colder drainage flow coming from north (Fig. 10b). During this process the temperature at the lower three levels decreased. The vertically lifted air mass then returned to its equilibrium position and the temperatures near the surface rose in response. For the second mechanism, the upper level (27 m) was influenced by the horizontal warm air advection caused by the collision. Moreover, the temperature oscillations within the bottom 8-m continued until 0650 MST, which was a result of the internal gravity wave generated by vertical displacement. However, the oscillation at 27 m was damped right after the peak temperature (at 0615 MST). In box [iii], the temperature decreased at lower layers (i.e., 2, 4, and 8 m) and increases at upper layer (i.e., 27 m), which is similar to what was observed in box [ii]. Recall that there was southerly cold-air advection at 0700 MST. The depth of this layer was about 10 m (based on Figs. 7a, 9a). The temperature rise at 27 m was probably caused by the warm-air advection coming from west.

3.2.3 *Internal Gravity Waves*

Drainage flows not only bring cold air into the valleys, but also can trigger internal gravity waves (Porch et al. 1991; Viana et al. 2010; Udina et al. 2013) under stable conditions. During the study periods, several oscillations in visibility, wind speed and TKE with time periods of about 10–20 min are reported in Figs. 2a, 9a, 10e. We believe that they are all connected to internal gravity waves (IGW). In this section, we discuss the presence of IGW in more details along with its impact on fog evolution.

To show the basic characteristics of IGW in this case, Fig. 12a presents filtered surface pressure (dP) using a high-pass Butterworth filter (removing periods larger than 45 min) at 8 m agl. Clear oscillations can be observed during this time period with an amplitude of about 0.05 hPa, similar in magnitude to pressure oscillations observed in other studies such as the Boundary Layer Late Afternoon and Sunset Turbulence (BLLAST) field campaign (Román-Cascón et al. 2015a). Figure 12b shows the strongest energy signal for periods of 10–20 min from 0400 to 0600 MST and from 0630 to 0700 MST, which are indicative of IGW. Additional evidence of the presence of IGW are peaks in the power spectra of temperature and vertical velocity fluctuations at frequencies of $10^{-3} - 4 \times 10^{-3}$ Hz, corresponding to time periods of 4–16 min (Fig. 12c–d, see also Meillier et al. 2008).

One significant feature of IGW is its impact on vertical heat transport. To study this, we show a

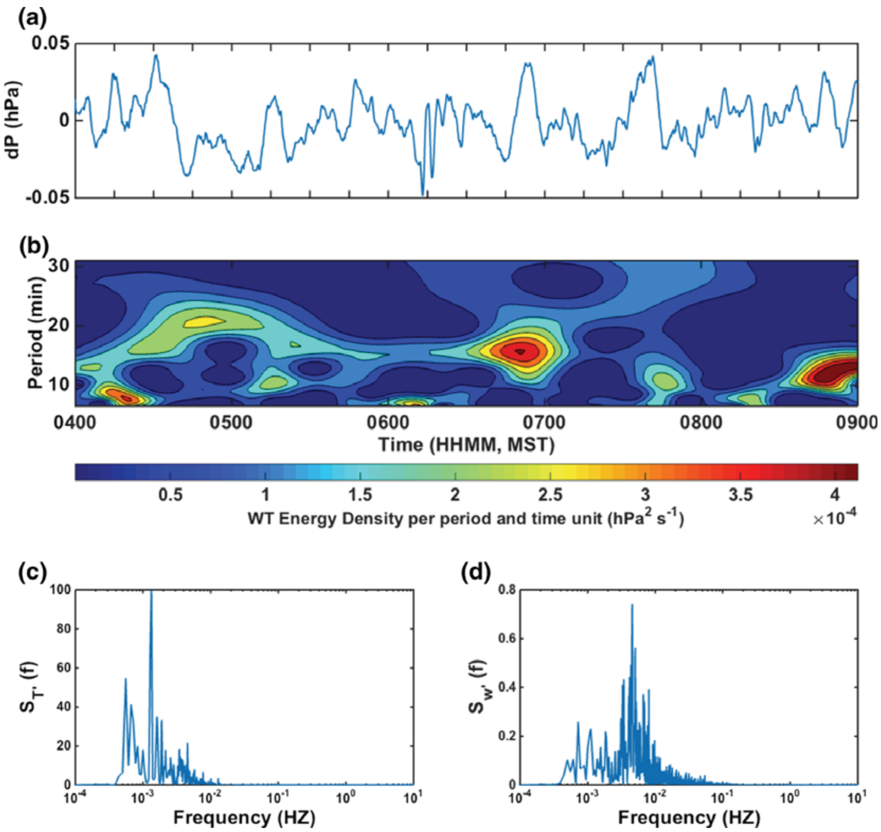

Figure 12

a Filtered surface pressure (dP) from 0400 to 0900 MST; **b** wavelet transform analysis of dP from 0400 to 0900 MST; **c**, **d** power spectra of temperature fluctuation (T') and vertical velocity fluctuation (w') from 0400 to 0900 MST

contour plot of $\overline{w'\theta'}$ interpolated from four vertical measurement levels (Fig. 13). A positive–negative oscillation of the kinematic heat flux is clearly noted, in particular during the TKE spike (from 0610 to 0635 MST). Evidence of oscillations in the kinematic heat flux was observed at 0430, 0620 and 0745 MST. Besides the one at 0620 MST, the other two were dominated by higher level (above 30 m) flow processes. We hypothesize that these oscillations were due to the existence of internal gravity waves generated by mountains.

To better understand the impact of IGW on the fog process, air temperatures at the fog observation site are presented in Fig. 14. During the foggy period (0720–0900 MST), temperature oscillations were well aligned with visibility oscillations. As discussed earlier, temperature oscillations are directly influenced by internal gravity waves due to the vertical displacements of air masses. In conclusion, good correlations between temperature and visibility indicate that the internal gravity waves have a significant impact on fog processes by modulating the near-surface air temperature in our study case.

4. *Summary and Discussion*

Figure 15 shows a conceptual figure of the flow dynamics in the valley and its impact on fog

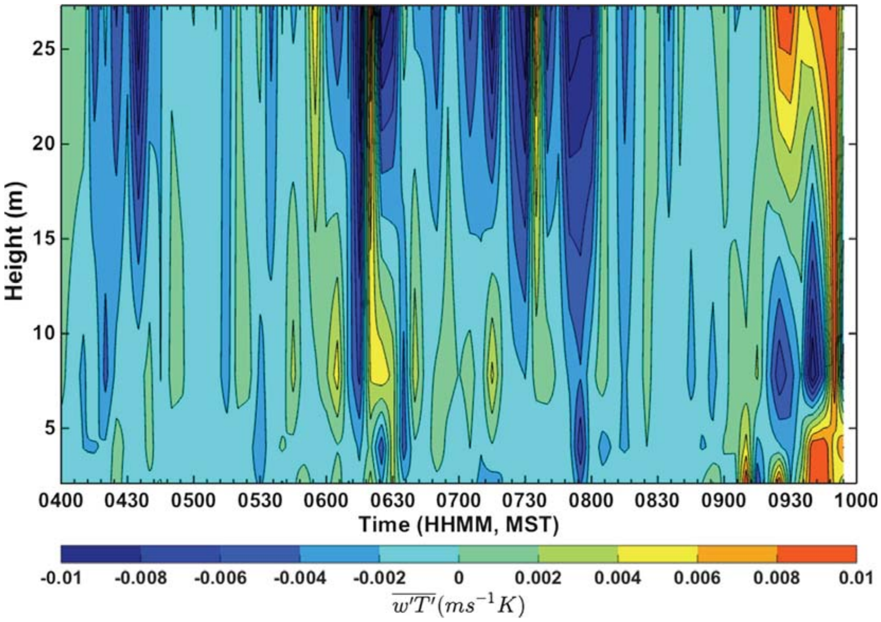

Figure 13
Contour plot of vertical heat flux at turbulence tower site. Data was averaged over 5 min

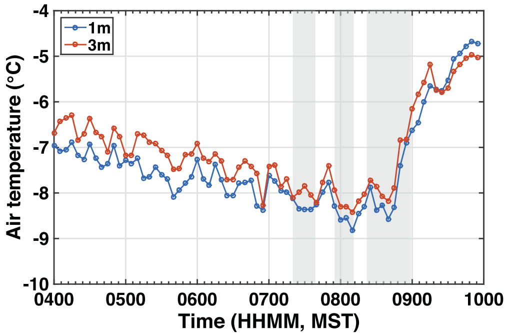

Figure 14
Air temperatures at the fog observation site at two levels. *Shaded areas* represent the periods when the visibility is less than 1000 m (i.e., fog)

evolution. The sequence of events occurring during the January 9 fog event may be summarized as follows:

- 0440–0510 MST: internal gravity waves were observed in the valley, possibly generated by the surrounding topography and vertical displacements caused by downslope drainage flow interactions. Indeed, a noticeable energy peak with a 20-min period can be observed from wavelet analysis based on dP (Fig. 11a).
- 0530 MST: a drainage flow comes from the north (~20°).
- 0550 MST: another drainage flow comes from the west (~270°).
- 0600 MST: a collision between drainage flows and cold-air pool sloshing causes strong local shear instability, which leads to a sudden increase in TKE at 0620 MST.
- 0700 MST: southerly advection brings a cooler air mass to the measurement site, which triggers fog formation by lowering the temperature rapidly.
- 0720 MST: fog forms at both the fog observation site and turbulence tower site.
- 0720–0900 MST: fog (visibility) oscillates due to the impact of IGW on temperature and surface pressure (Fig. 14). At about 0800 MST, the air temperature starts to increase via solar insolation. A convective mixing layer was built by both

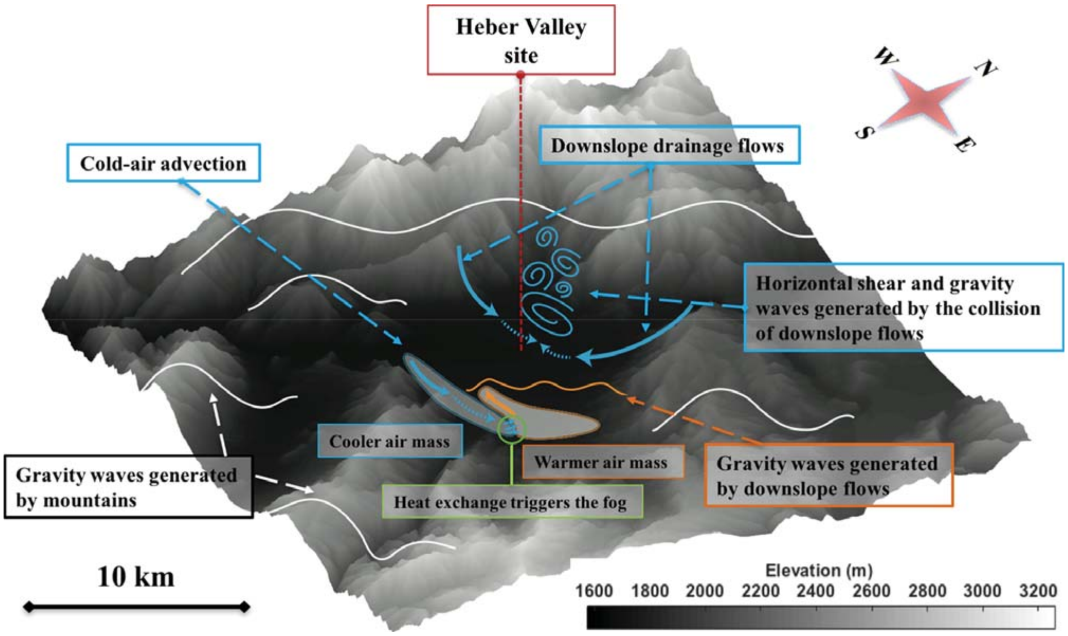

Figure 15
Conceptual figure of flow dynamics in the Heber valley on January 9, 2015

surface heating from below and radiative cooling at the fog top. This mixing seems to promote fog development by increasing the fog depth (Fig. 5f).

- 0900 MST: fog dissipates as a result of increasing temperature, which were caused by both surface heating and heat absorption by the fog particles from solar radiation.

To the best of our knowledge, this work is one of the few observational studies focusing on detailed explanations of the impact of flow dynamics on very shallow and short-duration valley fog. With the help of intensive turbulence measurements covering the near-surface layer, this work shows that mountain circulations play a critical role in the formation and development of shallow valley fog by modulating temperature and moisture fields through katabatic flow interactions and gravity waves. In particular, internal gravity waves modulate fog processes by varying the near-surface temperature. Our study revealed that drainage flows and cold-air pool sloshing can trigger fog formation. Hence, to accurately predict valley fog, numerical weather prediction models need to capture these small-scale mountain circulations, which is not a trivial task given their coarse resolution.

This case study revealed that to fully capture the complexity of fog formation in mountain terrain, a number of experimental set up limitations must be overcome. Future experiments should better characterize internal gravity waves using multiple microbarometers distributed in space. In addition, to better estimate the fog depth and spatial variability lidars should be deployed above the fog layer, scanning downward. Furthermore, to study the complexity of valley circulations, a large distributed array of automatic weather stations (with 2D sonics capable of capturing extremely weak winds) should be deployed throughout the valley.

5. *Conclusions*

This work presents a case study of a typical early morning, short-lived, patchy, mountain valley fog event, including how the fog is modulated by interactions with turbulence, wavelike motions and mountain circulations. The analysis is based on an intensive observation period carried out on January 9, 2015 in Heber Valley (Utah, USA), as part of the MATERHORN-Fog project.

Although visibility dropped at least ten times between 0400 and sunrise, there were three periods when visibility was less than 1 km, lasting, respectively, 19, 16 and 37 min. RH_w was consistently greater than 95 % until the start of the third fog episode, and then dropped to 90 % when the last fog episode dissipated. RH_i was greater than 100 % most of the time before 0900 MST, a possible indication of the occurrence of ice fog. An analysis of fog particle size distribution during the fog event revealed that the fog particles (sizes from 1.0 to 10.0 μm) were formed rapidly via water vapor condensation on cloud nuclei (sizes from 0.3 to 1.0 μm).

The net radiation flux remained constant at -45 W m^{-2} during the early morning period prior to sunrise, indicative of significant radiative cooling. The associated air temperature cooling rate was 0.5 °C h^{-1}. This cooling sustained a cold-air pool of $\approx$50–100 m agl that was present throughout the night with a stable vertical potential temperature gradient of about 0.13 °C m^{-1} and extremely light wind speeds (mostly $<$0.5 m s^{-1}). As soon as fog formed, temperatures in the shallow fog layer homogenized via convective mixing caused by radiative cooling (sinking cold air) at the fog top and surface heating (rising warm air), which promoted the fog development.

Several mountain circulations were observed, mostly originating from three directions (N, W, and S) before 0700 MST. We showed evidence that some of these drainage flows and the flow generated by cold-air pool sloshing collided, leading to strong horizontal shear instabilities and a TKE spike dominated by horizontal velocity fluctuations at 0620 MST. Drainage flows also triggered internal gravity waves near the surface. At 0700 MST, cold-air advection from the south triggered the start of the first fog episode.

Internal gravity waves also played a role in modulating the fog. Oscillating surface pressure and air temperature periodically forced the fog to form and dissipate during the fog period (0720–0900 MST). From wavelet analysis, oscillations with time periods of 15–20 min were noted throughout the whole night. The dominant time period of temperature and vertical velocity fluctuations was about 14 min. The mechanisms of temperature oscillations were various. They were the results of internal gravity waves, overturning vertical motions, downslope drainage flows, or the combination of these processes.

In summary, it is intuitive to state that the interaction of fog and turbulence in the stably stratified nocturnal boundary layer are extremely complicated, and even more so over complex terrain. Even though this case study was unable to make firm conclusive statements, it provides a detailed (yet partial) description of some of the connections between fog and flow dynamics over complex terrain.

Acknowledgments

This research was funded by the Office of Naval Research Award #N00014-11-1-0709, Mountain Terrain Atmospheric Modeling and Observations (MATERHORN) Program. We are grateful the John Pace and Dragan Zajic from the U.S. Army Dugway Proving grounds for their gracious help and instrument contributions to the project. The authors want to thank Stephan de Wekker for providing data from the automatic weather station. We would also like to thank Alexei Perelet, Derek Jensen, and Matt Jeglum for their help in the field. We are also extremely grateful to Grant Kohler and the Kohler family for the use of their farm during the experiment as well as all of the additional help that they regularly provided during the experiment. The authors are extremely grateful for all of the help during the field campaign, and the scientific insight provided by the MATERHORN team.

REFERENCES

Adedokun, J. A., & Holmgren, B. (1993). Acoustic sounder doppler measurement of the wind fields associated with a mountain stratus transformed into a valley fog: a case study. *Atmospheric Environment. Part A. General Topics, 27*, 1091–1098.

Ahrens, C.D. (2012). Meteorology today: an introduction to weather, climate, and the environment, 10th edn. (Cengage Learning).

Argentini, S., Mastrantonio, G., & Lena, F. (1999). Case studies of the wintertime convective boundary-layer structure in the urban area of Milan, Italy. *Boundary-Layer Meteorology, 93*, 253–267.

Bergot, T., & Guedalia, D. (1994). Numerical forecasting of radiation fog. Part I: Numerical model and sensitivity tests. *Monthly Weather Review, 122*, 1218–1230.

Bossche, M., & de Wekker, S.F.J. (2016). Spatiotemporal variability of surface meteorological variables during fog and no-fog events in the Heber Valley, UT; selected case studies from MATERHORN-fog. *Pure and Applied Geophysics* **(in press)**.

Choularton, T. W., Fullarton, G., Latham, J., Mill, C. S., Smith, M. H., & Stromberg, I. M. (1981). A field study of radiation fog in Meppen, West Germany. *Quarterly Journal Royal Meteorological Society, 107*, 381–394.

Cuxart, J., & Jiménez, M. A. (2012). Deep radiation fog in a wide closed valley: study by numerical modeling and remote sensing. *Pure and Applied Geophysics, 169*, 911–926.

Duynkerke, P. (1991). Observation of a quasi-periodic oscillation due to gravity waves in a shallow radiation fog. *Quarterly Journal Royal Meteorological Society, 117*, 1207–1224.

Duynkerke, P. (1999). Turbulence, radiation and fog in Dutch stable boundary layers. *Boundary-Layer Meteorology, 90*, 447–477.

Ellrod, G. P., & Gultepe, I. (2007). Inferring low cloud base heights at night for aviation using satellite infrared and surface temperature data. *Pure and Applied Geophysics, 164*, 1193–1205.

Fernando, H. J. S., Pardyjak, E. R., Di Sabatino, S., Chow, F. K., de Wekker, S. F. J., Hoch, S. W., et al. (2015). The MATERHORN: unraveling the intricacies of mountain weather. *Bulletin of the American Meteorological Society, 96*, 1945–1968.

Finnigan, J. J. (1988). Kinetic energy transfer between internal gravity waves and turbulence. *Journal of the Atmospheric Sciences, 45*, 486–505.

Fitzjarrald, D., & Lala, G. (1989). Hudson valley fog environment. *Journal of Applied Meteorology, 28*, 1303–1328.

Gerber, H. (1981). Microstructure of a radiation fog. *Journal of the Atmospheric Sciences, 38*, 454–458.

Golding, B. W. (1993). A study of the influence of terrain on fog development. *Monthly Weather Review, 121*, 2529–2541.

Gultepe, I., Fernando, H.J.S., Pardyjak, E.R., Hoch, S.W., Silver, Z., Creegan, E., Leo, L.S., Pu, Z., de Wekker, S., & Hang, C. (2016). Mountain ice fog: observations and predictability. *Pure and Applied Geophysics*. doi:10.1007/s00024-016-1374-0

Gultepe, I., Hansen, B., Cober, S. G., Pearson, G., Milbrandt, J. A., Platnick, S., et al. (2009). The fog remote sensing and modeling field project. *Bulletin of the American Meteorological Society, 90*, 341–359.

Gultepe, I., Isaac, G., Hudak, D., Nissen, R., & Strapp, J. W. (2000). Dynamical and microphysical characteristics of arctic clouds during BASE. *Journal of Climate, 13*, 1225–1254.

Gultepe, I., Isaac, G. A., Joe, P., Kucera, P., Theriault, J. M., & Fisico, T. (2012). Roundhouse (RND) mountain top research site: measurements and uncertainties for winter alpine weather conditions. *Pure and Applied Geophysics, 171*, 59–85.

Gultepe, I., Isaac, G. A., Williams, A., Marcotte, D., & Strawbridge, K. B. (2003). Turbulent heat fluxes over leads and polynyas, and their effects on arctic clouds during FIRE. ACE: aircraft observations for April 1998. *Atmosphere-Ocean, 41*, 15–34.

Gultepe, I., Minnis, P., Milbrandt, J., Cober, S. G., Nguyen, L., Flynn, C., et al. (2008). The fog remote sensing and modeling (FRAM) field project: visibility analysis and remote sensing of fog. *Remote Sensing Applications for Aviation Weather Hazard Detection and Decision Support, 7088*(12), 708803.

Gultepe, I., Tardif, R., Michaelides, S. C., Cermak, J., Bott, A., Bendix, J., et al. (2007). Fog research: a review of past achievements and future perspectives. *Pure and Applied Geophysics, 164*, 1121–1159.

Gultepe, I., Zhou, B., Milbrandt, J., Bott, A., Li, Y., Heymsfield, A. J., et al. (2014). A review on ice fog measurements and modeling. *Atmospheric Research, 151*, 2–19.

Haeffelin, M., Bergot, T., Elias, T., Tardif, R., Carrer, D., Chazette, P., et al. (2010). PARISFOG: shedding new light on fog physical processes. *Bulletin of the American Meteorological Society, 91*(6), 767–783.

Hodges, D., & Pu, Z. (2015). The climatology, frequency, and distribution of cold season fog events in Northern Utah. *Pure and Applied Geophysics*, 1–15. doi:10.1007/s00024-015-1187-6.

Holets, S., & Swanson, R. N. (1981). High-inversion fog episodes in Central California. *Journal of Applied Meteorology, 20*, 890–899.

Horel, J., Ptter, T., Dunn, L., Steenburgh, W. J., Eubank, M., Splitt, M., et al. (2002). Weather support for the 2002 winter olympic and paralympic games. *Bulletin of the American Meteorological Society, 83*(2), 227. **(24)**.

Jensen, D.D., Nadeau, D.F., Hoch, S.W., & Pardyjak, E.R. (2015). Observations of near-surface heat-flux and temperature profiles through the early evening transition over contrasting surfaces. *Boundary-Layer Meteorology*, 1–21. doi:10.1007/s10546-015-0067-z.

Kurita, S., Okada, K., Naruse, H., Ueno, T., & Mikami, M. (1990). Structure of a fog in the dissipation stage over land. *Atmospheric Environment. Part A. General Topics, 24*, 1473–1486.

Lareau, N. P., Crosman, E., Whiteman, C. D., Horel, J. D., Hoch, S. W., Brown, W. O. J., et al. (2013). The persistent cold-air pool study. *Bulletin of the American Meteorological Society, 94*, 51–63.

Lee, T. (1987). Urban clear islands in California central valley fog. *Monthly Weather Review, 115*, 1794–1796.

Mahrt, L. (2013). Stably stratified atmospheric boundary layers. *Annual Review of Fluid Mechanics, 46*, 23–45.

Manoj, M. G., & Devara, P. C. S. (2011). Quasi-periodic oscillations of aerosol backscatter profiles and surface meteorological parameters during winter nights over a tropical station. *Annales Geophysicae, 29*, 455–465.

Mason, J. (1982). The physics of radiation fog. *Meteorological Society of Japan, 60*, 486–499.

Meillier, Y. P., Frehlich, R. G., Jones, R. M., & Balsley, B. B. (2008). Modulation of small-scale turbulence by ducted gravity waves in the nocturnal boundary layer. *Journal of the Atmospheric Sciences, 65*, 1414–1427.

Monti, P., Fernando, H.J.S., Princevac, M., Chan, W.C., Kowalewski, T.A., Pardyjak, E.R. (2002), Observations of Flow and Turbulence in the Nocturnal Boundary Layer over a Slope, Journal Atmospheric Science. 59, 2513–2534

Müller, M. D., Schmutz, C., & Parlow, E. (2007). A one-dimensional ensemble forecast and assimilation system for fog prediction. *Pure and Applied Geophysics, 164*, 1241–1264.

Nappo, C. J. (2002). *An introduction to atmospheric gravity waves*. London: Academic Press.

National Oceanic and Atmospheric Administration (NOAA), (2005), Surface Weather Observations and Reports, (Federal Meteorological Handbook).

Pilié, R. J., Mack, E. J., Kocmond, W. C., Rogers, C. W., & Eadie, W. J. (1975). The life cycle of valley fog. Part I: micrometeorological characteristics. *Journal of Applied Meteorology, 14*, 347–363.

Porch, W. M., Clements, W. E., & Coulter, R. L. (1991). Nighttime valley waves. *Journal of Applied Meteorology, 30*, 145–156.

Price, J., Porson, A., & Lock, A. (2015). An observational case study of persistent fog and comparison with an ensemble forecast model. *Boundary-Layer Meteorology, 155*, 301–327.

Price, J. D., Vosper, S., Brown, A., Ross, A., Clark, P., Davies, F., et al. (2011). COLPEX: field and numerical studies over a region of small hills. *Bulletin of the American Meteorological Society, 92*, 1636–1650.

Pu, Z., Chachere, C.N., Hoch, S.W., Pardyjak, E., & Gultepe, I. (2016). Numerical prediction of cold season fog events over complex terrain: the performance of the WRF model during MATERHORN-fog and early evaluation. *Pure and Applied Geophysics*. doi:10.1007/s00024-016-1375-z.

Rees, J., Staszewski, W., & Winkler, J. (2001). Case study of a wave event in the stable atmospheric boundary layer overlying an Antarctic ice shelf using the orthogonal wavelet transform. *Dynamics of Atmospheres and Oceans, 34*, 245–261.

Richiardone, R., Alessio, S., Canavero, F., Einaudi, F., & Longhetto, A. (1995). Experimental study of atmospheric gravity waves and visibility oscillations in a fog episode. *II Nuovo Cimento C, 18*, 647–662.

Roach, W. T. (1976). On some quasi-periodic oscillations observed during a field investigation of radiation fog. *Quarterly Journal Royal Meteorological Society, 102*, 355–359.

Rodhe, B. (1962). The effect of turbulence on fog formation. *Tellus, 14*, 49–86.

Román-Cascón, C., Yagüe, C., Mahrt, L., Sastre, M., Steeneveld, G. J., Pardyjak, E. R., et al. (2015a). Interactions among drainage flows, gravity waves and turbulence: a BLLAST case study. *Atmospheric Chemistry and Physics, 15*, 9031–9047.

Román-Cascón, C., Yagüe, C., Sastre, M., Maqueda, G., Salamanca, F., & Viana, S. (2012). Observations and WRF simulations of fog events at the Spanish Northern Plateau. *Advances in Science and Research, 8*, 11–18.

Román-Cascón, C., Yagüe, C., Viana, S., Sastre, M., Maqueda, G., Lothon, M., et al. (2015b). Near-monochromatic ducted gravity waves associated with a convective system close to the Pyrenees. *Quarterly Journal Royal Meteorological Society, 141*, 1320–1332.

Steeneveld, G. J., Ronda, R. J., & Holtslag, A. A. M. (2014). The challenge of forecasting the onset and development of radiation fog using mesoscale atmospheric models. *Boundary-Layer Meteorology, 154*, 265–289.

Sun, J., Nappo, C. J., Mahrt, L., Belu, D., Stauffer, D. R., Pulido, M., et al. (2015). Review of wave-turbulence interactions in the stable atmospheric boundary layer. *Reviews of Geophysics, 53*, 956–993.

Terradellas, E., Ferreres, E., & Soler, M. R. (2008). Analysis of turbulence in fog episodes. *Advances in Science and Research, 2*, 31–34.

Thom, D. J. (1965). *The geography of heber valley*. Utah: University of Utah.

Torrence, C., & Compo, G. P. (1998). A practical guide to wavelet analysis. *Bulletin of the American Meteorological Society, 79*, 61–78.

Udina, M., Soler, M. R., Viana, S., & Yagüe, C. (2013). Model simulation of gravity waves triggered by a density current. *Quarterly Journal Royal Meteorological Society, 139*, 701–714.

Uematsu, A., Hashiguchi, H., Yamamoto, M. K., Dhaka, S. K., & Fukao, S. (2007). Influence of gravity waves on fog structure revealed by a millimeter-wave scanning doppler radar. *Journal Geophysical Research, 112*, D07207.

Underwood, S. J., Ellrod, G. P., & Kuhnert, A. L. (2004). A multiple-case analysis of nocturnal radiation-fog development in the central valley of California utilizing the goes nighttime fog product. *Journal of Applied Meteorology, 43*, 297–311.

Van Der Velde, I. R., Steeneveld, G. J., Wichers Schreur, B. G. J., & Holtslag, A. A. M. (2010). Modeling and forecasting the onset and duration of severe radiation fog under frost conditions. *Monthly Weather Review, 138*, 4237–4253.

Viana, S., Terradellas, E., & Yagüe, C. (2010). Analysis of gravity waves generated at the top of a drainage flow. *Journal of the Atmospheric Sciences, 67*, 3949–3966.

Viana, S., Yagüe, C., & Maqueda, G. (2009). Propagation and effects of a mesoscale gravity wave over a weakly-stratified nocturnal boundary layer during the SABLES2006 field campaign. *Boundary-Layer Meteorology, 133*, 165–188.

Welch, R. M., Ravichandran, M. G., & Cox, S. K. (1986). Prediction of quasi-periodic oscillations in radiation fogs. Part I: comparison of simple similarity approaches. *Journal of the Atmospheric Sciences, 43*, 633–651.

Whiteman, C. D., Zhong, S., Shaw, W. J., Hubbe, J. M., Bian, X., & Mittelstadt, J. (2001). Cold pools in the Columbia Basin. *Weather and Forecasting, 16*, 432–447.

Ye, X., Wu, B., & Zhang, H. (2014). The turbulent structure and transport in fog layers observed over the Tianjin area. *Atmospheric Research, 153*, 217–234.

Zhou, B., & Ferrier, B. S. (2008). Asymptotic analysis of equilibrium in radiation fog. *Journal of Applied Meteorology and Climatology, 47*, 1704–1722.

(Received May 27, 2016, revised July 15, 2016, accepted July 30, 2016, Published online August 10, 2016)

CHAPTER 4

NEAR-SURFACE POTENTIAL TEMPERATURE VARIANCE BUDGET FOR UNSTABLE ATMOSPHERIC FLOWS

Over the past decades, researchers have made significant progress toward a fundamental understanding of the budgets of turbulence variables over flat and homogeneous terrain, and only more recently over complex terrain. However, temperature variance budgets, which are parameterized in most meteorological models, are still poorly understood even under relatively idealized conditions. In this chapter, we rely on near-surface turbulence observations collected as part of the Mountain Terrain Atmospheric Modeling and Observations (MATERHORN) program. Daytime observations collected in May 2013 in western Utah at three field sites subjected to similar large-scale forcing are analyzed: a desert playa (i.e., dry lakebed), characterized by a flat surface devoid of vegetation; a vegetated site, characterized by a flat valley floor covered with greasewood vegetation; and a slope site with a local slope angle of 2-4° and covered by 1-m tall sparse desert steppe vegetation.

4.1 Introduction

The study of turbulence variance characteristics in the atmospheric boundary layer (ABL) is one of the key topics in fluid dynamics and numerical weather prediction (e.g., Abdella & McFarlane, 1997; Antonia et al., 1983; Asanuma & Brutsaert, 1999; Bradley et al., 1981; Caughey & Wyngaard, 1979; Mironov & Sullivan, 2016; Nadeau et al., 2011; Nilsson et al., 2016; Otić et al., 2005; Sempreviva & Højstrup, 1998; Shaw et al., 2001; Wyngaard & Coté, 1971;). The variance of velocity perturbations and the associated turbulent kinetic energy (TKE) has received considerable attention (Caughey & Wyngaard, 1979; Frenzen & Vogel, 1992; Nadeau et al., 2011). However, only a few studies have looked at the potential temperature variance budget (PTVB) under relatively idealized conditions, by means of field observations (Bradley et al., 1981; Champagne et al., 1977; Lee, 2009; Li et al., 2015; Shaw et al., 2001; Wyngaard & Coté, 1971), laboratory experiments (Antonia et al., 1983; Zhou & Antonia, 2000), and numerical simulations, most of which have used large-eddy simulations (LES) (Abdella & McFarlane, 1997; Mason & Derbyshire, 1990; Mironov & Sullivan, 2016).

The PTV budget indicates how turbulent thermal energy evolves and is distributed in the flow. In the atmosphere, various terms of the budget must be parametrized and included in turbulence closure models implemented in numerical weather prediction models (Mellor & Yamada, 1974). Moreover, temperature variance can also be used to estimate turbulent fluxes by means of flux-variance relationships (e.g., Albertson et al., 1995; Asanuma & Brutsaert, 1999; Detto et al., 2008; Katul et al., 1995; Kiely et al., 1996). However, these applications are limited by a lack of fundamental understanding of the potential temperature variance under certain situations. For instance, the applicability of the flux-variance method is questionable over complex terrain since Monin-Obukhov similarity theory (MOST) was derived assuming homogeneous and flat surfaces (Asanuma & Brutsaert, 1999; Kroon & de Bruin, 1995; Lloyd et al., 1991; Nadeau et al., 2013). It is, therefore, not a surprise to note that past studies on the PTV budget have almost exclusively focused on flat and uniform surfaces. These include Bradley et al., (1981), who analyzed turbulence characteristics over a uniform ≈0.12-m tall wheat field; Champagne et al., (1977); Kaimal et al., (1976), whose field site had a uniform roughness at the kilometer scale; Kiely et al., (1996), who analyzed flow over smooth uniform bare soil and crusted sand surfaces; and Shaw et al., (2001), whose surface of interest was composed of find-grained sediments with a small roughness. Even across these flat and homogeneous surfaces, the temperature variance budget can exhibit significant variability. In addition, only a few studies have considered non-ideal surfaces, such as sparse and open canopies (Lee, 2009), lakes (Li et al., 2015) and oceans (Edson & Fairall, 1998). Also, to the best of our knowledge, there have not been any studies investigating temperature variance at a slope site. It is desirable to have more observations over different surfaces to better understand the turbulence characteristics over realistic terrain. To avoid additional complexity associated with the transition periods and stable boundary layers, this work focuses on the potential temperature variance budget (PTVB) during convective periods over contrasting surfaces.

4.2 Theoretical Background

The temperature variance over flat terrain is typically scaled using MOST, such that (Monji, 1972; Wyngaard & Coté, 1972):

$$\frac{\overline{\theta^2}}{T^{*2}} = {C_2}^2 \left[-\frac{z}{\Lambda}\right]^{-2/3}, \tag{4.1}$$

where θ is the fluctuating potential temperature, T^* is the temperature scale, defined as:

$$T^* = -\frac{\overline{w\theta}}{u_*}, \tag{4.2}$$

In Eq. (4.2), $\overline{w\theta}$ is the vertical turbulent kinematic heat flux, u_* is the friction velocity, C_2 is a constant previously found to be 0.92 (Monji, 1972) or 0.95 (Wyngaard et al., 1972) under unstable stratification, z is the height above ground level, and L is the Obukhov length, written as:

$$L = -{u_*}^3\Theta_0/(\kappa g(\overline{w\theta})), \tag{4.3}$$

where Θ_0 is the potential temperature at the surface level (2–m level here), κ is the von Kármán constant, which is taken as 0.4 (Obukhov, 1946), and g is the gravitational acceleration. Despite the fact that Wyngaard & Coté (1972) have shown that Eq. (4.1) works well under convective periods, a comparison of scaled $\overline{\theta^2}$ over different surfaces, in particular over non-flat surfaces, has not been conducted.

The prognostic equation for the potential temperature variance budget may be written as (Antonia et al., 1980):

$$\underbrace{\frac{\partial\overline{\theta^2}}{\partial t}}_{\text{I}} + \underbrace{\overline{U_j}\frac{\partial\overline{\theta^2}}{\partial x_j}}_{\text{II}} = \underbrace{-2\overline{u_j\theta}\frac{\partial\overline{\Theta}}{\partial x_j}}_{\text{III}} - \underbrace{\frac{\partial\overline{u_j\theta^2}}{\partial x_j}}_{\text{IV}} - \underbrace{2\epsilon_\theta}_{\text{V}} + \underbrace{\epsilon_R}_{\text{VI}} + \underbrace{\alpha\nabla^2\overline{\theta^2}}_{\text{VII}} + \underbrace{\frac{2}{C_p}\overline{\theta\epsilon}}_{\text{VIII}}, \tag{4.4}$$

where t is time, $\overline{U_j}$ is the mean wind component in the j-direction; u_j is the wind fluctuation in the j-direction; $\overline{\Theta}$ is the potential temperature, α is thermal diffusivity, and C_P is the specific heat at constant pressure. Here, overbars are used for time averaging, ϵ_θ is the molecular dissipation of $\overline{\theta^2}$, ϵ is the molecular dissipation of turbulent kinetic energy, and ϵ_R is the radiation destruction.

In Eq. 4.4, term I is the local storage of $\overline{\theta^2}$. During unstable (i.e., mostly daytime) and stable (i.e., mostly nighttime) periods, this term is negligible compared to the dominant terms, such as production (term III) and dissipation (term V). Under steady-state conditions, this term can be neglected (e.g., Panofsky & Dutton, 1984).

Term II is the advection of potential temperature variance by the mean wind. This term can be neglected under the assumptions of horizontal homogeneity and weak subsidence (e.g., Deardorff, 1961).

Terms III and V, respectively, represent the production of $\overline{\theta^2}$ due to the interaction of the heat flux and the mean temperature gradient, as well as the molecular dissipation rate of $\overline{\theta^2}$, and are typically considered the dominant terms of Eq. (4.4) throughout the whole diurnal cycle. They have been the focus of most previous studies on the potential temperature variance budget (e.g., Antonia et al., 1980; Champagne et al., 1977; Monji, 1972; Shaw et al., 2001; Wyngaard & Coté, 1971, etc.). In second-order turbulence closure models, a perfect balance between these two terms is assumed to compute $\overline{\theta^2}$ (Mellor & Yamada, 1974). In practice, these two terms are rarely equal in magnitude, hence, it is common to look at the ratio of production to dissipation, also called the imbalance ratio. As a summary, Table 4.1 reports the imbalance ratios along with surface covers and stability conditions from a few previous studies. The imbalance ratio ranges from 0.75 (i.e., the dissipation dominates the budget), to 1.83 (i.e., the production dominates the budget). In their studies over plowed surfaces, Antonia et al., (1979) and Champagne et al., (1977) found that the imbalance ratio did not have any correlation with atmospheric stability. Bradley et al., (1981) and Kiely et al., (1996) reported higher values of the imbalance ratio under unstable conditions and the balance between production and dissipation of $\overline{\theta^2}$ under near-neutral conditions over flat terrain. Moreover, both Bradley et al., (1981) and Champagne et al., (1977)

Table 4.1: Review of production to dissipation of $\overline{\theta^2}$ ratio from field measurements. z/L is the Monin-Obukhov stability parameter.

$\frac{\text{Production}}{\text{Dissipation}}$	Surface	$-(z/L)$	Reference
0.86 – 1.8	Plowed soil surface	0.067 – 0.110	Champagne et al., (1977)
1.83/ 0.75/ 1.4	Plowed soil surface	0.08/0.50/0.45	Antonia et al., (1979)
1.43±0.3	Sparse wheat	0.1 – 0.7	Bradley et al., (1981)
1.06±0.13		0 – 0.1	
1.42	Uniform bare soil	2.0 – 8.0	Kiely et al., (1996)
1.14	Large basin with crusted sand	0.006 – 0.04	

explored possible reasons for the imbalance other than stability conditions, such as the need to include the radiation destruction term (term VI in Eq. (4.4)), the local storage, or even advection effects, but their analysis was inconclusive.

Term IV represents the turbulent transport of $\overline{\theta^2}$. This term has been neglected by most previous studies. Both Bradley et al., (1981) and Wyngaard & Coté (1971) found that this term was one order of magnitude smaller than the production term. However, Bradley et al. (1981) also found that the transport term was independent of stability conditions, which contradicts the finding of Wyngaard & Coté (1971), that the turbulent transport term is a sink term under unstable conditions and a source term under stable conditions. Sempreviva & Højstrup (1998) found turbulent transport processes to be small compared to production of $\overline{\theta^2}$ under convective conditions, while under near-neutral conditions, turbulent transport was more important. The relative strength of the transport term is certainly unclear under different stability conditions and over different surfaces.

Term VI in Eq. (4.4) is the radiation destruction term that tends to decrease $\overline{\theta^2}$ over small length scales, i.e., the effect of radiation is greater in the high-frequency end of the $\overline{\theta^2}$ spectrum (Plate, 1971). In addition to being extremely difficult to measure in the field, this term is typically one to two order of magnitude smaller than the molecular dissipation term (Coantic & Simonin, 1984). Hence, this process is neglected in most of the PTVB studies (Högström, 1990; Lumley & Panofsky, 1964; Wyngaard & Coté 1971), including here.

Term VII represents conductive diffusion of potential temperature variance, which is expected to be small compared with the production term (Antonia et al., 1980).

Finally, term VIII is the dissipation of kinetic energy into heat. Plate (1971) argued that this term is negligible due to the fact that the high-frequency end of the momentum spectrum contributes the most to $\overline{\theta\epsilon}$, whereas θ is small in the same range of spectrum.

In summary, under the assumptions of steady state, horizontal homogeneity (no advection), negligible subsidence and radiation destruction of $\overline{\theta^2}$, Eq. (4.4) can be written as:

$$0 = \underbrace{-\overline{w\theta}\frac{\partial\overline{\Theta}}{\partial z}}_{\text{III}} - \underbrace{\frac{1}{2}\frac{\partial\overline{w\theta^2}}{\partial z}}_{\text{IV}} - \underbrace{\epsilon_\theta}_{\text{V}}, \tag{4.5}$$

The objectives of this study are thus: 1) to characterize the vertical profile of potential temperature variance over different surfaces in the near-surface region; 2) to quantify the significant terms in the potential temperature variance budget equation; and 3) to show the variability of the budget terms as a function of height over three diverse surfaces exposed to similar large-scale forcing..

4.3 Methods

The analysis is supported by field observations collected within the Mountain Terrain Atmospheric Modeling and Observations (MATERHORN) program, which is designed to better understand atmospheric fluid dynamics across all scales over realistic mountainous terrain as well as under transient and steady conditions. The overall goal of the MATERHORN program is to improve mountain weather forecasts by developing scientific tools to help identify leaps in predictability. More details can be found in Fernando et al., (2015).

4.3.1 Experimental Sites

To study the behavior of the potential temperature variance over different surfaces, we analyze MATERHORN data collected during the spring campaign (1 to 31 May 2013) at three sites: Playa, Sagebrush, and Slope (Figure 4.1). These sites are all located at the U.S. Army Dugway Proving Ground (DPG), which is situated 137 km southwest of Salt Lake City, Utah. DPG is characterized by a dryland environment consisting of salt flats and isolated hills surrounded by interconnected mountains. Playa site (Figure 4.1b) is a highly alkaline desert playa (40°08′N, 113°27′W, 1296 m above mean sea level), which is mostly devoid of vegetation and characterized by a very flat surface and a heterogeneous soil moisture spatial distribution (Hang et al., 2015). The elevation variation is typically less than 1 m km^{-1} with an aerodynamics roughness length of 0.11 mm. Sagebrush site (Figure 4.1c) is a low-elevation valley floor covered by greasewood vegetation that is approximately 1-m high. It is located $\approx$ 25 km to the east of Playa site (40°07′N,

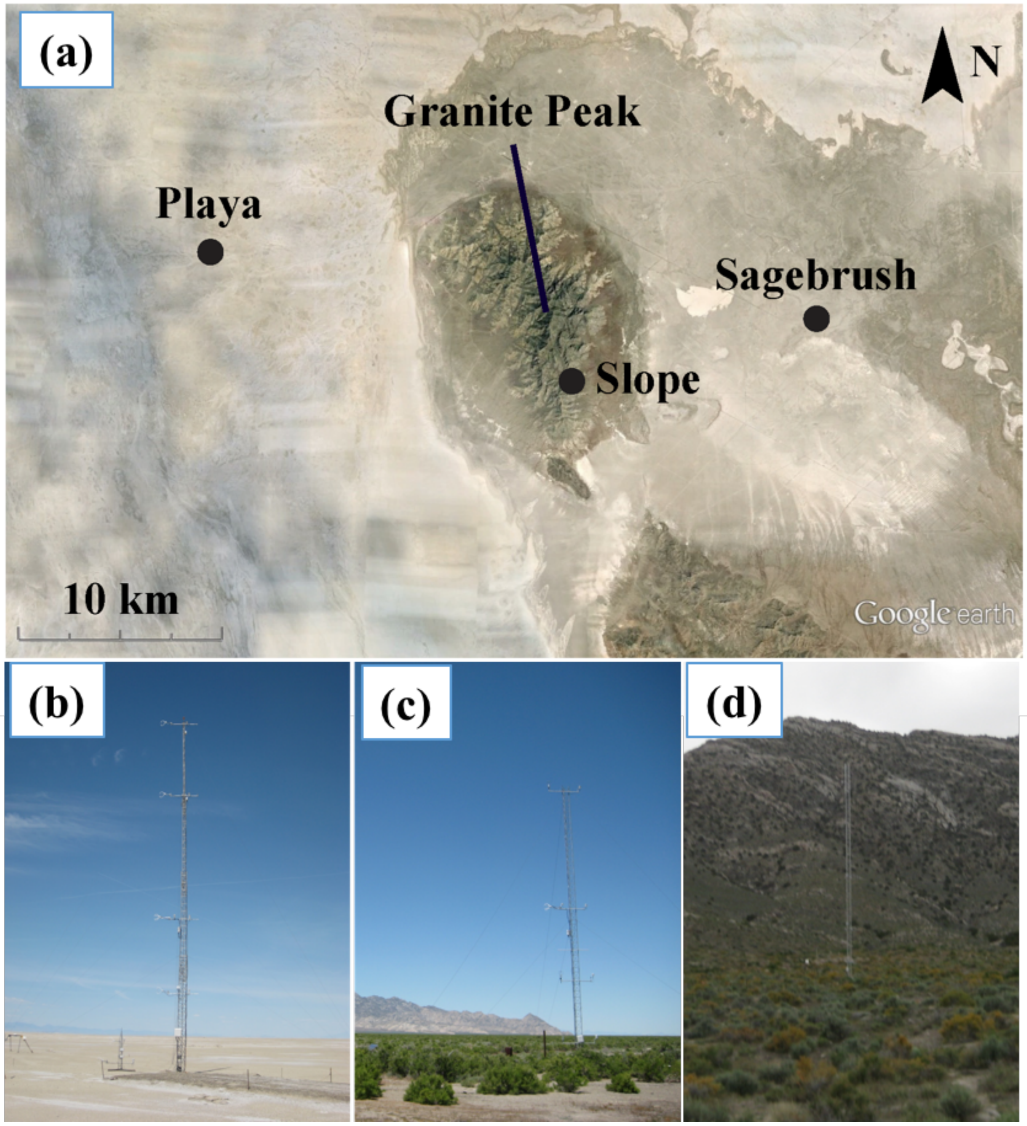

Figure 4.1: (a): Google Earth image of the three sites of interest at Dugway Proving Ground, UT; Photographs of (b): Playa; (c): Sagebrush; (d): Slope sites. Copyright 2017 Derek Jensen and Sebastian Hoch

113°7′W, 1316 m above mean sea level). The roughness length at Sagebrush site is 140 mm during spring season (Jensen et al., 2015). Slope site (Figure 4.1a) is covered with higher elevation desert vegetation on the east side of Granite Peak (Figure 4.1). The vegetation is sparse desert steppe on the order of 1-m height. The tower sits in the upper portion of the slope with a ridge-line pitch of 2 to 4° with a surface roughness length of 80 mm.

4.3.2 Instruments

Turbulence variables were measured at multiple levels between the surface and 25.5 m above ground level (agl) at the three sites of interest. At Playa site, the turbulence tower consisted of a 28-m mast equipped with CSAT3 sonic anemometers and 0.0127 mm type-E thermocouples at six levels (0.6, 2.0, 5.3, 10.4, 19.4, 25.5 m). At Sagebrush site, sonic anemometers and 0.0127 mm type-E thermocouples were used at five levels (0.5, 2.0, 5.9, 10.2, 18.2 m). A CSAT3 sonic anemometer was deployed at the 10.2-m level, while RM Young ultrasonic anemometers where deployed at all other levels. At the Slope site, the tower had five levels of CSAT3 sensors (0.6, 2.1, 5.1, 10.1, 20.1 m). A detailed list of instruments is presented in Table 4.2. All fast-response instruments were sampled at 20 Hz. Note that the lowest sonic anemometers (≈ 0.5 m) are below the vegetation height at both Sagebrush and Slope sites. Note that the lowest measurement level at Sagebrush and Slope sites is below the average canopy height (≈ 1 m). However, given the ratios of the surface roughness lengths (0.14 m for Sagebrush and 0.08 m for Slope) to the lowest measurement levels (0.5 m for Sagebrush and 0.6 m for Slope), we chose to keep these data in the analysis.

In order to measure high frequency temperature and velocity fluctuations, two sets of co-located 5 ¯m tungsten diameter hot-wires (55P16, Dantec Dynamic, Denmark) and 5 ¯m tungsten diameter cold-wires (Digital Flow Technologies Inc., East Lansing, MI) were deployed at Playa site, which is ≈10 m away from the turbulence tower, during ten Intensive Observation Periods (IOPs). The measurements were taken at 33 and 798 mm above ground during IOP 9 (Figure 4.2). The hot-wire array is a two-component X-array that measures the streamwise and vertical veloc-

Table 4.2: Instrumentation deployed at Playa, Sagebrush, and Slope sites. u, v, and w are the streamwise, spanwise and vertical velocity components, respectively. T is air temperature.

Instrument name	Variables measured	Accuracy	Manufacturer
CSAT3	u, v	± 0.08 m s^{-1}	Campbell Sci., Inc.
	w	± 0.04 m s^{-1}	
RMY8100	u, v, w	± 0.05 m s^{-1}	R.M. Young, Inc.
FW05	T	± 0.07 °C	Campbell Sci., Inc.

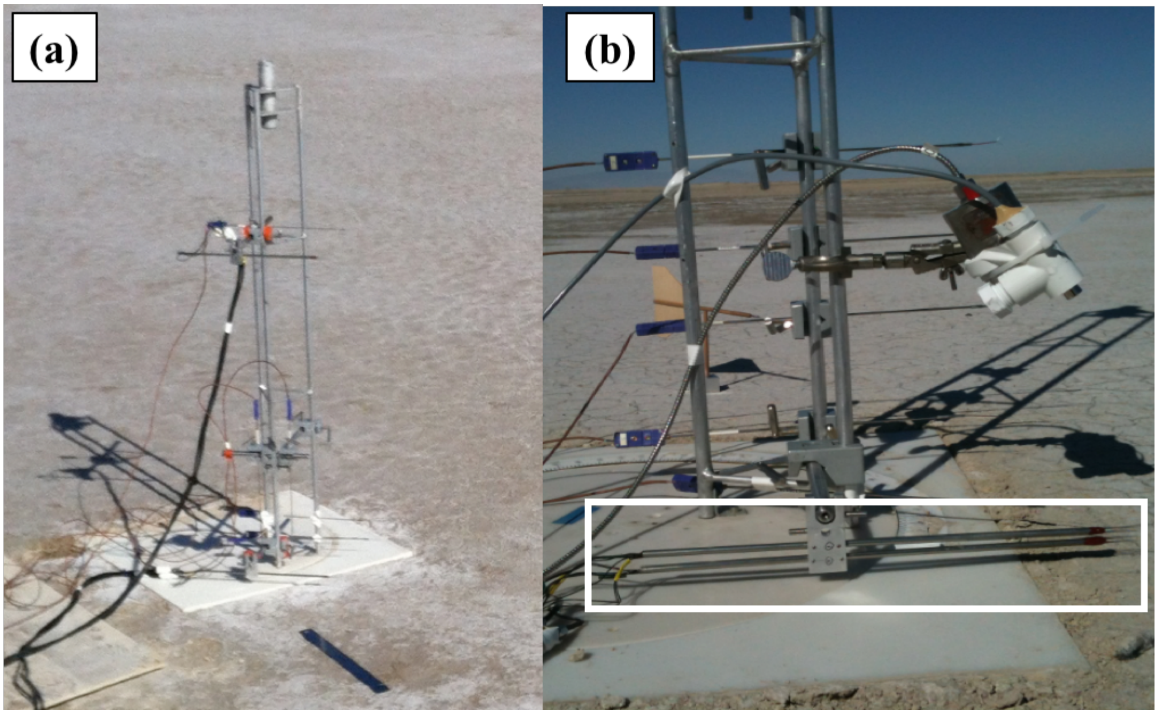

Figure 4.2: (a): Photographs illustrating the setup for the two sets of collocated hot-wire and cold-wire probes; (b): This photo shows two sets of probes. Each probe has 2 hot-wires (an X-array) and a single cold wire at 33 mm above ground level (in the white rectangle).

ity components. It must be regularly aligned with the mean wind. The cold-wire consists of a single straight wire. All three wires are spaced within approximately 33 mm. The hot-wire probe is calibrated by a portable unit that swept through different angles and speeds. The cold-wire is calibrated by air stream that is heated at two different temperatures. For the cold wire probe, a new correction was applied based on Arwatz et al., (2013) to provide frequency response to temperature fluctuations up to about 1 kHz. To compare the dissipation rate of $\overline{\theta^2}$ from direct method and indirect methods, we choose a data segment from 1330 – 1800 MST on 25 May 2013, which is under clear sky and strong south-westerly winds with a sustained wind speed of about 6 ms^{-1} at 1 m from the surface. During period, the surface layer is dominated by shear stress and the average turbulence intensity is less than 0.5. These conditions are ideal for the determination of the dissipation rate using the direct method, which is under the assumption of Taylor's hypothesis. The sampling frequency was 15 kHz.

4.3.3 Data Analysis and Availability

Raw turbulence data were processed with the Utah Turbulence in Environmental Studies Processes and analysis code (UTESpac). The eddy-covariance technique was applied to obtain turbulent fluxes using averaging periods of 30 min, which is long enough to filter the data noise and short enough to capture the contribution from turbulent transfer. More details on the turbulence flux corrections and quality control can be found in Jensen et al., (2015). At the slope site, a two-sector planar fit was applied with the sector-wise planar-fit coefficients computed from 30-min averaged wind data (see Jensen et al., 2016, for details). All meteorological data were averaged over 30-min periods as well. Data are selected during the period 0800 to 1700 MST to avoid the morning and afternoon transition periods. The average sunrise and sunset times during May 2013 are 0517 and 1939 MST, respectively. In addition, data with $z/L < 0$ at each level are selected as well to assure the presence of unstable conditions. Based on the previous criteria, the data availability for all sites are 3-6, 12-16, 21-27, and 30-31 May 2013. All vertical gradients are computed by means of finite difference techniques. A forward difference is used for the lowest level, a backward difference for the highest level, and an analytical derivative of a Lagrangian interpolating polynomial for the intermediate levels (Chapra & Canale, 1998).

4.3.4 Determination of the Dissipation Rate of $\overline{\theta^2}$

To compute the dissipation term, four methods are used: the so-called direct method, the spectral density approach, the second-order structure function, and the third-order structure function. Despite the fact that the direct method is expected to yield the most accurate estimation of dissipation rates, it is usually difficult to collect enough data to carry a sufficiently long analysis due to extremely high sampling frequency required. Indeed, the latter is typically greater than 10 kHz to allow the contribution of turbulent scales smaller than the so-called Kolmogorov microscale. As a result, in most practical applications, indirect methods are used.

Determination of ϵ_θ by means of direct method uses (Sreenivasan et al., 1977):

$$\epsilon_\theta = \alpha \, \overline{\left(\frac{\partial \theta}{\partial x_i} \right)^2}, \tag{4.6}$$

where α is thermal diffusivity of air. We also assume $T \approx \theta$ in this testing case. Under the assumptions of locally isotropic turbulence and Taylor's hypothesis, ϵ_θ can be approximated by:

$$\epsilon_\theta = 3\,\alpha \, \overline{\left(\frac{\partial \theta}{\partial x} \right)^2} \simeq 3\,\alpha\, U^{-1} \, \overline{\left(\frac{\partial \theta}{\partial t} \right)^2}, \tag{4.7}$$

where U is the local mean wind speed measured at the same location.

The three indirect methods are all based on inertial subrange scaling, which is applicable with measurements from 3-D sonic anemometer with a transducer spacing of 150 mm, and Taylor's hypothesis. A short description of all three methods will be given here, following the study of Kiely et al., (1996).

The spectral density of the temperature fluctuations in the Kolmogorov inertial subrange can be expressed as:

$$E_\theta(k) = \beta_\theta \, \epsilon_\theta \, \epsilon^{-1/3} \, k^{-5/3}, \tag{4.8}$$

where E_θ is the power spectra of θ at wavenumber k (rad m^{-1}), β_θ is the Obukhov-Corrsin constant, taken here as 0.8 (Wyngaard & Coté 1971). In Eq. (4.8), ϵ is the mean dissipation rate of turbulent kinetic energy calculated using the one-dimensional spectra:

$$E_u(k) = \alpha_u \, \epsilon^{2/3} \, k^{-5/3}, \tag{4.9}$$

where E_u is the power spectra of u at wavenumber k, α_u is the Kolmogorov constant, taken as 0.55 (Antonia et al., 1979).

With the second-order structure function approach, the dissipation of PTV can be written as (Obukhov, 1949):

$$D_{\theta\theta}(r) = C_{\theta\theta} \, \epsilon_\theta \, \epsilon^{-1/3} \, r^{2/3}, \tag{4.10}$$

where $D_{\theta\theta}(r)$ is the expected value of the temperature difference between two points separated by a distance r along the wind direction, which can be evaluated by $D_{\theta\theta}(r) = (\Delta\theta(r))^2$, where $\Delta\theta(r) = \theta(x+r) - \theta(x)$; the constant $C_{\theta\theta} = 4\beta_\theta$; the streamwise velocity fluctuation dissipation ϵ is obtained using:

$$D_{uu}(r) = C_{uu} \, \epsilon^{2/3} \, r^{2/3}, \tag{4.11}$$

where D_{uu} is the expected value of longitudinal velocity difference; $C_{uu} = 4.0\alpha_u$.

The third-order structure function of streamwise velocity and squared temperature differences as a function of r in the inertial subrange may be written as (Yaglom, 1948):

$$D_{u\theta\theta}(r) = -\frac{4}{3} \, \epsilon_\theta \, r, \tag{4.12}$$

The advantage of this method is not requiring free constants, and a *priori* knowledge of the dissipation rate of the turbulent kinetic energy.

4.4 Results and Discussion

4.4.1 Stability Conditions

The probability distribution of local stability parameter (z/Λ) is presented in Figure 4.3 for the data acquired during May 2013, where Λ is the local Obukhov length, which is determined by computing local values of u_*, Θ_v, and $\overline{w\theta}$ at each level. More than 60% of the data at the lowest level are within the near-neutral

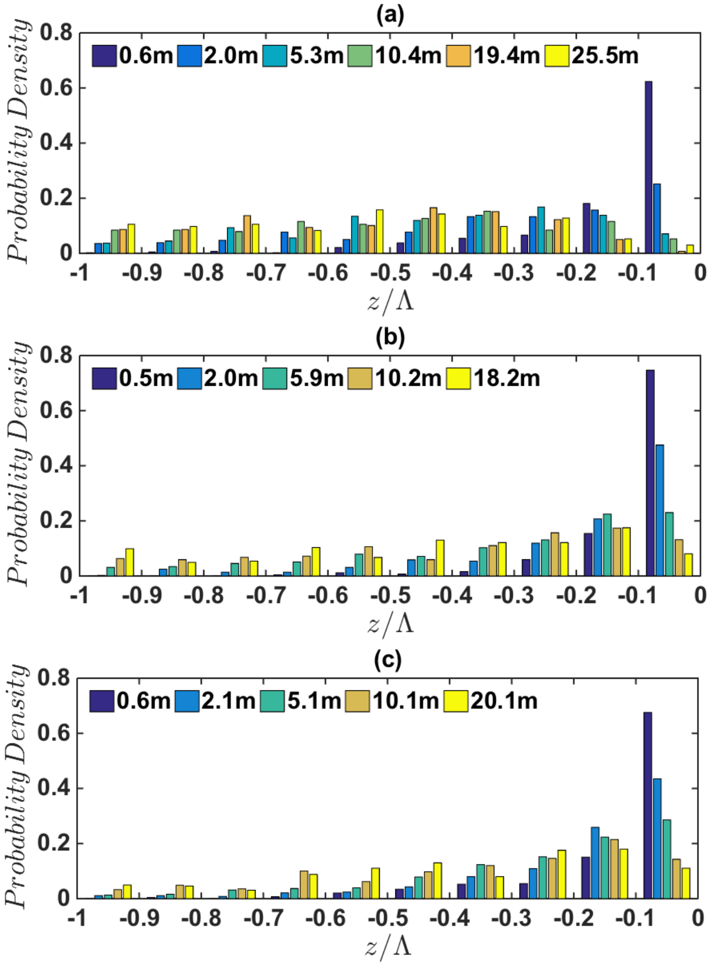

Figure 4.3: Probability density of the stability parameter z/Λ at a) Playa; b) Sagebrush; c) Slope sites at all measurement levels. The span for each interval is 0.1, except for the leftmost interval, which represent the probability density of $z/\Lambda < -1$.

range (i.e., $-0.1 < z/\Lambda < 0$) at all three sites. At Sagebrush and Slope sites, the probability density decreases with as conditions become more unstable. The ranges of z/Λ for the period of interest in this study are -0.005 to -12 at Playa site, -0.0017 to -5.78 at Sagebrush site, and -0.0007 to -13.28 at Slope site. These data have been used to compute ensemble averages for convective conditions in the following analysis.

4.4.2 Profiles of Potential Temperature Variance

Figure 4.4 shows the contour plots of ensemble averaged $\overline{\theta^2}$ at all three sites. A clear diurnal cycle can be observed at all sites. $\overline{\theta^2}$ at Sagebrush site has the greatest value among the three sites. Between 0800 and 1700 MST (indicated by two vertical dashed lines), the evolution of temperature variance displays different features over three sites. By comparing Playa site (smooth surface) to Sagebursh and Slope Sites (rough surfaces), we can see that the magnitude of $\overline{\theta^2}$ at Playa with the maximum value of 1.82 K^2 is noticeably smaller than at Sagebrush and Slope sites with peak values of 2.87 K^2 and 2.10 K^2, respectively. This is due to the fact that rough surfaces generate more turbulence and thus more fluctuations of temperature around its mean value.

To investigate the behavior of the profiles during unstable periods and the applicability of existing scaling relationships (i.e., Eq. (4.1)), the temperature scale (T^{*2}) and Obukhov length scale (L) in Eq. 4.1 are expanded so that Eq. (4.1) can be expressed as:

$$\overline{\theta^2} = C_\theta \left[\frac{z\,g}{\Theta_v \left(\overline{w\theta}\right)_s^2} \right]^{-2/3}, \tag{4.13}$$

where C_θ is a constant equal to 1.66 (${C_2}^2\kappa^{-2/3}$),with C_2 taken as 0.95 (Wyngaard & Coté, 1972).

The plots on the left side of Figure 4.5 show scaled $\overline{\theta^2}$ based on observations and models as a function of z/Λ at all three sites. At Playa site, R-squared (R^2) is 0.34 when using the literature value of the constant $C_2 = 0.95$, and 0.61 when using $C_2 = 1.35$ as calculated from a best-fit of the data. It is clear that the performance of the potential temperature variance model is improved significantly by using another C_2 value. At Sagebrush site, $R^2 = 0.34$ when $C_2 = 0.95$, and 0.41 when

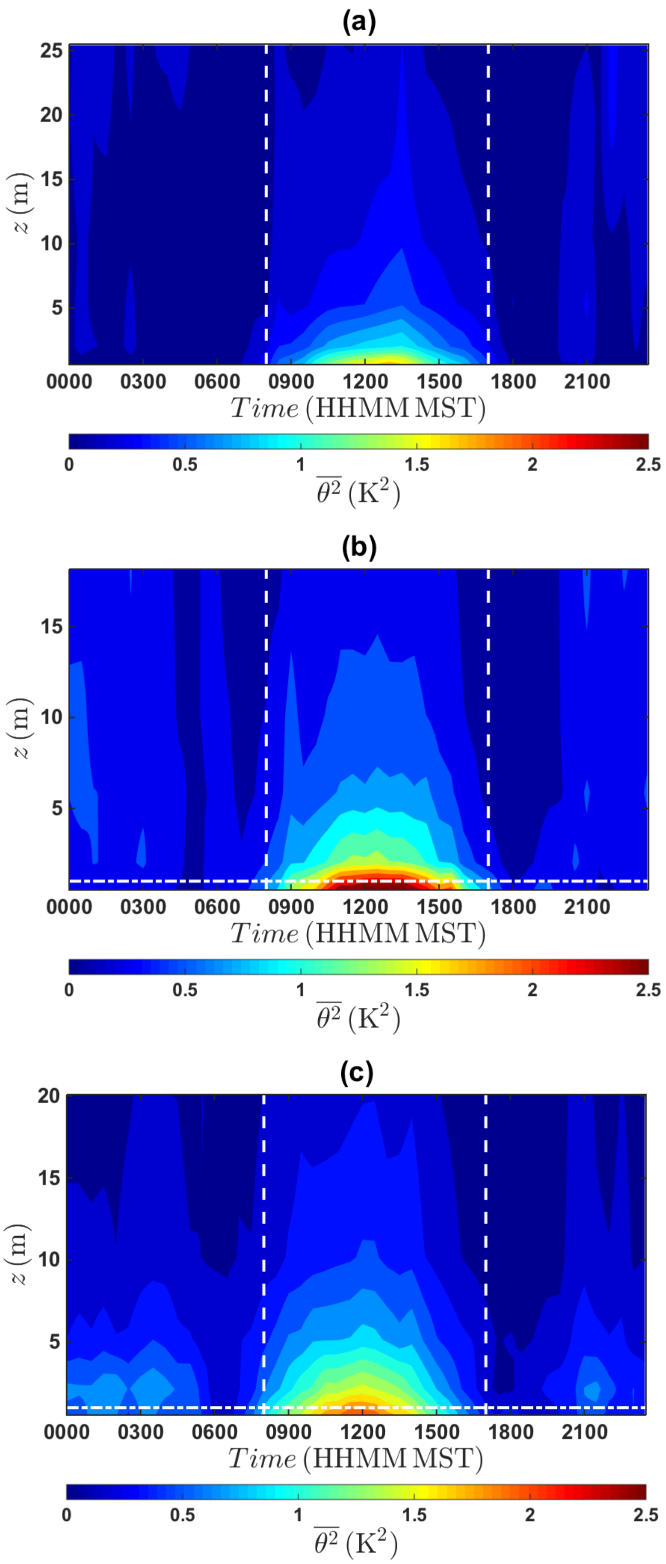

Figure 4.4: Contour plots of ensemble averaged $\overline{\theta^2}$ at (a): Playa; (b): Sagebrush; (c): Slope sites. White horizontal dashed lines at (b) and (c) indicate the approximate height of the vegetation when present ($\approx$1 m).

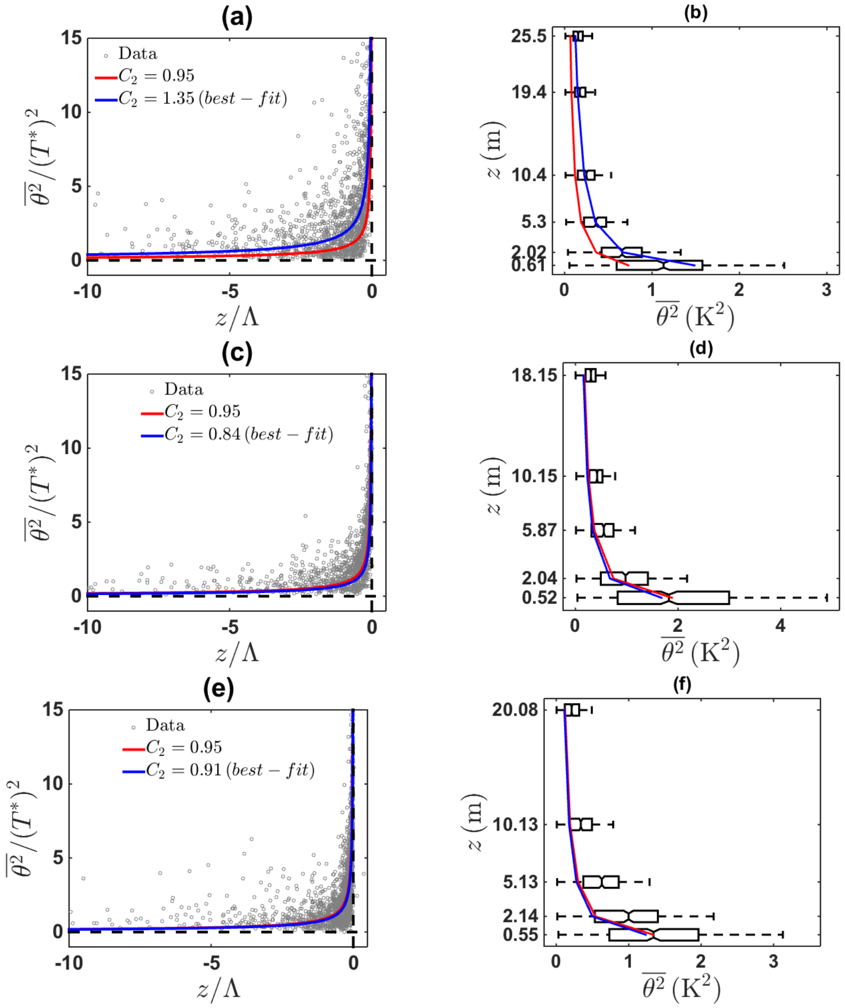

Figure 4.5: Left panel: normalized $\overline{\theta^2}$ by T^{*2}. Gray dots are the observational data. C_2 is the constant in Eq. (4.1). Red lines indicate the model with $C_2 = 0.95$; blue lines represent C_2 by best-fit of all the data. Right panel: Boxplots of $\overline{\theta^2}$ during daytime (0800 to 1700 MST). Centers of the black boxes indicate the medians of $\overline{\theta^2}$, the edges show the lower and upper quartiles. Red solid lines denote medians of the model based on Eq. (4.13) with C_θ=1.75 (C_2=0.95) at each level; blue solid lines represent the same with C_θ (C_2) equal 3.38 (1.35) at Playa site, 1.39 (0.84) at Sagebrush site, and 1.53 (0.91) at Slope site that based on the model best fits the observational data. (a-b): Playa site; (c-d): Sagebrush site; (e-f): Slope site. Note that both Θ_v and $\overline{(w\theta)}_s$ are obtained at bottom level ($\approx$ 0.5 m at three sites).

$C_2 = 0.84$ from the present data, which shows a small improvement on the model performance. At Slope site, $R^2 = 0.44$ when $C_2 = 0.95$, and 0.46 when $C_2 = 0.91$ as calculated from the present data. After computing a best fit of Eq. (4.1) to the data, C_2 at Playa departs from 0.95 the most among all three sites. The departure from the accepted values are clearly caused by scatter in the data at Playa site. The possible reason for strong variation of $\overline{\theta^2}$ at Playa can be: 1) the surface heterogeneity of soil moisture and evaporation at playa site causes strong surface temperature variation (Hang et al., 2015); 2) the larger surface roughness at Sagebrush and Slope sites origins a relatively turbulent momentum, that tends to smooth the temperature variance. Nevertheless, this result indicates that $\overline{\theta^2}$ scaling works better over relatively rough surfaces like Sagebrush and Slope than over smooth surface like Playa. The right panel of Figure 4.5 shows unscaled vertical profiles of potential temperature variance (box-plots in the figure) throughout the field campaign during convective periods along curves (red and blue solid lines in the figure) based on Eq. (4.13) with different values of C_θ (i.e., 3.38, 1.39, and 1.53 for Playa, Sagebrush, and Slope sites, respectively). In general, the model (with either constant value) can capture the vertical variation of the medians of $\overline{\theta^2}$ at all sites, where a sharp vertical gradient can be observed below 5 m and a relatively constant $\overline{\theta^2}$ layer can be seen above that same height. At Sagebrush and Slope sites, the profiles of $\overline{\theta^2}$ are almost identical.

4.4.3 Temperature Variance Budgets

To better understand how each term of the simplified temperature variance budget (Eq. (4.5)) varies in the vertical direction, medians of unscaled and scaled production, turbulent transport, and dissipation of $\overline{\theta^2}$ are analysed (Figure 4.6). Note that the determination method of dissipation rate here is the second-order structure function, which provides the most consistent results comparing to the spectral density and the third-order structure function methods. From the unscaled plots, both production and dissipation terms show a rapid decrease with height between the lowest level (0.6 m) to $\approx$5 m agl, then they become much smaller above this level. To provide an appreciation of the depth of this shallow

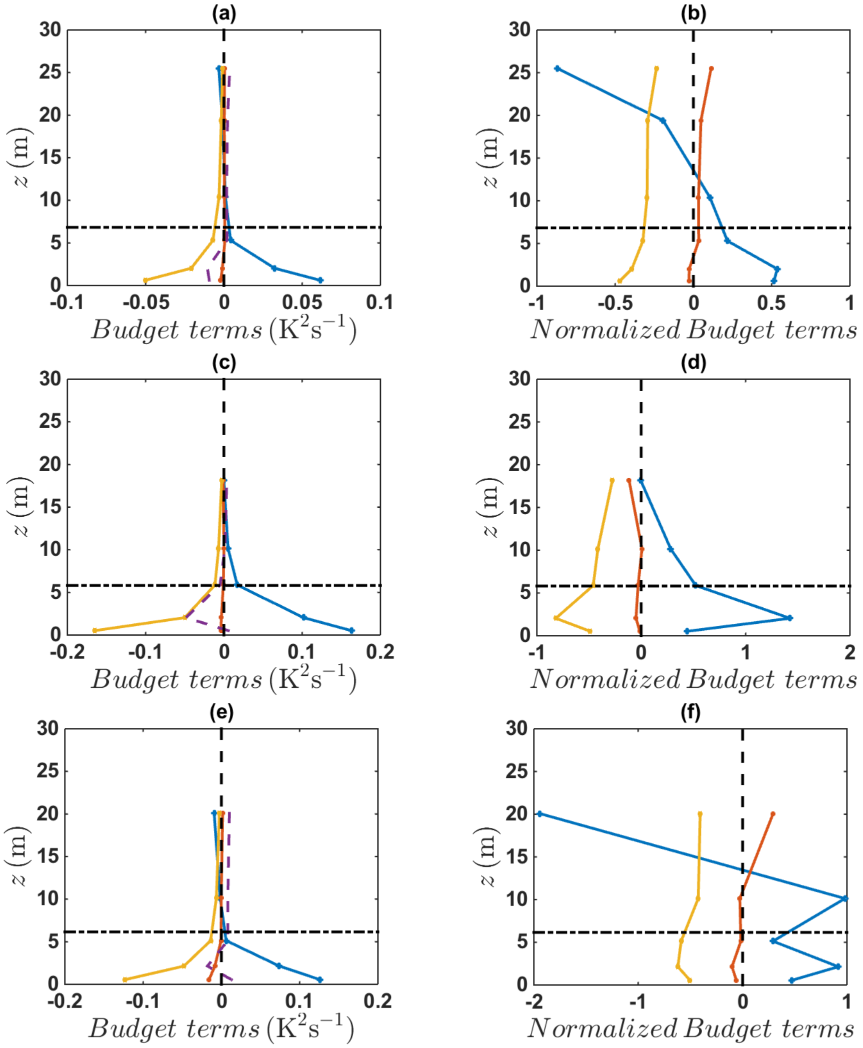

Figure 4.6: Left panel: medians of temperature variance budget and the residual term, which are indicated by purple dashed lines, (Production + Transport+Dissipation+Residual = 0) during the convective time periods (0800 to 1700 MST). Blue, red and orange lines indicate the production, turbulent transport and dissipation terms of $\overline{\theta^2}$, respectively. Black horizontal dashed lines represent the top of the layer above which $\overline{\theta^2}$ is less than 20% of its bottom value. Right panel: medians of scaled budget terms normalized by $u_* T^{*2}/(kz)$ at each level. All the color and dashed lines are the same as the left panel. (a-b): Playa site; (c-d): Sagebrush site; (e-f): Slope site.

layer characterised by strong vertical gradients, we illustrate the height above which the median of the temperature variance drops to less than 20% of its surface value. The top of this layer is indicated with a horizontal black dashed line in Figure 4.6. The depth of the shallow surface layer is rather constant across the sites (5.6 m at Playa site, 6.0 m at Sagebrush site, and 6.1 m at Slope site), despite the difference in surface roughness and slope angle. Above 5 m, all the terms are at least one order-of-magnitude smaller than the values found below. The residual below 5 m at Playa has negative values, which indicates a dominant production term within this shallow 5-m layer. The possible missing sink term in the budget can be the radiation destruction term. The residual at Sagebrush site is close to zero except at 2 m agl with the magnitude being as large as the dissipation term.

From Figure 4.6d, we notice that at the 2-m level, the normalized production term is greater than unity. This implies that the negative residual at 2 m is caused by an unusual large production. At Slope site, the residual term is relatively small over all heights, which indicates a good balance for the simplified potential temperature variance budget. The right panel of Figure 4.6 shows medians of scaled budget profile normalized by $u_* {T^*}^2/(kz)$. The normalized dissipation term shows a relatively constant profile during the convective period at all three sites. The scaled production profile displays a complicated behaviour over three different sites. In particular, at Playa site, the production term becomes negative above 10 m. This is caused by a negative temperature gradient due to the subsidence, which is also observed from Jensen et al. (2015) based on tethered balloon data.

4.4.4 Turbulent Transport

Turbulent transport of PTV has been reported to be a negligible term by most previous studies. However, Bradley et al., (1981) and Sempreviva & Højstrup (1998) have shown that it can not be neglected intermittently under near-neutral conditions. To further investigate the importance of turbulent transport in PTVB, we plot the histogram showing the ratio of turbulent transport to production of $\overline{\theta^2}$ at the same height (Figure 4.7). From Figures 4.5 and 4.6, we know that the temperature variance budget evolves rapidly with height in the first few meters

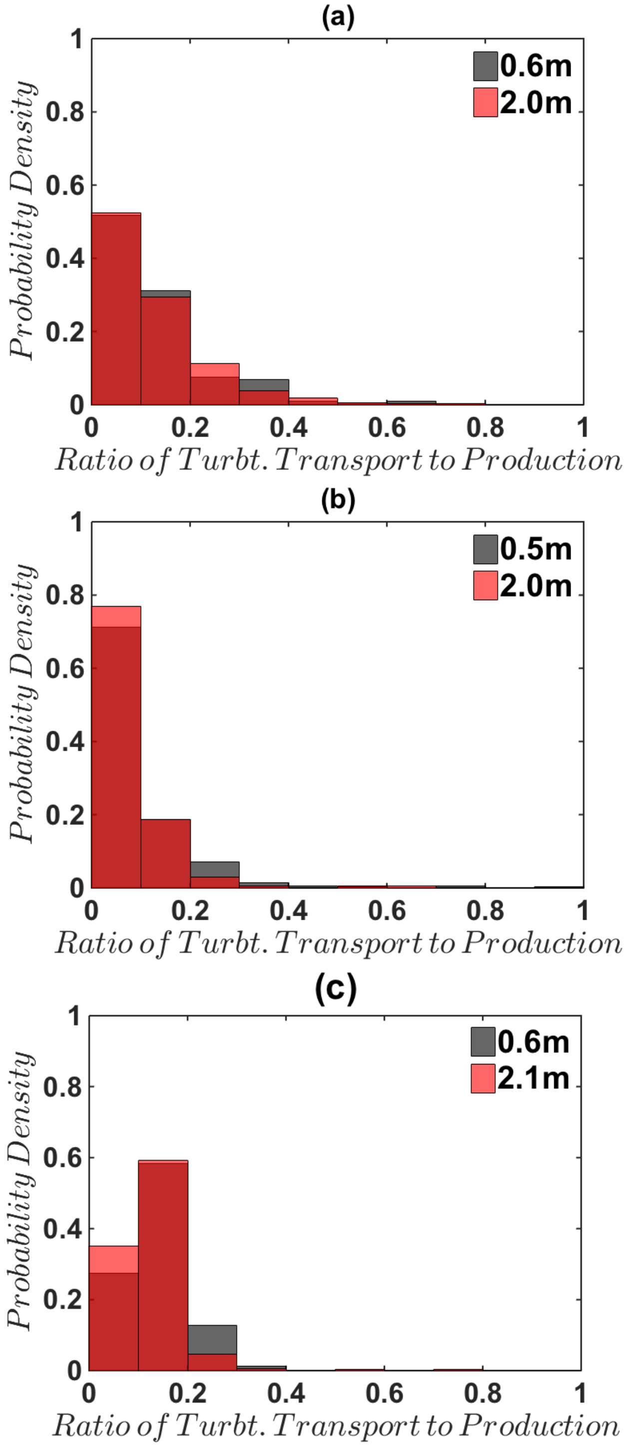

Figure 4.7: Probability density of the ratio of turbulent transport of PTV at the bottom two measurement levels to the production term at the same level at a) Playa, b) Sagebrush, and c) Slope sites.

above ground level, so the following discussion of turbulent transport will focus on the lowest two levels only. From Figure 4.7, we can see that there are more than 45% and 14% of the data segments with a ratio greater than 0.1 and 0.2, respectively, at Playa site. This result indicates that the turbulent transport may not be negligible over perfectly smooth surfaces like Playa site. However, at Sagebrush site, there are only ≈20% and 10% of data with a ratio greater than 0.1 and 0.2. The difference between two sites can be caused by the different in surface roughness. At Slope site (Figure 4.7c), the shape of the distribution is different from the other two sites. The ratio peaks between 0.1 and 0.2. The exact cause of this feature is still unclear. One possible reason could be related to the presence of daytime upslope flows. Furthermore, almost 70% of data has the ratio greater than 0.1, which might indicate that the turbulent transport term is not negligible over slope.

The turbulent transport term could also play a significant role in transferring the temperature variances through different layers. Figure 4.8 shows the ensemble averaged turbulent transport term at the three sites. Figure 4.8a indicates a clear separation between 0.6 - 2 m and 5 - 25.5 m at Playa. In the bottom layer, turbulent transport is acting as a sink term and in the upper layer, as a source term. From Figure 4.8b, we can see that the turbulent transport over Sagebrush at the lowest two levels is still a sink term in the $\overline{\theta^2}$ budget between 0700 – 1700 MST and becomes a source term between 1700 – 1900 MST. At 5.9 m level, turbulent transport acts as a sink term as well without significant variation during daytime. However, at the highest two levels, turbulent transport varies notably. Based on 30-min averaged data, the temporal variation of turbulent transport is significant on a daily base (not shown here). Overall, the behavior of turbulent transport at different heights at the Sagebrush site is more complicated than those at playa and slope sites. Figure 4.8c shows the diurnal cycle of the transport term at the Slope site. At midday, the transport is large and positive near the ground, decreases with height and is negative at the 20-m level. Overall, turbulent transport at all three sites transfers the temperature variance upwards with a relatively strong magnitude at the bottom two levels, and then its behavior is less consistent above the 5-m level from site to site.

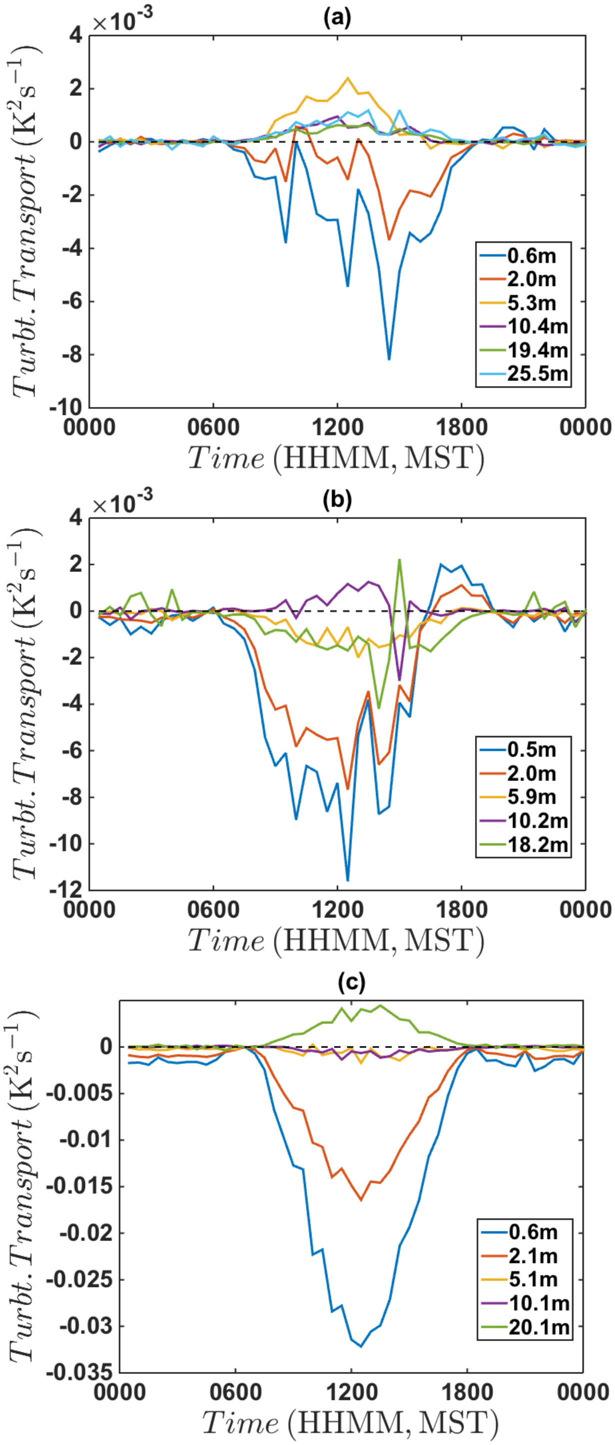

Figure 4.8: 24-hr Ensemble averaged turbulent transport of $\overline{\theta^2}$ throughout the periods of interest at all levels at a) Playa site, b) Sagebrush site, and c) Slope site.

To investigate how turbulent transport of $\overline{\theta^2}$ varies with atmospheric stability, we analyze the relationships between the ratio of turbulent transport to production and the local stability parameter z/Λ (Figure 4.9). Region (v) in Figure 4.9, where $-0.05 < z/\Lambda < 0$, which we consider considered as near-neutral conditions, shows the greatest variability,, which is consistent with the findings of Bradley et al., (1981) and Sempreviva & Højstrup (1998). However, the medians show that turbulent transport term is still small compared to production under near-neutral conditions. In fact, the medians at all three sites are relatively in dependent of stability in the convective boundary layer. The similarity between all three sites indicate that the importance of turbulent transport in the temperature variance budget is not very sensitive to variations in surface roughness and slope angles.

4.4.5 Dissipation

In this section, we attempt to intercompare different methods to determine ϵ_θ using a short-period during which direct calculations of ϵ_θ were possible. Due to the fact that the hot-wire and sonic-anemometers are measuring at different heights, an interpolation of ϵ_θ based on the indirect methods is required. In this case, a two-term exponential function (i.e., $\epsilon_\theta(z) = a \cdot exp(b \cdot z) + c \cdot exp(d \cdot z)$) is is used to interpolate ϵ_θ profiles with $R^2 = 0.99$. Figure 4.10 shows that ϵ_θ from the direct method varies significantly compared to ϵ_θ from the three indirect methods. Moreover, after 1700 MST, ϵ_θ from the indirect methods shows a clear decay and becomes almost negligible. However, ϵ_θ from the direct method is still active until 1800 MST. This extension of dissipation from the direct method is due to the fact that the hot-wire is measuring the flow with smaller length scale compared to sonic anemometers. The difference between the four methods could easily cause an imbalance between the production and dissipation terms, which is usually about 20%. Nevertheless, ϵ_θ from indirect methods is still valuable when we comparing to the production term to evaluate the imbalance ratio, which will be discussed in the following section.

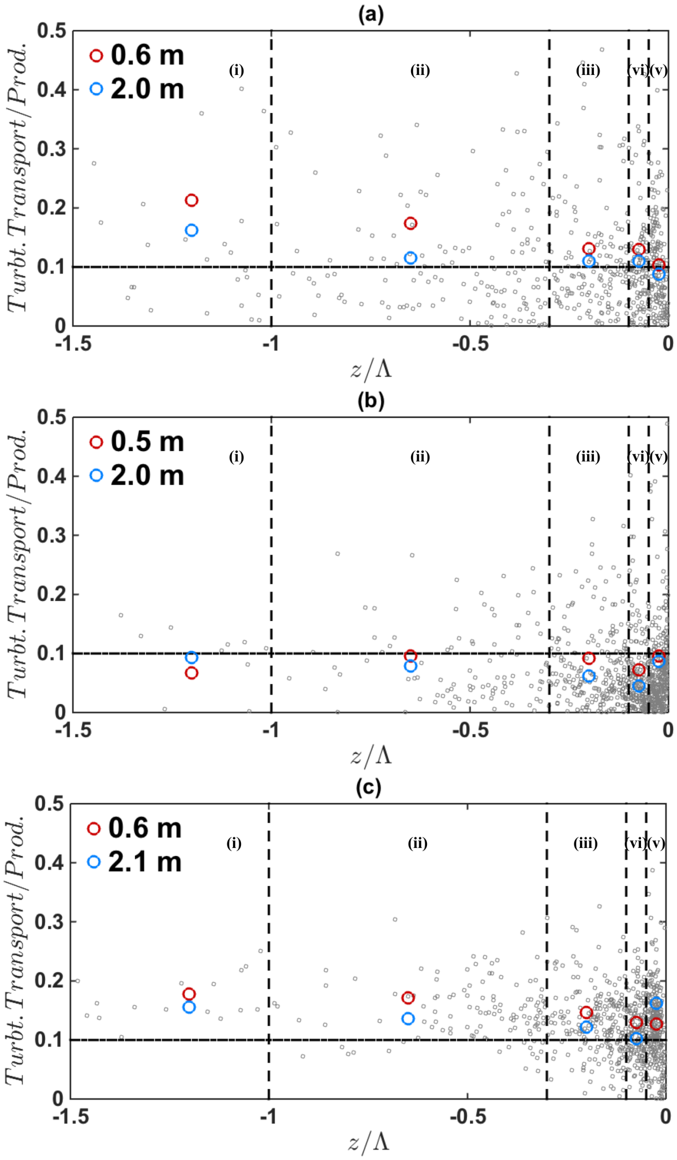

Figure 4.9: Ratio of turbulent transport to production term of $\overline{\theta^2}$ at a) Playa site, b) Sagebrush site, and c) Slope site. Gray dots represent 30-min average data at the bottom two levels, and red and blue dots represent bin-averaged ratio at two different heights over different ranges of z/Λ as indicated: (i) z/Λ < -1; (ii) -1< z/Λ <0.3; (iii) -0.3 < z/Λ < -0.1; (iv) -0.1 < z/Λ < -0.05; (v) -0.05 < z/Λ < 0.

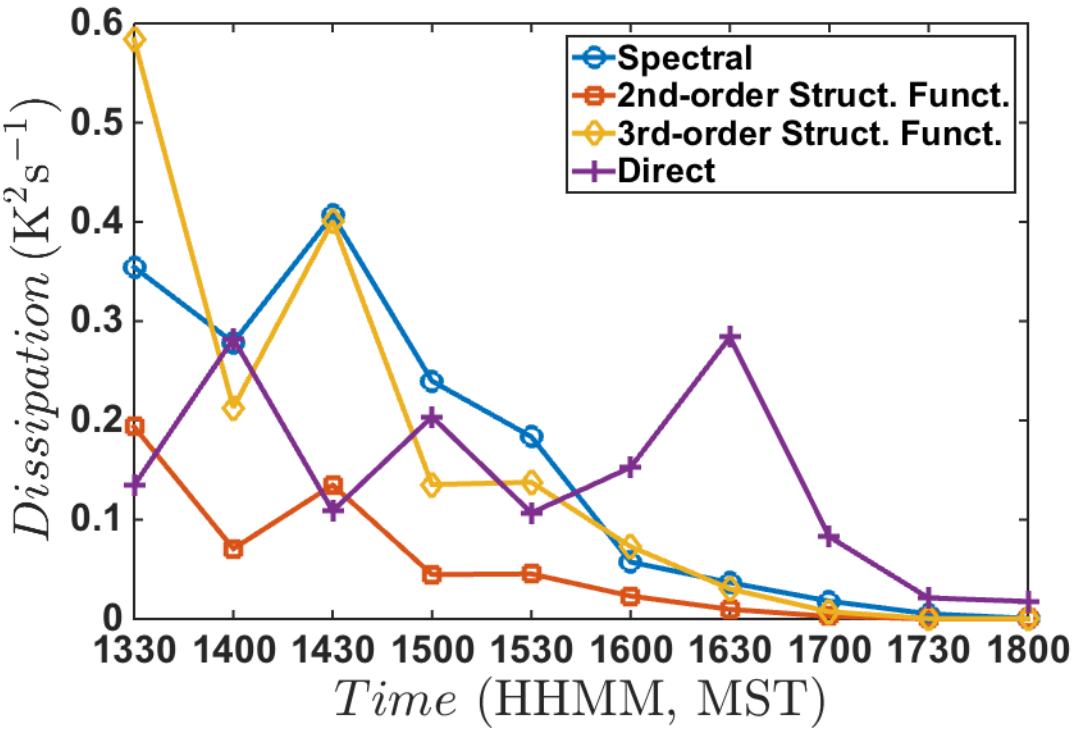

Figure 4.10: Time series of ϵ_θ at 0.6 m determined by the Spectral density, the second-order structure function, the third-order structure function, and the Direct methods on 25 May 2013 at Playa site.

4.4.6 Imbalance Ratio between Production and Dissipation

Previous studies have failed to clearly describe the relationship between the imbalance ratio (production to dissipation) and stability conditions. Figure 4.11 shows the imbalance ratio as a function of local stability parameter for all three sites. As discussed in the previous section, the determination of dissipation rate will certainly affect the imbalance ratio. To achieve the most information from the observational data, we will present the data based on both the second-order structure function and the third-order structure function, which are commonly used in previous studies (Kiely et al., 1996; Li et al., 2015).

Figure 4.11 shows that both 30-min averaged and bin-averaged imbalance ratio have a greater value when the dissipation is calculated with the second-order structure function. In addition, the ratio remains almost constant as z/Λ more negative at all three sites, which suggests no correlation between these two variables. From Figure 4.11a, taken at the 0.6 m level, the imbalance ratio becomes much smaller than unity, which indicates dissipation rate dominates production, as z/Λ becomes smaller than -0.3. In particular, when z/Λ is less than -1, the imbalance ratio is less than 0.5. This result is very different from what Kiely et al., (1996) observed over uniform bare soil, which is very similar to Playa site. As listed in Table 4.1, they reported an imbalance ratio of 1.42 when z/L is less than -2. This important difference of temperature variance budget closure can be caused from the basic assumption of assuming horizontal homogeneity. Hang et al., (2015) have reported a strong heteogeneity in surface temperature at the Playa site, consistent with the spatial distribution of soil moisture.

4.5 Summary

This work studies the potential temperature variance and budget terms under unstable conditions over a flat desert playa site without vegetation, a flat sagebrush site with 1-m tall sparse bushes, and a $2^\circ - 4^\circ$ slope site with higher elevation desert vegetation. The analysis is based on data acquired during the 2013 spring campaign at Dugway, UT, as part of the MATERHRON program.

Contour plots of $\overline{\theta^2}$ revealed clear diurnal cycles at the three sites. The average

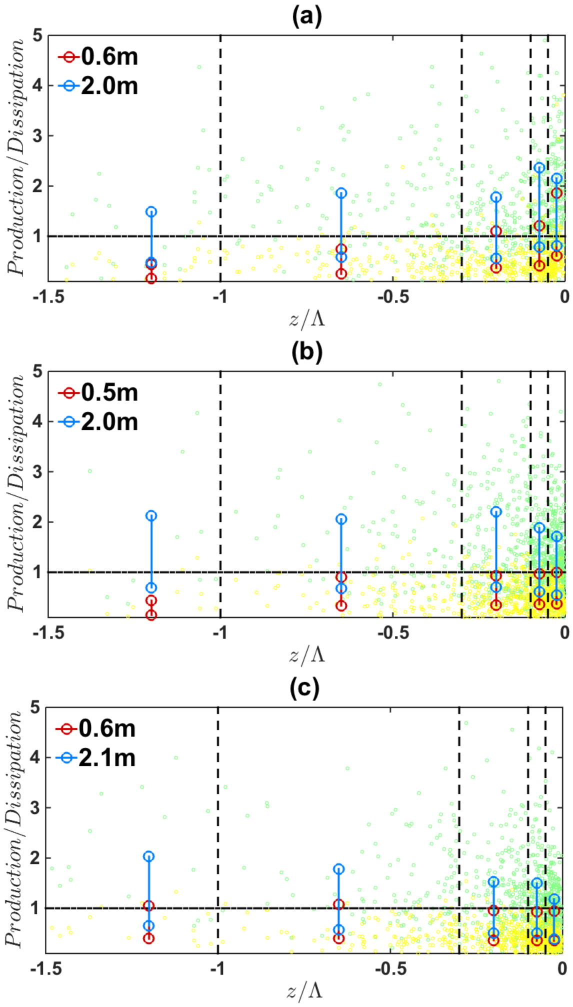

Figure 4.11: Imbalance ratio of production to dissipation rate of $\overline{\theta^2}$ at a) Playa site, b) Sagebrush site, and c) Slope site. Green and yellow dots represent 30-min averaged imbalance ratio based on the dissipation rate calculated by second-order and third-order structure function at the bottom two levels. Red and blue circles represent bin-averaged values at two different heights over different ranges of z/Λ, which is same as the ones in Figure 4.9. The upper dots represent the ratio based on ϵ_θ calculated by second-order structure function, and the bottom dots represent the one by third-order structure function.

magnitude of temperature variance was greatest at Sagebrush site, and smallest at Playa site. This difference was likely caused by variations in surface roughness. Scaled and unscaled potential temperature variance were also investigated as a function of height and stability. A stronger variation was observed at Playa than at the other two sites. $\overline{\theta^2}$ profiles showed a rapid decrease with increasing height such that the PTV was 36%, 37%, and 52% of it's 0.6 m value at 5 m at Playa, Sagebrush, and Slope sites, respectively.

Based on the vertical distribution of the most significant budget terms, we can see that over all three sites, the production and dissipation terms decrease rapidly with height within a shallow ≈5-m thick layer. Above this shallow layer, all the terms become relatively small. The scaled temperature variance budget shows a inconsistent profile at all sites. The scaling term $w^* {T^*}^2/(kz)$ does not work well to capture the mechanisms of temperature variance budget profiles. The subsidence at Playa site causes a negative temperature gradient (Massey et al., 2014), which leads to an unusual negative production term of $\overline{\theta^2}$.

In order to find the relative significance of the turbulent transport term, the ratio of the turbulent transport to the production term was calculated. There are ≈45% (14%) of data with a ratio > 0.1 (0.2) at Playa, and ≈20% of data with a ratio > 0.1 at Sagebrush site. At the Slope site, the ratio peaks between 0.1 and 0.2, which includes ≈55% of the data. The mechanism behind this unexpected PDF distribution is not clear. Overall, turbulent transport might not be negligible over Playa and Slope, and might be small over a more typical surface, which is flat and relatively rough (i.e., Sagebrush site).

To investigate the controversial argument from Bradley et al., (1981); Sempreviva & Højstrup, (1998); Wyngaard & Coté, (1972)., which stated that turbulent transport is negligible most of time and could be important under near-neutral conditions, we analysed the ratio of turbulent transport to production at all sites at the lowest two levels. In this study, we do observe significant ratios (up to 0.5) during near-neutral conditions. However, the ratio remains relatively constant through near-neutral and unstable conditions at all three sites with a value of about 0.1 to 0.2.

A comparison between different determination of ϵ_θ is presented. The data is from 1330 to 1800 MST at Playa Site when the boundary layer is shear-dominated, which is ideal for the direct method. If we consider ϵ_θ from the direct method is close to the 'true' value, an underestimated ϵ_θ from the second-order structure function and an overestimated ϵ_θ from the spectral density and the third-order structure function methods. Nevertheless, this result implies that ϵ_θ based on the indirect methods is still valuable to evaluate the imbalance ratio between production to dissipation rates.

The ratio of production to dissipation or the imbalance ratio was relatively constant across the full range of convective conditions studied. At the 2-m level, a general balance between production and dissipation can be assumed over unstable conditions at all three sites. However, this is not the case at 0.6-m. In particular at Playa site, a very low value of the ratio (≈ 0.5) can be found when $z/\Lambda < -1$. This imbalance can be caused by strong thermal heterogeneity at Playa, which is also observed from Hang et al., (2015).

In summary, there are still many knowledge gaps regarding to the temperature variance budget over different surfaces and stability conditions. This study is providing more observational data to improve the basic understanding of temperature variance budget in the atmospheric boundary layer.

4.6 References

Abdella, K., & N. McFarlane (1997), A new second-order turbulence closure scheme for the planetary boundary layer, *Journal of the Atmospheric Sciences*, *54*(14), 1850–1867, doi:http://doi.org/dd6j4h

Albertson, J. D., M. B. Parlange, G. G. Katul, C.-R. Chu, H. Stricker, & S. Tyler (1995), Sensible heat flux from arid regions: a simple flux-variance method, *Water Resources Research*, *31*(4), 969–973, doi:https://doi.org/10.1029/94wr02978

Antonia, R. A., A. J. Chambers, D. Phong-Anant, & S. Rajagopalan (1979), Properties of spatial temperature derivatives in the atmospheric surface layer, *Boundary-Layer Meteorology*, *17*(1), 101–118, doi:https://doi.org/10.1007/bf00121939

Antonia, R. A., A. J. Chambers, & C. A. Friehe (1980), Note on the viscous heating term in the temperature variance equation, *Boundary-Layer Meteorology*, *19*(3), 269–272, doi:https://doi.org/10.1007/bf00120591

Antonia, R. A., L. W. B. Browne, A. J. Chambers, & S. Rajagopalan (1983), Budget of the temperature variance in a turbulent plane jet, *International Journal of Heat and Mass Transfer*, *26*(1), 41–48, doi:https://doi.org/10.1016/s0017-9310(83)80006-4

Arwatz, G., C. Bahri, A. J. Smits, & M. Hultmark (2013), Dynamic calibration and modeling of a cold wire for temperature measurement, *Measurement Science and Technology*, *24*(12), 125,301, doi:https://doi.org/10.1088/0957-0233/24/12/125301

Asanuma, J., & W. Brutsaert (1999), Turbulence variance characteristics of temperature and humidity in the unstable atmospheric surface layer above a variable pine forest, *Water Resources Research*, *35*(2), 515–521, doi: https://doi.org/10.1029/1998wr900051

Bradley, E. F., R. A. Antonia, & A. J. Chambers (1981), Temperature structure in the atmospheric surface layer, *Boundary-Layer Meteorology*, *20*(3), 275–292, doi: https://doi.org/10.1007/bf00121373

Caughey, S. J., & J. C. Wyngaard (1979), The turbulence kinetic energy budget in convective conditions, *Quarterly Journal of the Royal Meteorological Society*, *105*(443), 231–239, doi:https://doi.org/10.1256/smsqj.44314

Champagne, F. H., C. A. Friehe, J. C. LaRue, & J. C. Wynagaard (1977), Flux measurements, flux estimation techniques, and fine-scale turbulence measurements in the unstable surface layer over land, *Journal of the Atmospheric Sciences*, *34*(3), 515–530, doi:https://doi.org/10.1175/1520-0469(1977)034¡0515:fmfeta¿2.0.co;2

Chapra, S. C., & R. P. Canale (1998), *Numerical methods for engineers*, vol. 2, New York: McGraw-Hill.

Coantic, M., & O. Simonin (1984), Radiative effects on turbulent temperature spectra and budgets in the planetary boundary layer, *Journal of the Atmospheric Sciences*, *41*(17), 2629–2651, doi:http://doi.org/b2t8kz

Deardorff, J. W (1961)., On the direction and divergence of small-scale turbulent heat flux, *Journal of the Atmospheric Sciences*, *18*(4), 540–548, doi: https://doi.org/10.1175/1520-0469(1961)018

Detto, M., G. Katul, M. Mancini, N. Montaldo, & J. D. Albertson (2008), Surface heterogeneity and its signature in higher-order scalar similarity relationships, *Agricultural and Forest Meteorology*, *148*(6-7), 902–916, doi: https://doi.org/10.1016/j.agrformet.2007.12.008

Edson, J. B., & C. W. Fairall (1998), Similarity relationships in the marine atmospheric surface layer for terms in the TKE and scalar variance budgets, *Journal of the Atmospheric Sciences*, *55*(13), 2311–2328, doi:http://doi.org/b948jh

Fernando, H. J. S., et al., (2015), The MATERHORN: Unraveling the intricacies of mountain weather, *Bulletin of the American Meteorological Society*, *96*(11), 1945–1967, doi:https://doi.org/10.1175/bams-d-13-00131.1

Frenzen, P., & C. A. Vogel (1992), The turbulent kinetic energy budget in the atmospheric surface layer: A review and an experimental reexamination in the field, *Boundary-Layer Meteorology*, *60*(1-2), 49–76, doi: https://doi.org/10.1007/bf00122061

Hang, C., D. F. Nadeau, D. D. Jensen, S. W. Hoch, & E. R. Pardyjak (2015), Playa soil moisture and evaporation dynamics during the MATERHORN field program, *Boundary-Layer Meteorology*, *159*(3), 521–538, doi: https://doi.org/10.1007/s10546-015-0058-0

Högström, U. (1990), Analysis of turbulence structure in the surface layer with a modified similarity formulation for near neutral conditions, *Journal of the Atmospheric Sciences*, *47*(16), 1949–1972, doi:https://doi.org/10.1175/1520-0469(1990)0472.0.co;2

Jensen, D. D., D. F. Nadeau, S. W. Hoch, & E. R. Pardyjak (2015), Observations of near-surface heat-flux and temperature profiles through the early evening transition over contrasting surfaces, *Boundary-Layer Meteorology*, *159*(3), 567–587, doi:https://doi.org/10.1007/s10546-015-0067-z

Jensen, D. D., D. F. Nadeau, S. W. Hoch, & E. R. Pardyjak (2016), The evolution and sensitivity of katabatic flow dynamics to external influences through the evening transition, *Quarterly Journal of the Royal Meteorological Society*, *143*(702), 423–438, doi:https://doi.org/10.1002/qj.2932

Kaimal, J. C., J. C. Wyngaard, D. A. Haugen, O. R. Coté, Y. Izumi, S. J. Caughey, & C. J. Readings (1976), Turbulence structure in the convective boundary layer, *Journal of the Atmospheric Sciences*, *33*(11), 2152–2169, doi: https://doi.org/10.1175/1520-0469(1976)0332.0.co;2

Katul, G., S. M. Goltz, C.-I. I. Hsieh, Y. Cheng, F. Mowry, & J. Sigmon (1995), Estimation of surface heat and momentum fluxes using the flux-variance method above uniform and non-uniform terrain, *Boundary-Layer Meteorology*, *74*(3), 237–260, doi:https://doi.org/10.1007/bf00712120

Kiely, G., J. D. Albertson, M. B. Parlance, & W. E. Eichinger (1996), Convective scaling of the average dissipation rate of temperature variance in the atmospheric surface layer, *Boundary-Layer Meteorology*, *77*(3-4), 267–284, doi: https://doi.org/10.1007/bf00123528

Kroon, L. J. M., & H. A. R. de Bruin (1995), The Crau field experiment: turbulent exchange in the surface layer under conditions of strong local advection, *Journal of Hydrology*, *166*(3-4), 327–351, doi:https://doi.org/10.1016/0022-1694(94)05092-c

Lee, Y.-H. (2009), The influence of local stability on heat and momentum transfer within open canopies, *Boundary-Layer Meteorology*, *132*(3), 383–399, doi: https://doi.org/10.1007/s10546-009-9405-3

Li, D., G. G. Katul, & P. Gentine (2015), The k^{-1} scaling of air temperature spectra in atmospheric surface layer flows, *Quarterly Journal of the Royal Meteorological Society*, *142*(694), 496–505, doi:https://doi.org/10.1002/qj.2668

Lloyd, C. R., A. D. Culf, A. J. Dolman, & J. H. C. Gash (1991), Estimates of sensible heat flux from observations of temperature fluctuations, *Boundary-Layer Meteorology*, *57*(4), 311–322, doi:https://doi.org/10.1007/bf00120051

Lumley, J. L., & H. A. Panofsky (1964), *The structure of atmospheric turbulence*, Hoboken, NJ: Wiley.

Mason, P. J., & S. H. Derbyshire (1990), Large-eddy simulation of the stably-stratified atmospheric boundary layer, *Boundary-Layer Meteorology*, *53*(1), 117–162.

Massey, J. D., W. J. Steenburgh, S. W. Hoch, & J. C. Knievel (2014), Sensitivity of near-surface temperature forecasts to soil properties over a sparsely vegetated dryland region, *Journal of Applied Meteorology and Climatology*, *53*(8), 1976–1995.

Mellor, G. L., & T. Yamada (1974), A hierarchy of turbulence closure models for planetary boundary layers, *Journal of the Atmospheric Sciences*, *31*(7), 1791–1806.

Mironov, D. V., & P. P. Sullivan (2016), Second-moment budgets and mixing intensity in the stably stratified atmospheric boundary layer over thermally heterogeneous surfaces, *Journal of the Atmospheric Sciences*, *73*(1), 449–464.

Monji, N. (1972), Budgets of turbulent energy and temperature variance in the transition zone from forced to free convection, Thesis (Ph.D.), University of Washington, Seattle, WA.

Nadeau, D. F., E. R. Pardyjak, C. W. Higgins, H. J. S. Fernando, & M. B. Parlange (2011), A simple model for the afternoon and early evening decay of convective turbulence over different land surfaces, *Boundary-Layer Meteorology*, *141*(2), 301–324.

Nadeau, D. F., E. R. Pardyjak, C. W. Higgins, & M. B. Parlange (2013), Similarity scaling over a steep alpine slope, *Boundary-Layer Meteorology*, *147*(3), 401–419.

Nilsson, E., F. Lohou, M. Lothon, E. Pardyjak, L. Mahrt, & C. Darbieu (2016), Turbulence kinetic energy budget during the afternoon transition — Part 1: Observed surface TKE budget and boundary layer description for 10 intensive observation period days, *Atmospheric Chemistry and Physics*, *16*(14), 8849–8872.

Obukhov, A. M. (1946), Turbulentnost'v temperaturnoj-neodnorodnoj atmosfere, *Trudy Geofizicheskogo Instituta, Akademiya Nauk SSSR*, *1*, 95–115.

Obukhov, A. M. (1949), Temperature field structure in a turbulent flow, *Izvestiya, Academy of Sciences, USSR, Atmosphere*, *13*, 58–69.

Otić, I., G. Grötzbach, & M. Wörner (2005), Analysis and modelling of the temperature variance equation in turbulent natural convection for low-prandtl-number fluids, *Journal of Fluid Mechanics*, *525*, 237–261.

Panofsky, H. A., & J. A. Dutton (1984), *Atmospheric turbulence: models and methods for engineering applications*, Hoboken, NJ: Wiley.

Plate, E. J. (1971), Aerodynamic characteristics of atmospheric boundary layers., *Tech. rep.*, Karlsruhe University: Argonne National Lab.

Sempreviva, A. M., & J. Højstrup (1998), Transport of temperature and humidity variance and covariance in the marine surface layer, *Boundary-Layer Meteorology*, *87*(1986), 233–253.

Shaw, W. J., J. H. Trowbridge, & A. J. Williams (2001), Budgets of turbulent kinetic energy and scalar variance in the continental shelf bottom boundary layer, *Journal of Geophysical . . .* , *106*, 9551–9564.

Sreenivasan, K. R., R. A. Antonia, & H. Q. Danh (1977), Temperature dissipation fluctuations in a turbulent boundary layer, *Physics of Fluids*, *20*(8), 1238.

Wyngaard, J. C., & O. R. Coté (1971), The budgets of turbulent kinetic energy and temperture variance in the atmospheric surface layer, *Journal of the Atmospheric Sciences*, *28*(2), 190–201.

Wyngaard, J. C., & O. R. Coté (1972), Cospectral similarity in the atmospheric surface layer, *Quarterly Journal of the Royal Meteorological Society*, *98*(417), 590–603.

Wyngaard, J. C., O. R. Coté, & Y. Izumi (1972), Local free convection, similarity, and the budgets of shear stress and heat flux, *Journal of the Atmospheric Sciences*, *29*(6), 1230–1231.

Yaglom, A. M. (1948), Homogeneous and isotropic turbulence in a viscous compressible fluid, *Izvestiya, Academy of Sciences, USSR, Atmosphere*, *12*, 501.

Zhou, T., & R. A. Antonia (2000), Approximations for turbulent energy and temperature variance dissipation rates in grid turbulence, *Physics of Fluid*, *12*(2), 335–344.

CHAPTER 5

CONCLUSIONS AND FUTURE WORK

In this work, observational data were used to study the flow processes and scalar transport over diverse terrain, including mountainous terrain and flat surfaces with strong thermal and moisture heterogeneities. The main objective was to better understand the complex exchange of heat and moisture over different types of surfaces and subject to various atmospheric conditions so that the performance of numerical weather forecasting models can be improved through more accurate boundary conditions and parameterizations. The results presented were based on two extensive filed campaigns, which were conducted in an arid environment (the U.S. Army Dugway Proving Ground) and a sheltered alpine valley, as part of the MATERHORN program.

Chapter 2 described a strong spatial and temporal variation of surface moisture and evaporation over a flat desert surface. After occasional rain events, evaporation rates were enhanced by a few local features, such as soil properties, which had features of high water capacity and low permeability, surface albedo, and soil moisture, which caused a positive feedback mechanism and significant nocturnal evaporation. In addition, a strong surface temperature and moisture heterogeneity was observed over a desert Playa site, a flat surface with negligible surface roughness. The difference in near-surface soil moisture and cumulative evaporation was more than 5 mm from site to site over a very small distance ($\sim$200 m). This result clearly revealed the complexity of scalar transport over a flat and horizontal homogeneous surface, which would be ideal for momentum transport near the surface.

Chapter 3 described a case study of a typical shallow and short-lived valley fog in a sheltered alpine valley. The results indicated the significance of mountain circulations in the valley fog processes. In particular, internal gravity waves, generated by surrounding topography, greatly influenced the fog evolution by varying the near-surface temperature and wind fields. To better understand and predict the evolution of radiation fog in the valley, a comprehensive spatial coverage of observations near the surface would be required to capture rapid flow processes and complex interactions between mountain circulations.

Chapter 4 investigated the temperature variance budget over three different arid surfaces, which were a flat non-vegetated Playa (the same site used in Chapter 2), a flat vegetated Sagebrush, and a vegetated gentle Slope site. Typically, a perfect balance between production and dissipation of $\overline{\theta^2}$ is assumed in weather forecasting models. To examine the validity of this balance, we studied the temperature variance budget under unstable conditions. The results showed that the budget was not closed based on two dominant terms, and the turbulent transport term could be non-negligible at Playa and Slope sites. The imbalance ratio of production on how dissipation terms were determined. In addition, the observations also indicated the existence of a persistent surface-based 5-m layer where the magnitude of production and dissipation terms of $\overline{\theta^2}$ dropped rapidly with increasing height over all three sites.

The present dissertation revealed the complexity of heat and moisture transport in the atmospheric boundary layer over diverse terrain. The findings made a meaningful contribution to the literature of scalar transport in different topics. Meanwhile, many new scientific questions and research opportunities emerged from this study. In Chapter 2, we showed a strong variation of near-surface soil moisture and evaporation rates over relatively small spatial scales ($\sim$ 100 m). More work could be followed with a focus on thermal heterogeneity near the surface. For example, Morrison et al., (2017) developed a new method to compute spatially and temporally varying surface sensible heat flux at playa site from high-frequency thermal imagery. In Chapter 3, we found that to improve the prediction of valley fog, it was necessary to have a better knowledge of flow dynamics in mountainous terrain during stably-stratified boundary layer, including katabatic flows, cold-air pools, internal gravity waves, etc. It was desirable to have more observations that showed the rapid interactions between mountain circulations and radiation fogs. The rapid changes of fog evolution include not only in temporal scales, which can be $\sim$10 min but also in spatial scales, which cover the range from 10^1 m to 10^4 m. In Chapter 4, we found the existence of a persistent 5-m shallow surface layer with respect to the potential temperature variance regardless of surface types. Some analytical work should be done to explain this shallow surface layer and to investigate the thermal roughness length. In addition, the present results showed that it was questionable to use the balance between the production and dissipation term of the temperature variance in the second-order turbulence closure model under near-neutral condition and over complex terrain. More effort could be dedicated to the terms that received much less attention in the temperature variance budget, such as the importance of the turbulent transport term and radiation destruction term, the determination of dissipation rates, and the validation of horizontal homogeneities.

5.1 References

Morrison, T., M. Calaf, H. J. S. Fernando, T. Price, & E. Pardyjak (2017), A methodology for computing spatially and temporally varying surface sensible heat flux from thermal imagery, *Quarterly Journal of the Royal Meteorological Society*, *143*, 2616–2614, doi:http://dx.doi.org/10.1002/qj.3112